

Department of Precision and Microsystems Engineering

A refocusing mechanism for a laser satellite communication terminal

A.C.Garde

Report no : 2022.049
Coach : Prof. dr. ir. G. V. Vdovin
Specialisation : OPT
Type of report : Master Thesis
Date : 30 August 2022

A refocusing mechanism for a laser satellite communication terminal

by

A.C.Garde

to obtain the degree of Master of Science
at the Delft University of Technology,
to be defended publicly on Tuesday August 30, 2022 at 01:00 PM.

Student number:	5255244	
Project duration:	October 01, 2021 – August 30, 2022	
Thesis committee:	Prof. dr. ir. G. V. Vdovin,	TU Delft, supervisor
	Dr. ir. S. Kuiper,	TNO, supervisor
	Dr. ir. L. A. Cacace,	TU Eindhoven, committee member
	Prof. dr. N. Bhattacharya,	TU Delft, committee member
	Prof. dr. ir. G. N. Gaydadjiev,	TU Delft, committee member

An electronic version of this thesis is available at <http://repository.tudelft.nl/>.

Acknowledgement

I would like to thank everyone who assisted me during my project. I would like to thank Pieter Kappelhof for finding me this project. At TNO, I would like to thank Stefan Kuiper for our weekly meetings. His expertise in system design and mechanical design helped me navigate through the project. I would also like to thank Dorus de Lange and Rob Vink for our meetings and discussions and their expertise in optics. At TU Delft I would like to thank Gleb Vdovin for our biweekly meetings. His constructive feedback helped me improve my work. I would like to thank Lennino Cacace for our biweekly OM meetings during the first few months and the monthly meetings thereafter. I would like to thank all the OM students (Sawa Bezelev, Wei She and Emile Heezen) for their feedback during our OM meeting. I would like to thank my intern colleagues at TNO (Emile Heezen, Roel Habraken) for having interesting discussions about the project and beyond. Finally, I would like to thank my parents for their support and continuous encouragement throughout the project.

Contents

List of Figures	vi
List of Tables	ix
Acronyms and Abbreviations	x
1 Introduction	1
1.1 Research goal	1
1.2 Thesis structure	2
I Literature Research	3
2 Laser satellite communication	4
2.1 Why laser communication?	4
2.2 Laser and RF communication comparison	5
2.2.1 Propagation of electromagnetic waves	5
2.2.2 High data rate	6
2.2.3 Small size	6
2.2.4 Better security	7
2.3 Challenges of laser satellite communication	7
2.3.1 Pointing Accuracy	7
2.4 Technical background	7
2.5 Conclusion	9
3 Laser communication terminal	10
3.1 Laser communication terminal(LCT) overview	10
3.1.1 Laser	11
3.1.2 Telescope	12
3.1.3 Coarse Pointing Assembly	13
3.1.4 Fine Steering Mirror	14
3.1.5 Detectors	15
3.2 Pointing, acquisition and tracking	16

3.2.1	Pointing	16
3.2.2	Acquisition	16
3.2.3	Tracking	17
3.3	Conclusion	17
4	State of the Art: Refocusing mechanisms	18
4.1	Refocusing mechanism for the Solar Orbiter mission	18
4.2	In-orbit refocusing mechanism for SpaceEye-1	19
4.3	CHEMCAM autofocus mechanism	20
4.4	Refocusing mechanism for EO telescopes	21
4.5	Thermal refocusing method for spaceborne imagers	21
4.6	Piezoelectric refocusing mechanism	22
4.7	Comparison and summary	23
4.8	Conclusion	25
II	Refocusing System Design	26
5	Defocus detection	27
5.1	Rx beam simulation	27
5.1.1	Gaussian beam spot at focus	27
5.1.2	Optical fiber coupling efficiency	28
5.1.3	Camera spot size	32
5.2	Tx beam simulation	33
5.3	Conclusion	35
6	Refocusing system operation	36
6.1	The refocusing system	36
6.2	Use case scenarios	37
6.2.1	Scenario 1	37
6.2.2	Scenario 2	40
6.3	Conclusion	42
7	Mechanism placement	43
7.1	Potential locations	43
7.2	Trade-off	45
7.2.1	Conclusion	47

8	Extremum seeking control	48
8.1	Extremum seeking control	48
8.1.1	Working of ESC	49
8.2	Simulink model	50
8.3	ESC with white noise	52
8.4	Requirement drivers	53
8.5	Conclusion	54
9	System requirements	55
9.1	Operational requirements	55
9.2	Environmental requirements	57
9.3	Functional design	57
9.4	Conclusion	59
III	Mechanism Design	60
10	Actuator selection	61
10.1	Definitions and selection criteria	61
10.2	High level actuator trade-off	61
10.3	Linear actuators	62
10.4	Hybrid actuator	63
10.5	Conclusion	64
11	Mechanism design	65
11.1	Guidance concepts	65
11.2	Concept choice	66
11.3	Guidance design	67
11.3.1	Requirement	68
11.3.2	Material selection	70
11.3.3	Axial stiffness	70
11.3.4	Radial stiffness	71
11.3.5	Resolution	72
11.3.6	Resonance frequency	72
11.3.7	Stress criteria	73
11.3.8	Flexure dimensions	73
11.4	Strut	73
11.4.1	Strut dimensions	74
11.5	Power consumption	75
11.6	Design overview	76
11.7	Final design	76

11.8 Manufacturing	78
11.9 Conclusion	78
12 Thermal and mechanical analysis	79
12.1 Material properties	79
12.2 Model verification	79
12.3 Mechanical analysis	80
12.3.1 Boundary conditions	80
12.3.2 100g acceleration in X direction	82
12.3.3 100g acceleration in Y direction	83
12.3.4 100g acceleration in Z direction	84
12.3.5 +30 micron displacement in Z direction	85
12.3.6 Modal analysis	86
12.4 Thermal analysis	88
12.4.1 Boundary conditions	88
12.4.2 Mesh	88
12.4.3 Maximum operational temperature	89
12.4.4 Minimum operational temperature	92
12.4.5 Actuator + laser heat load	95
12.5 Summary	97
12.6 Conclusion	98
13 Conclusion and recommendations	99
13.1 Conclusion	99
13.2 Recommendations	100
13.2.1 Mechanism design	100
13.2.2 Actuator design	100
13.2.3 Actuator and laser heat load case	100
13.2.4 Manufacturing and assembly	100
13.2.5 RFM stability	100
A Mechanisms	101
B Optical simulation	104
Bibliography	105

List of Figures

1.1	3D model of the telescope.	1
2.1	Laser communication network[4].	5
2.2	Gaussian beam divergence parameters.	6
2.3	User satellite and ground station.	7
2.4	Laser communication between a user and hub satellite.	8
2.5	Communication between a hub satellite and a ground station can be either by RF or laser.	9
3.1	A system breakdown of the laser communication satellite.	11
3.2	Hub laser communication terminal overview.	11
3.3	Loss of pure silica fiber as a function of wavelength[12].	12
3.4	Transmittance through Earth's atmosphere[13]. Shaded blue areas are transparent.	12
3.5	A cross section view of a Cassegrain telescope	13
3.6	Coarse pointing assembly developed by TNO[17].	14
3.7	Fast steering mirror developed by TNO[18].	15
3.8	Detectors on-board the LCT.	16
3.9	Spiral scan performed by the transmitter satellite.	17
3.10	Acquisition strategy for line of sight alignment between satellites S1 and S2.	17
4.1	Refocusing mechanism for the Solar Orbiter mission [22] (a) CAD model (b) Cross section view	19
4.2	Refocusing mechanism on the SpaceEye-1. Image on the left shows the refocusing mechanism installed on the secondary mirror. Image on the right shows the telescope. [23]	20
4.3	Refocusing mechanism on the Curiosity rover [24]	20
4.4	Cross section of a refocusing mechanism for an Earth Observation satellite [25]. The colour code for the figure is as follows: Blue: outer cylinder, Orange: Inner cylinder, Green: Connections, Grey: Fixed, Red: electrical heater patch, Yellow lines: Multi-layer insulation, Dashed blue lines: Low emissivity coating. Arrows indicate direction of movement.	21
4.5	Refocusing mechanism with a thermal actuator on the M2 mirror for a Korsch telescope [26]	22
4.6	Shell type piezoelectric actuator fixed at the bottom. Red arrow shows the movement of piezoelectric material and blue arrow shows the movement of the top surface where a mirror can be mounted [27].	22
5.1	Gaussian laser beam through focus.	28
5.2	Gaussian fiber coupling	29

5.3	Optical system for Rx beam optical fiber coupling efficiency simulation. The schematic is not to scale.	30
5.4	Ray height(u) and ray angle(θ) for a beam passing through a lens.	31
5.5	Fiber coupling efficiency as a function of M2 mirror movement.	32
5.6	Spot size captured by the ACQ camera at different M2 defocus positions.	33
5.7	Spot size seen by the horizontal strip of pixels passing through the center of the beam spot at different M2 defocus positions.	33
5.8	Schematic of the optical system used for Tx beam simulation.	34
5.9	Power intercepted by the partnering satellite as a function of M2 mirror movement.	35
6.1	A system breakdown with the components of the refocusing system highlighted in blue.	36
6.2	A schematic of the refocusing system.	37
6.3	Use case scenario 1 flowchart. Boxes are colour coded according to the satellite(s) in operation. The RFM operation is marked with red coloured outline and numbered.	39
6.4	Use case scenario 2.	41
7.1	Terminal mechanical overview	44
8.1	Extremum seeking control loop.	48
8.2	Extremum seeking control for $\hat{u} < u^*$	49
8.3	Extremum seeking control for $\hat{u} > u^*$	50
8.4	ESC simulink block diagram	51
8.5	Fiber coupling efficiency as a function of M2 displacement fitted to a Gaussian.	51
8.6	ESC with white noise simulink block diagram	52
8.7	White noise in time domain y-axis: millimeters x-axis: seconds	52
8.8	ESC without noise.	53
8.9	ESC with noise.	53
9.1	Dimensions of the M2 mirror.	58
9.2	RFM functional block diagram.	58
10.1	Schematic of the hybrid actuator.	64
11.1	Tangential flexure concept. Note that the co-ordinate system for the guidance is in uppercase.	67
11.2	A membrane of the tangential flexure concept.	67
11.3	Guidance stiffness as a function of actuator stiffness.	68
11.4	A schematic of the mirror-guidance combination.	69
11.5	Resonance frequency f_2 as a function of disk spacing.	70
11.6	The flexure is modelled as a cantilever beam under a point load at it's free end. The original shape is shown in solid and the shape of the deformed beam is shown in dashed. Note that the co-ordinate system for a flexure is in lowercase.	71
11.7	A schematic of the radial stiffness of one of the membranes. Here, F and d is the direction of external force and displacement respectively. Angle α is the angle between the direction of displacement and the x axis.	72

11.8 Flexure design	73
11.9 A schematic of the strut.	74
11.10 Strut.	75
11.11 Static power consumption for a hybrid actuator.	76
11.12 Isometric view of the final design.	77
11.13 Exploded view of the final design.	77
11.14 Isometric view of membrane.	78
12.1 Mechanism force displacement plot.	80
12.2 Fixed boundary condition is highlighted by the blue surfaces.	81
12.3 Spring foundation surface is highlighted by blue.	82
12.4 Results for launch acceleration in X direction.	83
12.5 Results for launch acceleration in Y direction.	84
12.6 Results for launch acceleration in Z direction.	85
12.7 Results for a prescribed displacement of 30 microns.	86
12.8 Roller boundary condition highlighted by the blue surfaces.	88
12.9 Mesh of the RFM assembly.	89
12.10 Maximum operational temperature loadcase.	90
12.11 Schematic of thermal expansion. Here, M2: M2 mirror, S: strut, H: housing, A: actuator, I/F:RFM telescope interface.	91
12.12 Zernike decomposition of the deformed mirror surface.	92
12.13 Minimum operational temperature loadcase.	93
12.14 Schematic of thermal contraction. Here, M2: M2 mirror, S: strut, H: housing, A: actuator, I/F:RFM telescope interface.	94
12.15 Zernike decomposition of the deformed mirror surface.	95
12.16 Laser+actuator loadcase.	96
12.17 Stress detail for laser+actuator loadcase.	96
12.18 Zernike decomposition of the deformed mirror surface.	97
A.1 FACT sheet.	101
B.1 Airy disk through focus. The defocus from left to right is 0, 20, 40, 60 μm	104

List of Tables

2.1	Comparison of RF and laser beam divergence for a propagation distance of 10,000 kilometers in free space.	6
4.1	State of the Art refocusing mechanism comparison	24
7.1	Sensitivity table for the mirror M2 and the lens group.	46
7.2	Mechanism placement trade-off.	46
9.1	Refocusing mechanism operational requirements table.	57
9.2	Refocusing mechanism environmental requirement table.	57
10.1	Actuator high level trade-off.	62
10.2	Actuator trade-off table	63
11.1	Concept comparison summary.	66
11.2	Flexure material properties.	70
11.3	Subsystem design overview.	76
12.1	Material properties	79
12.2	Modal analysis	87
12.3	Summary of mechanical load cases.	97
12.4	Summary of thermal load cases.	98
A.1	1 DoF linear motion mechanisms.	103

Acronyms and Abbreviations

COTS	Commercial off the shelf component
CPA	Coarse pointing assembly
EO	Earth Observation
ESA	European Space Agency
ESC	Extremum seeking control
FOV	Field of view
FSM	Fine steering mirror
HST	Hub satellite
IE	Integrated energy
LCT	Laser Communication Terminal
LG	Lens group
M1	Telescope primary mirror
M2	Telescope secondary mirror
MTF	Modulation transfer function
PAM	Point ahead mechanism
PAT	Pointing Acquisition and Tracking
RF	Radiofrequency (communication)
RFM	Refocusing mechanism
Rx	Receiver
TNO	The Netherlands Organisation for Applied Scientific Research
Tx	Transmitter
UST	User satellite
WFE	Wavefront error

Chapter 1

Introduction

Laser satellite communication is a promising technology which offers high data rates and more secure links compared to the mature radio frequency communication. The focus of this project is on inter-satellite laser communication. The laser communication terminal must be compact to be market viable. The overall volume of the terminal is driven by the size of the telescope. TNO has designed a compact two mirror on-axis telescope. The combination of small size and high magnification makes it highly sensitive to focus error. The source of the focus error lies in the change in distance between the two mirrors. This affects the optical quality of both the incoming and outgoing laser beam. The focus error needs to be within 2 microns for successful operation. Such a sensitive telescope subject to high launch loads and harsh space environment imposes challenging dimensional tolerances. The compensation of the focus error is possible by actuating either one of the telescope mirrors or other optical components in the system. The challenge is to survive launch and maintain the telescope in focus during operation

1.1 Research goal

The laser satellite communication terminal needs to be low SWAP (Size, weight and power) to be market viable. The telescope is an important part of the terminal. TNO has developed a two mirror Cassegrain telescope shown in figure 1.1. The compact telescope is sensitive to focus error introduced by the change in distance between the two mirrors. In this case the tolerance on focus error is 2 microns. This makes it difficult to build the telescope on manufacturing tolerances. A solution is to have a refocusing mechanism to correct for defocus.

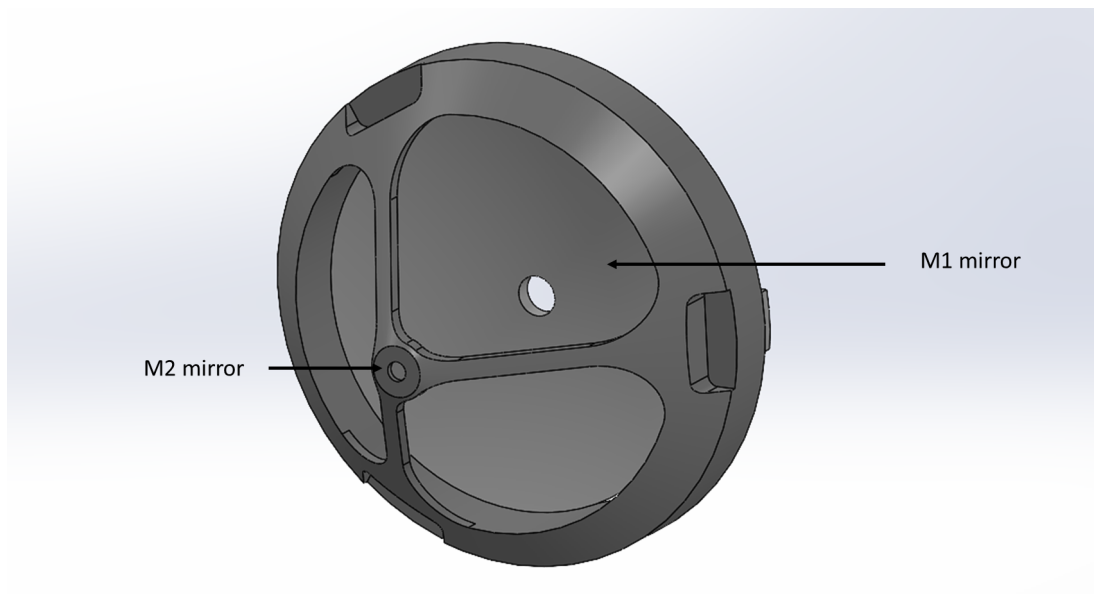


Figure 1.1: 3D model of the telescope.

The goal of this research is divided in two parts. First part of the project is to carry out a system design and show how the requirements flow from the system level to the mechanism level. This comprises of making use case scenarios, a trade-off on which optical component to actuate, modelling a control technique and free space optics simulations to derive the mechanism requirements. The second part of the project is to design the refocusing mechanism and show that it meets the requirements. This consists of the mechanism design process and FEM analysis to show that the mechanism meets the derived requirements.

1.2 Thesis structure

The thesis is divided into three parts. Part I: Literature Research, Part:II Refocusing system design and Part:III Mechanism design.

Part I of the thesis starts with chapter 2 which gives a technical background on laser satellite communication. In chapter 3 the functions of the components on-board a laser communication terminal are explained and the steps followed to establish an inter-satellite link is studied. Chapter 4 consists of the refocusing mechanisms found in literature used in space applications. The part ends with a reflection on the literature.

Part II of the thesis consists of the refocusing system design. In chapter 5 the on-board detectors are investigated to find what are the range of defocus they can detect. This is done by simulating the inter-satellite receiver (Rx) and transmitter (Tx) beams. In chapter 6 a high level system design is made with use case scenarios. In chapter 7 a trade-off is performed to select the best location to place the refocusing mechanism. In chapter 8 it is shown that extremum seeking control can be used to close the loop. The part ends with the system requirements in chapter 9.

Part III comprises of the mechanism design and analysis. It starts with chapter 10 in which a trade-off is performed to select a suitable actuator. Further, chapter 11 shows the concept and design of the mechanism. Mechanical and thermal simulations are carried out in chapter 12. Finally, in chapter 13 main conclusions of the thesis are presented and recommendations are made for future work.

Part I

Literature Research

Chapter 2

Laser satellite communication

The chapter starts with an introduction to laser communication, its advantages over the mature radio frequency (RF) communication and challenges. Motivation for using laser satellite communication for the project at TNO is presented. This is done by answering the following research questions.

- Why is laser communication better than RF communication?
- What are the challenges of laser communication?
- What is the application of this project?

2.1 Why laser communication?

There has been an exponential increase in the data rates required for transferring data from satellites to ground stations [1]. The mature radio communication technology is reaching its theoretical limit in terms of data rates. Laser satellite communication has been proven to be able to reach data rates of gigabits/second (Gb/s) [2] which are envisioned to reach terabits/second (Tb/s)[3]. The network of laser communication is shown in figure 2.1. Laser satellite communication primarily consists of two types of links: Inter-satellite communication and satellite to ground communication.

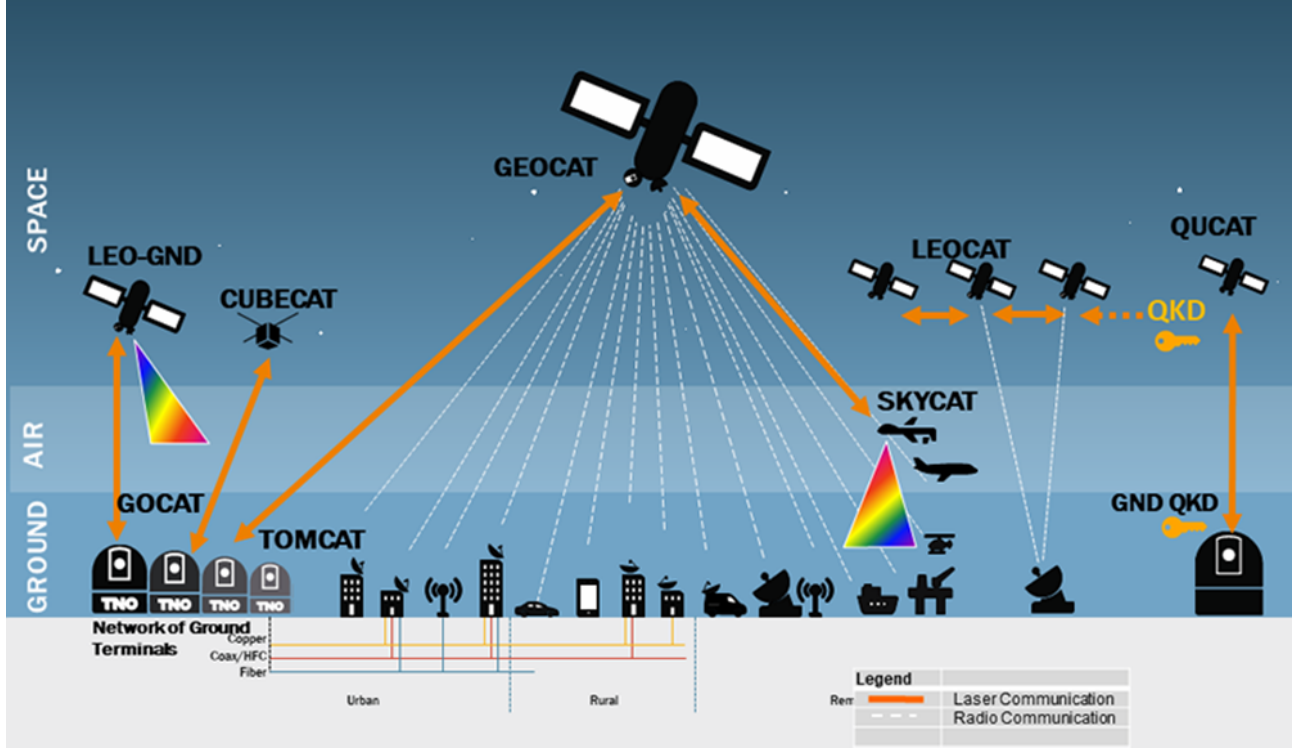


Figure 2.1: Laser communication network[4].

The aim of laser satellite communication is to have high data transfer rate with low size, weight and power (SWAP). Laser communication is a promising technology which has the potential to fulfil these requirements. The advantages of optical communication over RF communication are listed below.

1. High data rate [5].
2. Better security.
3. Small size.
4. No licensing required [6].

Theory for supporting these points will be elaborated in the following sub-sections.

2.2 Laser and RF communication comparison

2.2.1 Propagation of electromagnetic waves

Radio frequency and laser are both part of the electromagnetic spectrum. The divergence angle of an electromagnetic wave with a Gaussian intensity profile is given by equation 2.1.

$$\theta = \frac{\lambda}{\pi D_0} \quad (2.1)$$

Far-field diameter is given by equation 2.2. Note that small divergence angle means small far-field diameter for the same propagation distance.

$$D_f = 2\theta z = 2 \frac{\lambda z}{\pi D_0} \quad (2.2)$$

where,

θ : Divergence angle

λ : wavelength of electromagnetic wave

D_0 : Aperture diameter

D_f : Far-field diameter

z : propagation distance

The frequency range of RF communication is 1-40 GHz according to [7]. Optical communication works in the infrared part of the electromagnetic spectrum with a wavelength range of 820-1550 nm (in free space). Consider a transmitter and a receiver separated by a distance of 10,000 km and the antenna diameter of the transmitter is 0.2 m. The divergence angle and far-field diameter at the receiver is summarized in table 2.1.

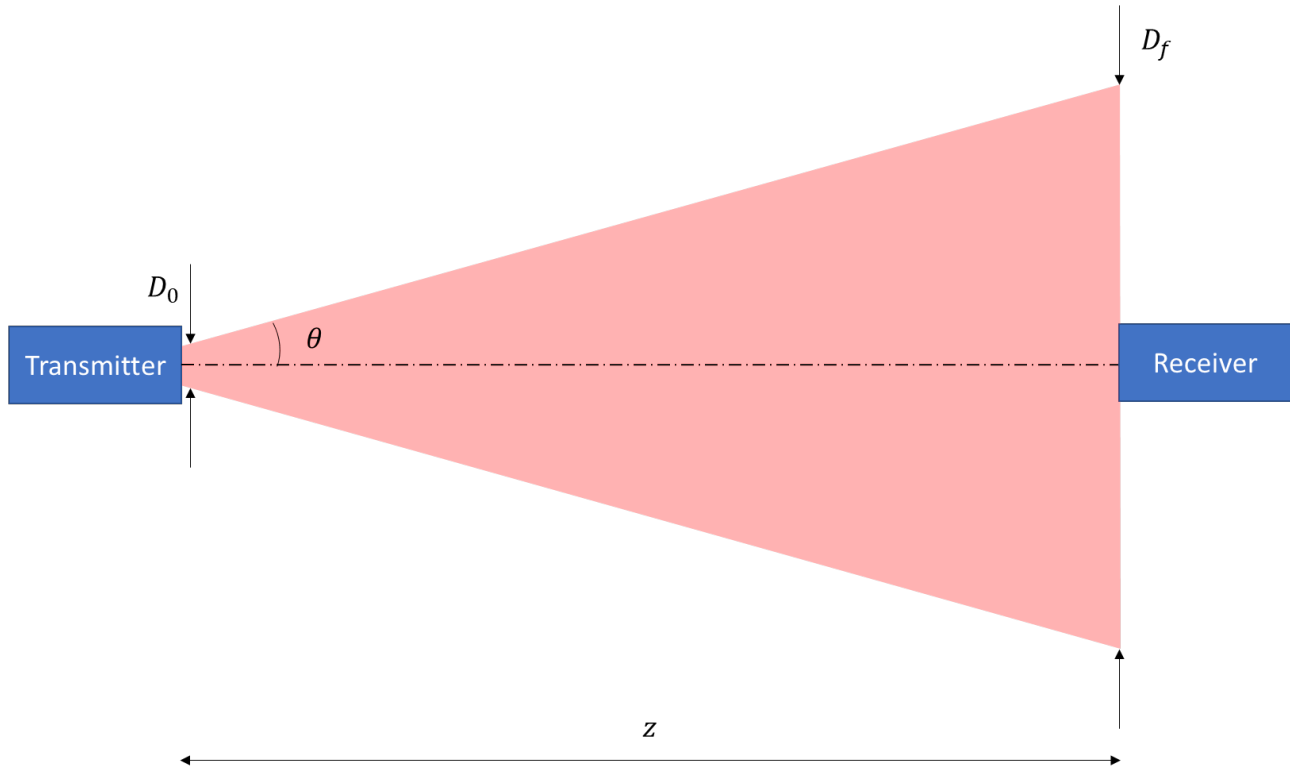


Figure 2.2: Gaussian beam divergence parameters.

	Wavelength	Frequency	Divergence (θ)	Far-field diameter (D)
RF	300-7.5 mm	1-40 GHz	477-11.9 mrad	19,098-477 km
Laser	850-1550 nm	350-193 THz	1.35-2.47 μ rad	54.1-98.7 m

Table 2.1: Comparison of RF and laser beam divergence for a propagation distance of 10,000 kilometers in free space.

2.2.2 High data rate

A laser has high carrier frequency compared to RF. As shown in table 2.1, light in the infrared (IR) region has three orders of magnitude higher frequency than RF. The bandwidth of data transfer is 20% of the carrier frequency [8]. This means that the theoretical upper limit for RF is 8 Gb/s and for laser it is 48 Tb/s.

2.2.3 Small size

The diameter of beam at the receiver is 6 orders of magnitude smaller for a laser compared to RF. This means that for a laser, the same amount of power is available in a smaller area. The size of the receiver antenna can be smaller to intercept the same amount of power.

The small size of the communication terminal means that more satellites can be accommodated for a single launch which is more economical.

2.2.4 Better security

The narrow beam divergence of a laser is difficult to intercept. This results in better security of transmitted information.

2.3 Challenges of laser satellite communication

Although laser satellite communication has advantages over RF communication it also has its own set of challenges.

1. Pointing accuracy.

2.3.1 Pointing Accuracy

The divergence of beam as calculated in table 2.1 is in micro-radian. The pointing stability has to be in this order of magnitude which is difficult.

Another challenge is the point ahead angle. This arises due to the relative velocity between the two communicating satellites [9].

2.4 Technical background

There are currently 479 Earth Observation (EO) commercial satellites revolving around the Earth in Low Earth Orbit (LEO) [10]. With an ever increasing demand for high quality and amount of information these satellites generate a lot of data. This data is sent from the EO satellites called user to ground stations by RF communication. This communication link is visualized in figure 2.3. A user satellite is available for communication with the ground station for a limited period of time which means that the large amount of data generated has to be transmitted to the ground station within this small period of time. This is a major bottleneck.

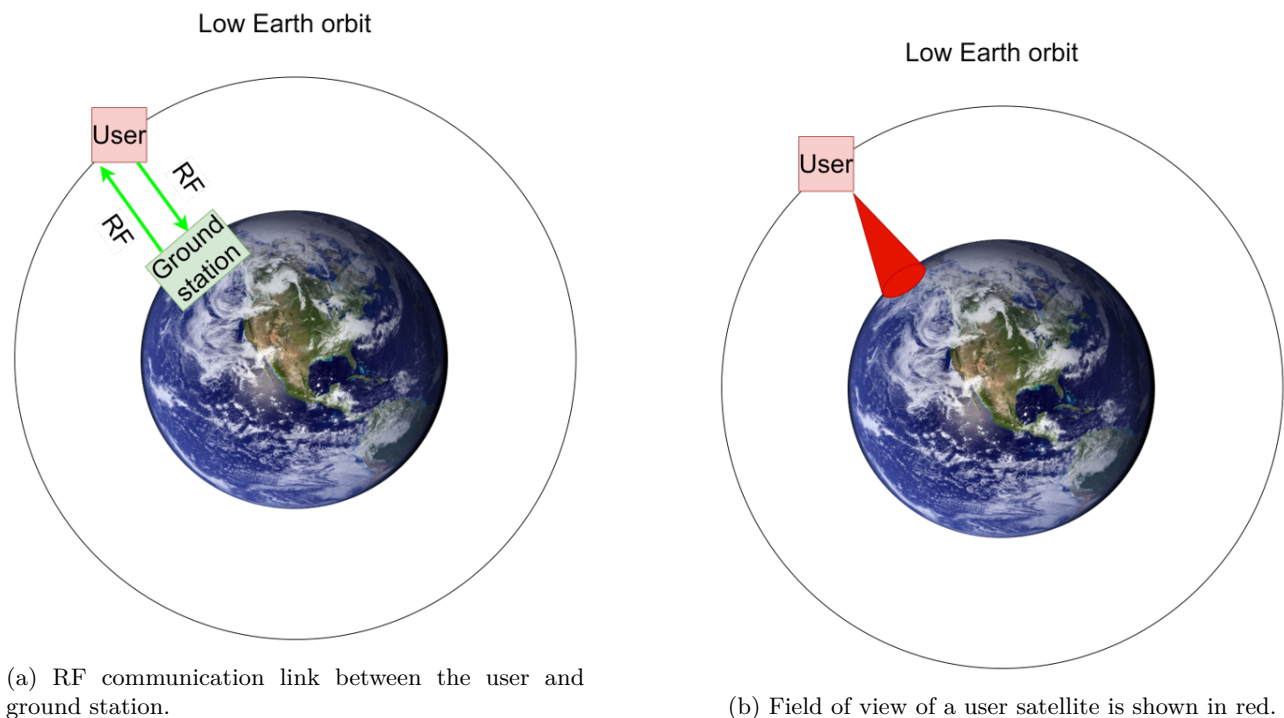


Figure 2.3: User satellite and ground station.

To overcome this, a hub satellite can be used to relay the data from user satellites to ground stations. With multiple hub satellites located in medium earth orbit (MEO), the user satellites can communicate with the ground stations at all times. The optical communication between the user and hub satellite is shown in figure 2.4. The communication between the hub satellite and ground station is shown in figure 2.5.

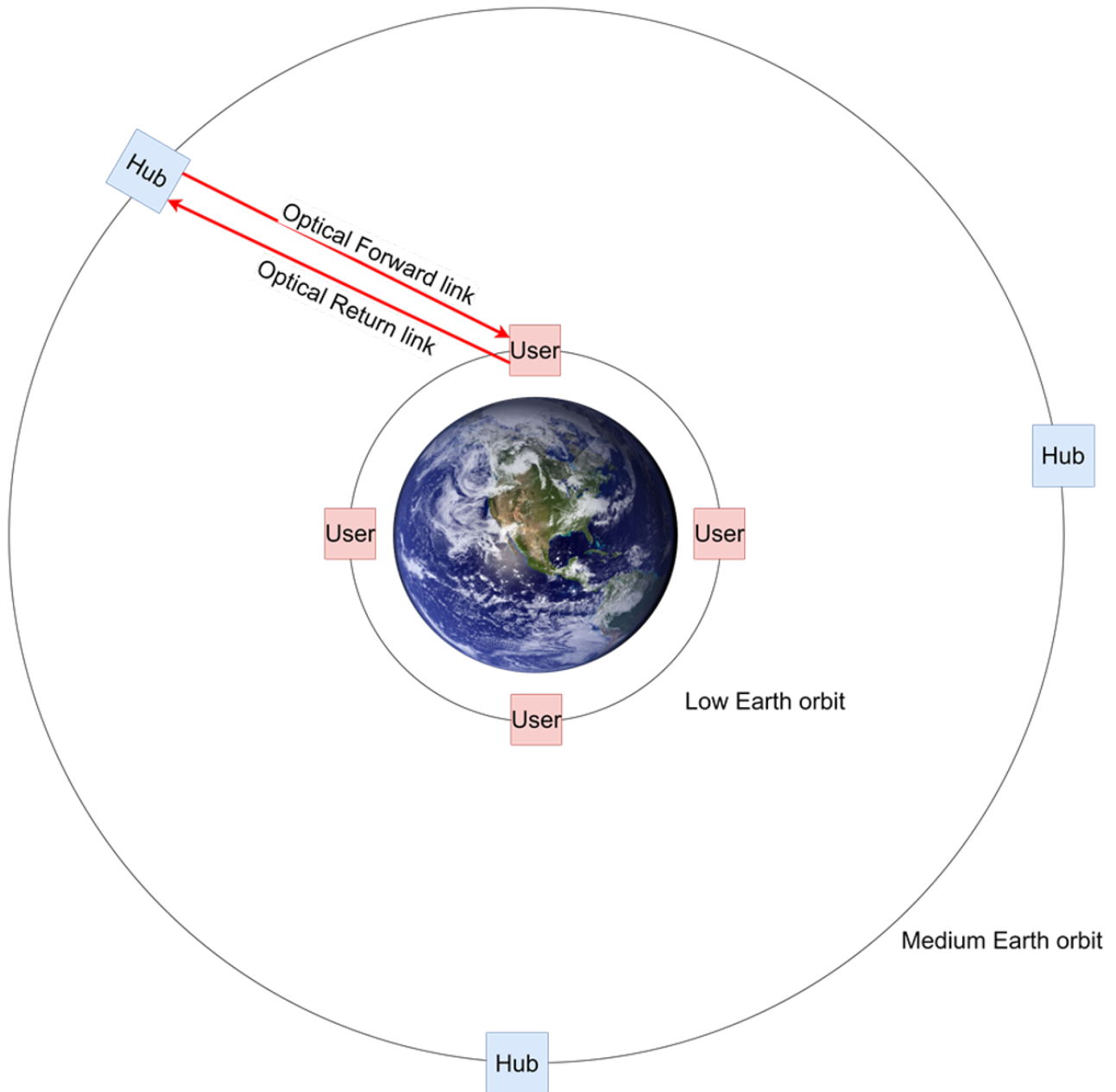


Figure 2.4: Laser communication between a user and hub satellite.

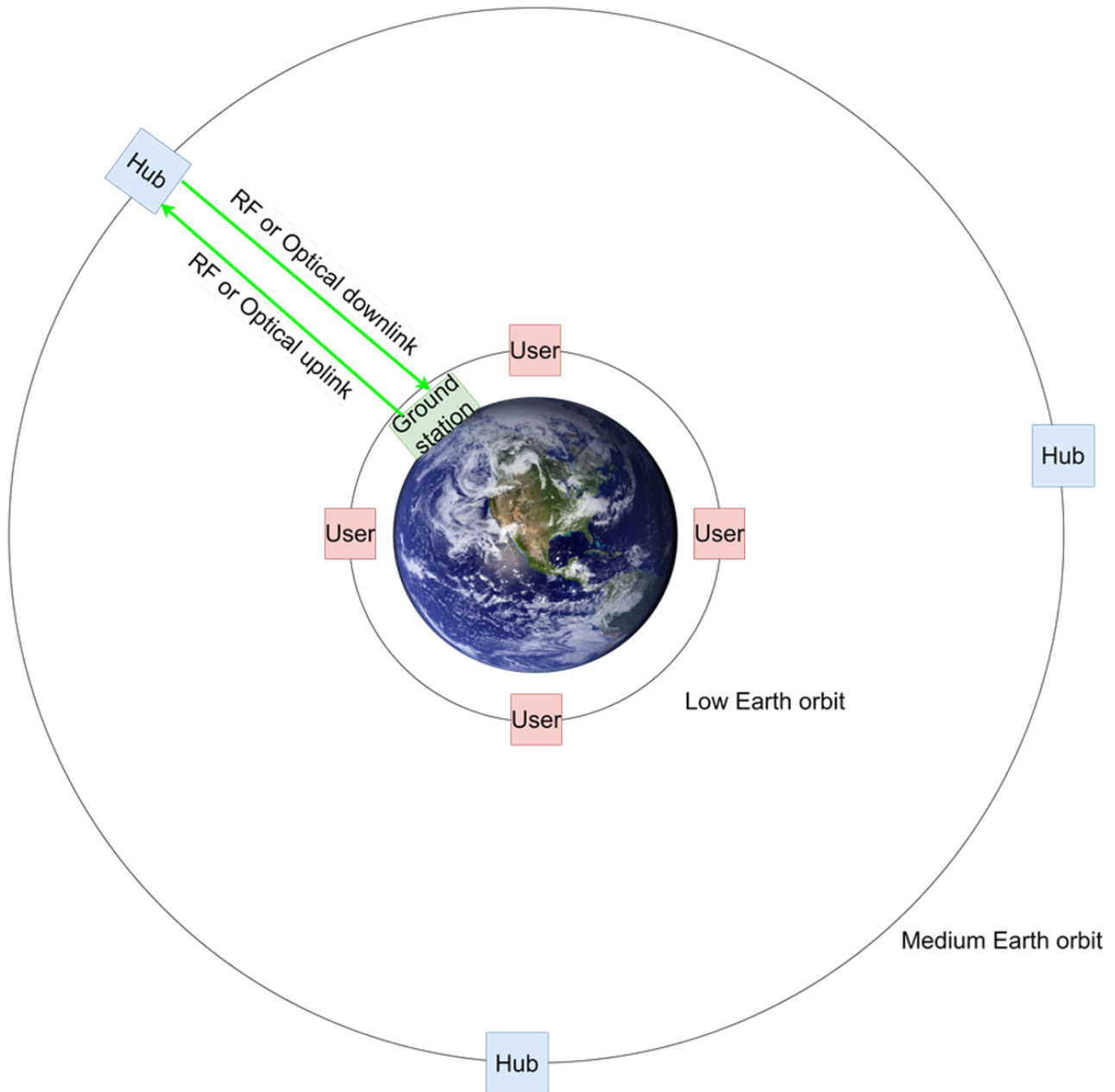


Figure 2.5: Communication between a hub satellite and a ground station can be either by RF or laser.

The focus of this project is on the inter-satellite communication between the hub and the user satellite, in particular the refocusing mechanism on the hub satellite telescope.

2.5 Conclusion

Laser satellite communication and RF communication are compared and it is shown laser communication has certain advantages. A technical background was presented highlighting the inter-satellite communication which is the focus of this project.

Chapter 3

Laser communication terminal

The chapter starts with an overview of a laser communication terminal. The main components on-board are discussed. The Pointing, Acquisition and Tracking(PAT) strategy to establish a stable inter-satellite link before the start of a communication session is explained in detail. This is explored by the following research questions.

- What are the different components onboard the laser communication satellite?
- How does a satellite establish a link?

3.1 Laser communication terminal(LCT) overview

An overview of a typical LCT is shown in figure 3.2. The components of a laser communication communication terminal are:

1. Laser
2. Coarse pointing assembly (CPA).
3. Telescope (mirror M1 and M2).
4. collimator (lens L1).
5. Fast steering mirror (FSM).
6. Point ahead mirror (PAM).
7. Detectors: Camera, Fiber, quadcell.
8. Collimating mirror (CM).

A systematic system breakdown is shown in figure 3.1. The main components are discussed one by one in the following subsections.

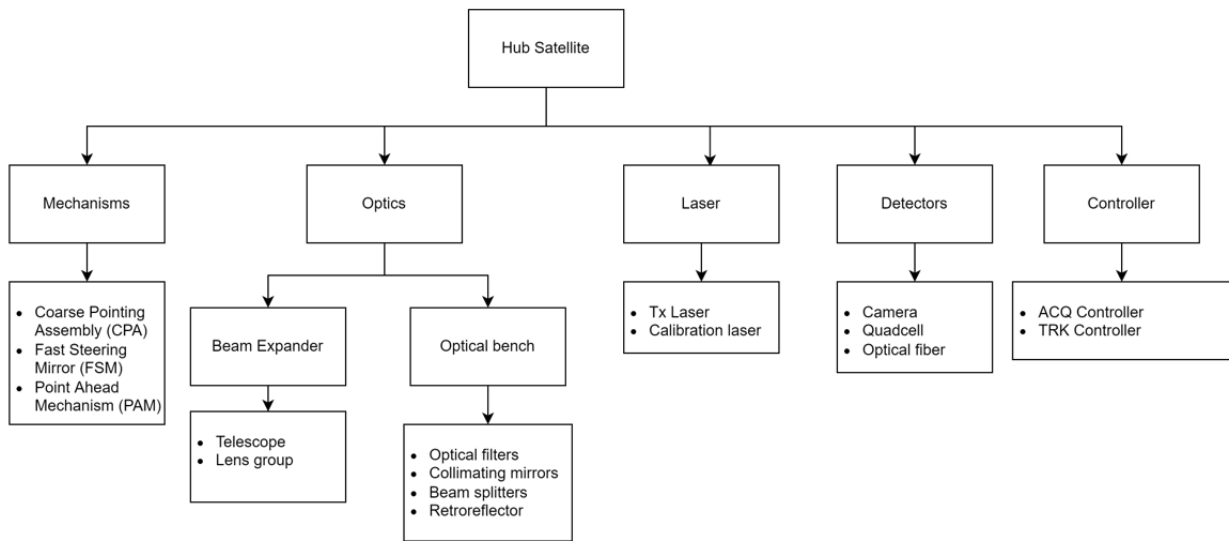


Figure 3.1: A system breakdown of the laser communication satellite.

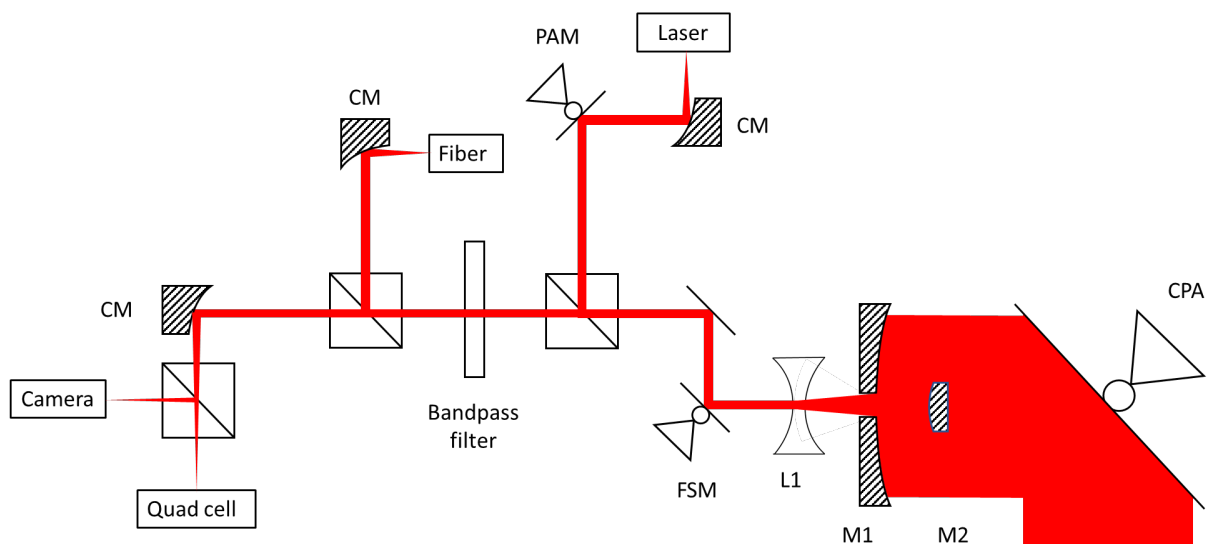


Figure 3.2: Hub laser communication terminal overview.

3.1.1 Laser

The function of a laser is to transfer data by intensity modulation to represent digital 1 and 0 states. The wavelength of light used is 1550 nm. The following reasons[8] make this wavelength attractive for laser communication between a satellite and a ground station.

1. Invisible to the human eye as well as eye safe[11].
2. Silica glass optical fiber used for telecommunication has minimum loss at 1550 nm as shown in figure 3.3. As telecommunication is a developed field, all the optical components such as lasers, fiber amplifiers are commercially available.
3. A range of wavelength around 1550 nm has high transmittance through Earth's atmosphere as shown in figure 3.4.

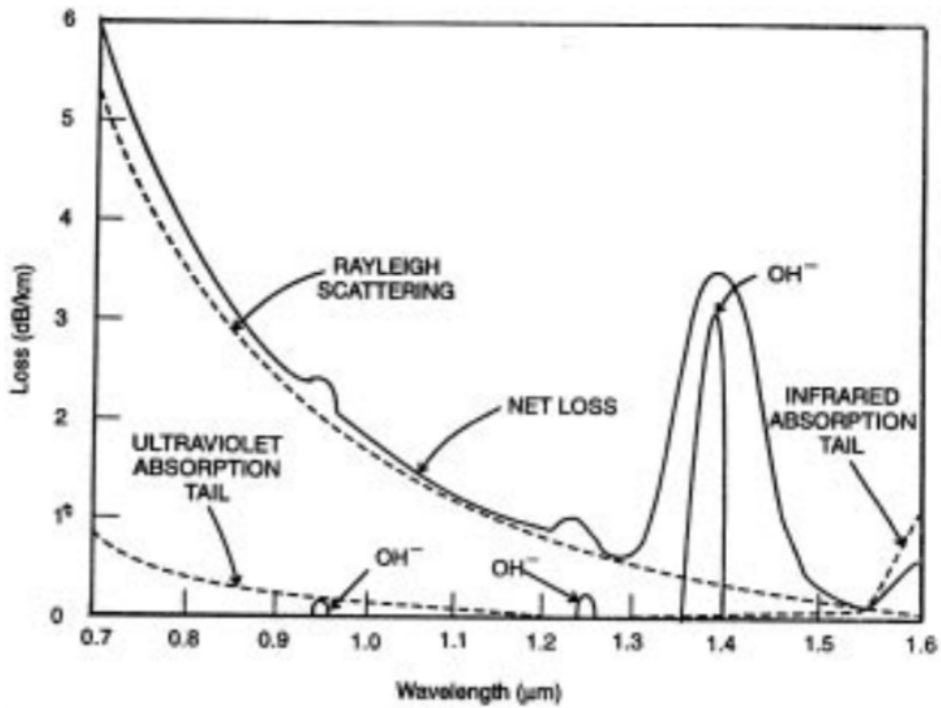


Figure 3.3: Loss of pure silica fiber as a function of wavelength[12].

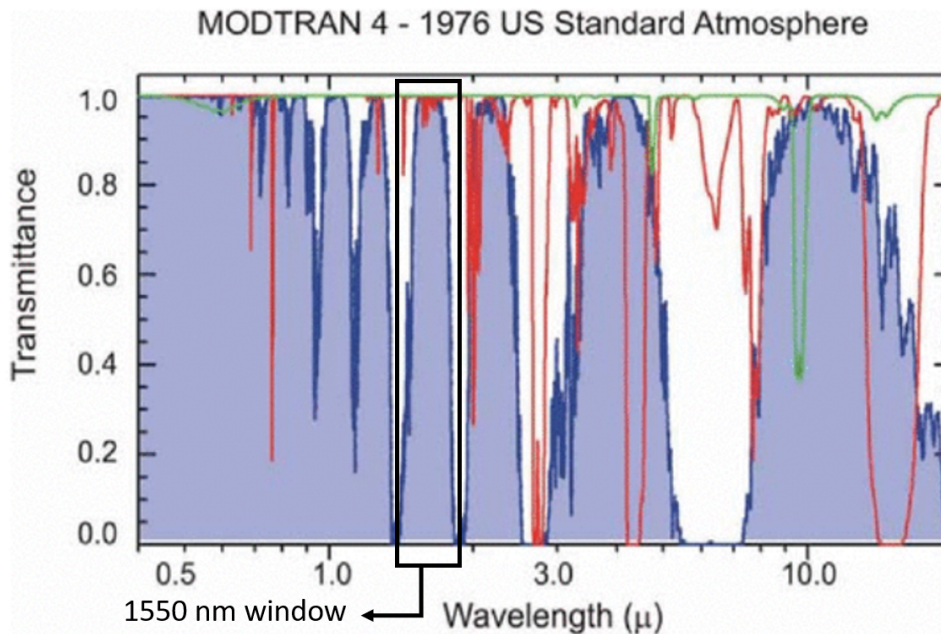


Figure 3.4: Transmittance through Earth's atmosphere[13]. Shaded blue areas are transparent.

3.1.2 Telescope

The telescope has a dual function, it demagnifies the Rx beam and magnifies the Tx beam. It is well known that a circular beam of light at the source with a large diameter has low divergence and hence the diameter at a very long distance is small. The requirements for a good space telescope [14] are given below.

1. Small size and weight.

2. Ability to operate over a range of wavelengths.

A telescope is classified into two categories: a reflector and a refractor. A reflector uses mirrors to manipulate light whereas a refractor uses lenses. A reflector has the following advantages over a refractor.

1. No chromatic aberrations[15].
2. Easy mounting.
3. Compact design.

This makes a logical argument to choose a reflector over a refractor. There is a wide variety of reflector telescopes in literature, but the most popular are two mirror and three mirror telescopes. Two mirror telescopes require smaller volume and are therefore more attractive for space applications.

Two of the most popular two mirror telescopes are Cassegrain and Gregorian. Cassegrain is preferred over Gregorian because of its shorter tube length. This reduces the overall telescope volume.

A typical Cassegrain telescope is shown in figure 3.5. The telescope consists of a concave primary mirror(M1) and a convex secondary mirror(M2).

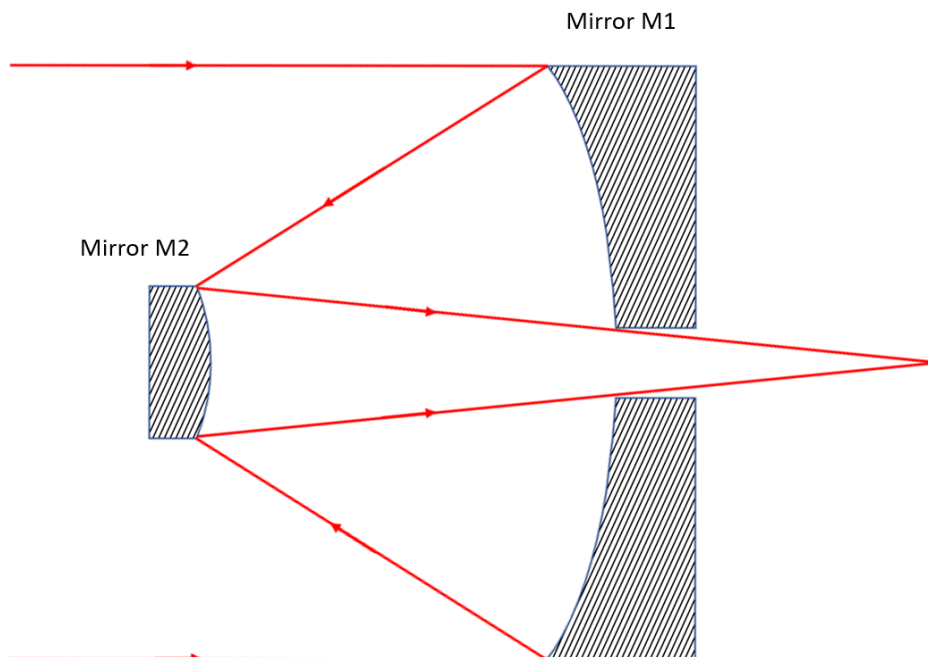


Figure 3.5: A cross section view of a Cassegrain telescope

The properties of a Cassegrain telescope are summarized below.

1. The optical design can be optimized to be an aplanatic [16]. This means that spherical and coma aberrations can be eliminated.
2. Short tube length.

3.1.3 Coarse Pointing Assembly

The coarse pointing assembly(CPA) enables a satellite to have a large field of regard. In this way, the satellite can point at the partnering satellite before the start of a communication session.

A model of CPA is shown in figure 3.6. The two axis are driven by variable reluctance motors visible on the right and bottom. The CPA has two axis of rotations in azimuth and elevation. Both the motors have a hall sensor which is used to operate the CPA in closed loop. The CPA enables the satellite to continuously point at the partnering satellite.

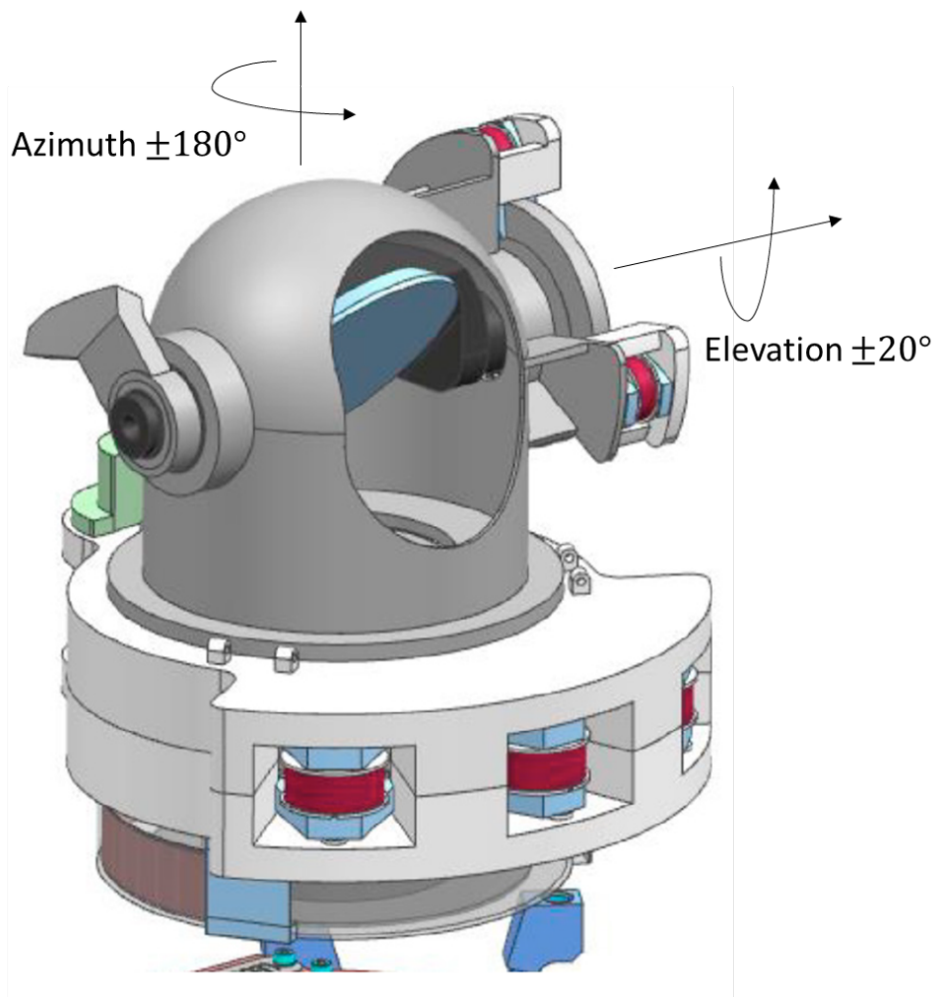


Figure 3.6: Coarse pointing assembly developed by TNO[17].

3.1.4 Fine Steering Mirror

A fine steering mirror(FSM) is a motorised flat mirror with tip-tilt movement to compensate for high frequency disturbances. It steers the beam with a high resolution over an optical angular range of $\pm 2^\circ$. The FSM has a bandwidth of >1000 Hz to compensate for beam jitter and microvibrations in the terminal to maintain a stable line of sight alignment between two satellites. The FSM is developed by TNO[18] and shown in figure 3.7.

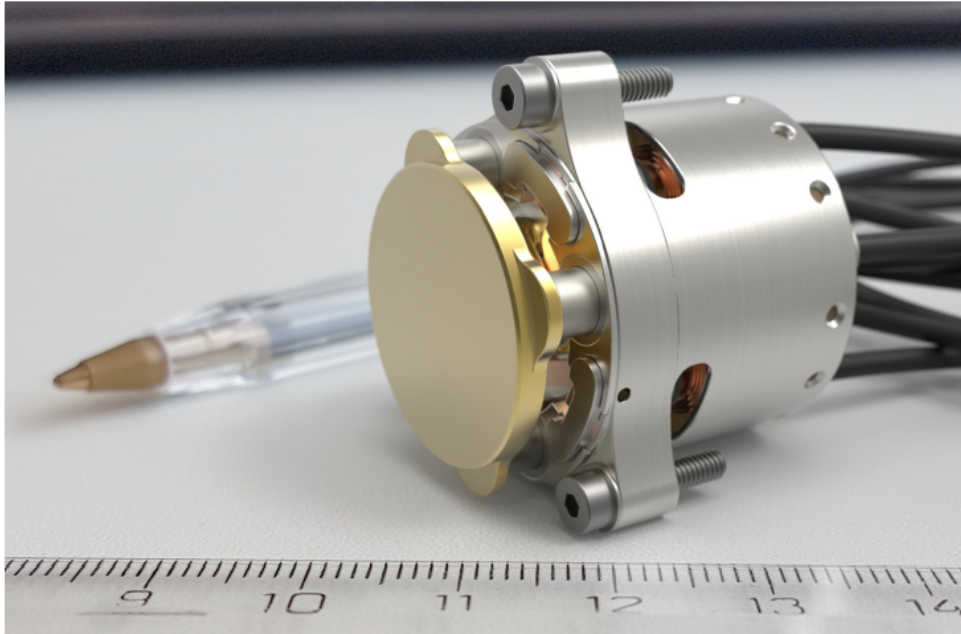


Figure 3.7: Fast steering mirror developed by TNO[18].

3.1.5 Detectors

There are three detectors on the terminal. These have a specific function which will be explained one by one.

1. Optical fiber: for data communication
2. Quadcell: for operating FSM in closed loop
3. Camera: for line of sight alignment with the partnering satellite

Optical fiber

The optical fiber is used as a receiver for the communication signal. The optical fiber is an amplifier for the incoming light. The light ultimately falls on a photodiode which converts the light information into electrical signal. A typical image of an optical fiber is shown in figure 3.8a.

Quadcell

A quadcell is an optical sensor with four identical photosensitive areas called cells. It is used to determine the position of the laser spot based on the amount of light received by each cell. In this case the beam position is continuously monitored and acts as a feedback for the CPA and FSM to maintain line of sight alignment. A typical quadcell is shown in figure 3.8b.

Camera

The camera is a large collection of small photosensitive areas. It is used to obtain a coarse line of sight alignment. The reason to use a camera is that it has a larger field of view compared to other detectors. A typical picture of a camera is shown in figure 3.8c.

Typical picture of these detectors are shown in figure 3.8.

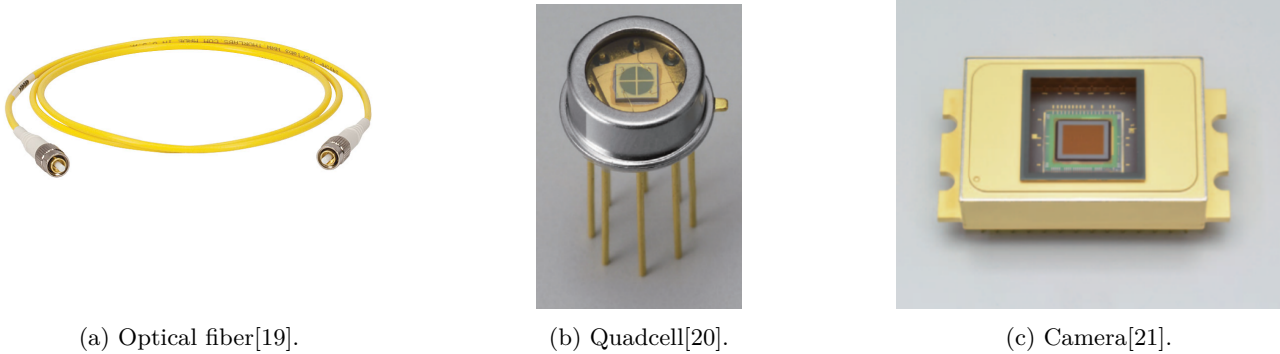


Figure 3.8: Detectors on-board the LCT.

3.2 Pointing, acquisition and tracking

Pointing, acquisition and tracking (PAT) is a strategy used to align two satellites. In table 2.1, it was shown that over a range of 10,000 km the laser beam diameter is around 100 m. This means that both the satellites must point with an accuracy of $2.5 \mu\text{rad}$ to receive the laser beam. It is difficult to align two satellites with such a stringent line of sight alignment. A commonly followed procedure to make this possible is a three step process pointing, acquisition and tracking. The steps taken during these phases is explained in the following subsections.

3.2.1 Pointing

In the pointing stage, the satellite receives information about the partnering satellite. This information is used to position the CPA to point at the partnering satellite. As both the satellites are in motion, the CPA has to keep track of the partnering satellite. This is done in open loop.

3.2.2 Acquisition

The Acquisition (ACQ) stage can be visualised as shown in figure 3.10.

In the S1 to S2 step, satellite S1 starts scanning its laser beam in a spiral pattern with its PAM as shown in figure 3.10. During the scan, S2 watches for the laser beam with its camera. In one cycle of the scan, the line of sight of S1 and S2 aligns for a certain moment and the S2 ACQ camera sees this as a blip. The controller on S2 moves its FSM to improve the line of sight alignment based on the position of the blip on the camera. Multiple cycles maybe required to center the laser beam on the ACQ camera.

In the S2 to S1 step, the satellite roles are interchanged and the same procedure is carried out.

In the fine acquisition step, both the satellites reduce their spiral scan size to further improve the line of sight alignment. When the spiral scan size is reduced in steps, at one point, the spiral scan size converges to the size of beam divergence. At this point there is a continuous spot on the ACQ camera. At this point the acquisition stage is complete.

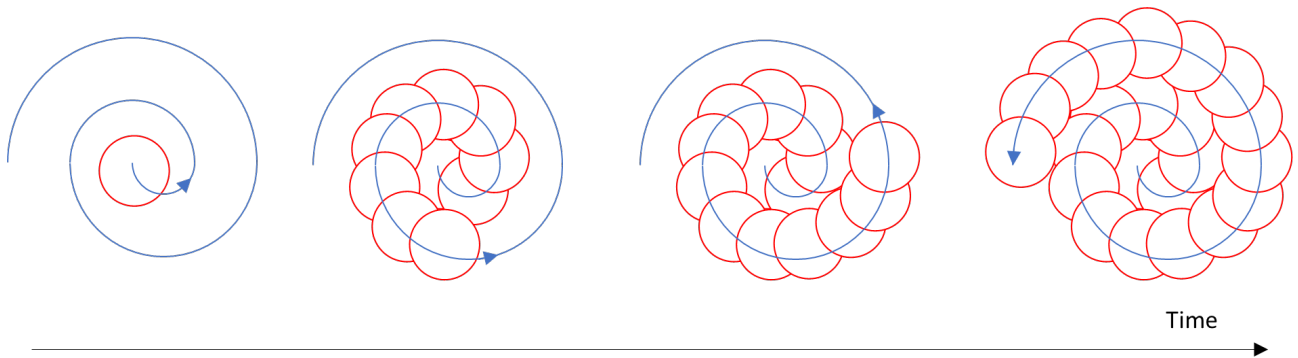


Figure 3.9: Spiral scan performed by the transmitter satellite.

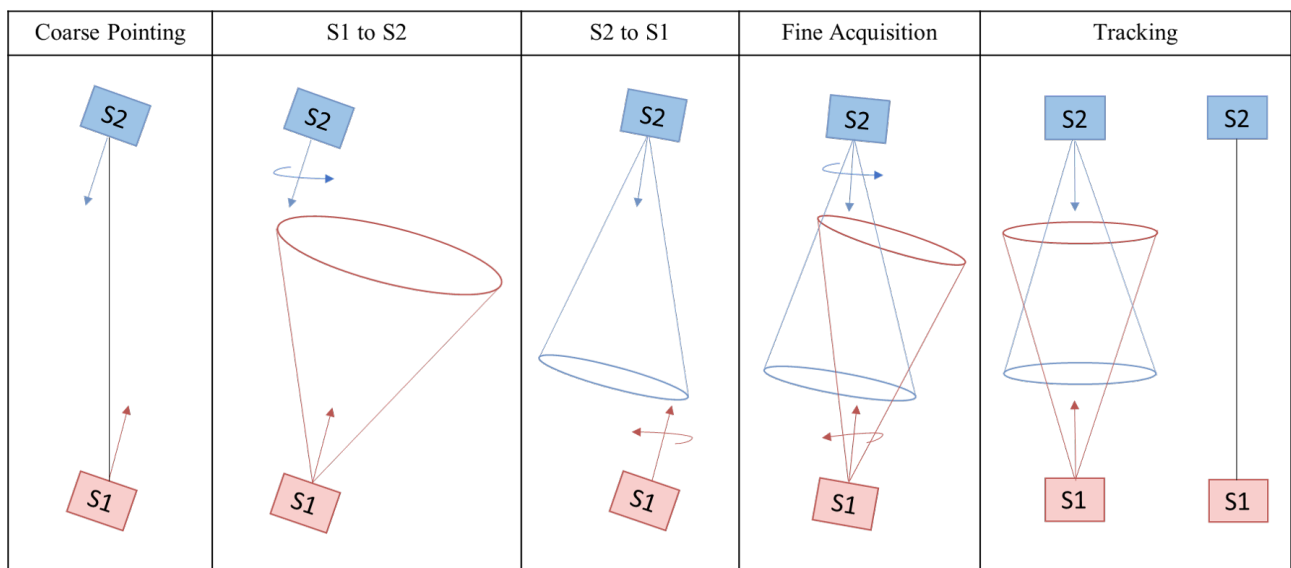


Figure 3.10: Acquisition strategy for line of sight alignment between satellites S1 and S2.

3.2.3 Tracking

In the tracking mode, a link between the two satellites has been established. There is a continuous beam of light on all the detectors. A closed loop tracking is initiated with the tracking detector and the FSM and CPA. The FSM adjusts for small errors and the CPA comes in if the error exceeds the range of FSM.

3.3 Conclusion

The layout of the laser terminal was studied to understand the different optical components, detectors, mechanisms and laser. The PAT strategy was studied to understand how two satellites establish a link.

Chapter 4

State of the Art: Refocusing mechanisms

In this chapter, refocusing mechanisms for a Cassegrain and Cassegrain-like telescopes are discussed. The focus of this survey is to study the different actuators and mechanisms used to refocus space telescopes. At the end of this chapter a comparison is made for the different mechanisms found in literature.

- What are the state of the art on axis telescope refocusing mechanisms used in space application?
- What are the actuators used for refocusing?
- What are the possible locations for placing the mechanism?

4.1 Refocusing mechanism for the Solar Orbiter mission

A refocusing mechanism was developed for the Full Disk telescope within the Polarimetric and Helioseismic Imager on a solar orbiter mission [22]. The goal of the mechanism was used to obtain focused images of the Sun. The refocussing was used to compensate for defocus induced by after launch misalignment, thermal drifts and moisture release from the satellite structure.

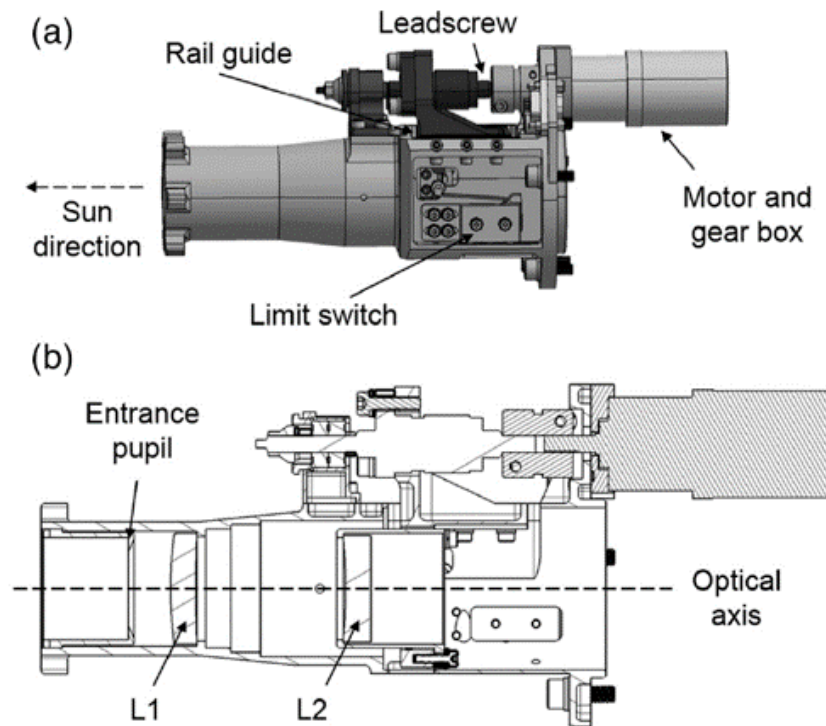


Figure 4.1: Refocusing mechanism for the Solar Orbiter mission [22] (a) CAD model (b) Cross section view

The telescope that was used is a refractive consisting of two lenses L1 and L2 as shown in figure 4.1. The mechanism is employed on lens L2. The lens is actuated by a leadscrew which is coupled to a stepper motor with a gearbox and guided by a linear crossed roller rail.

The metric used to determine focus is image contrast. Multiple images are taken while scanning the L2 range. The position of the stage which corresponds to highest contrast is the position of best focus.

4.2 In-orbit refocusing mechanism for SpaceEye-1

A refocusing mechanism was developed for an Earth observation satellite flying in Low Earth Orbit [23]. The satellite had a two mirror telescope design with a Carbon Fiber Reinforced Plastic(CFRP) metering structure. A well known issue with CFRP is that they absorb moisture from the atmosphere on ground and release it in vacuum. The reason for installing a refocusing mechanism was to compensate for the change in M1-M2 distance due to after launch shrinkage of the metering structure.

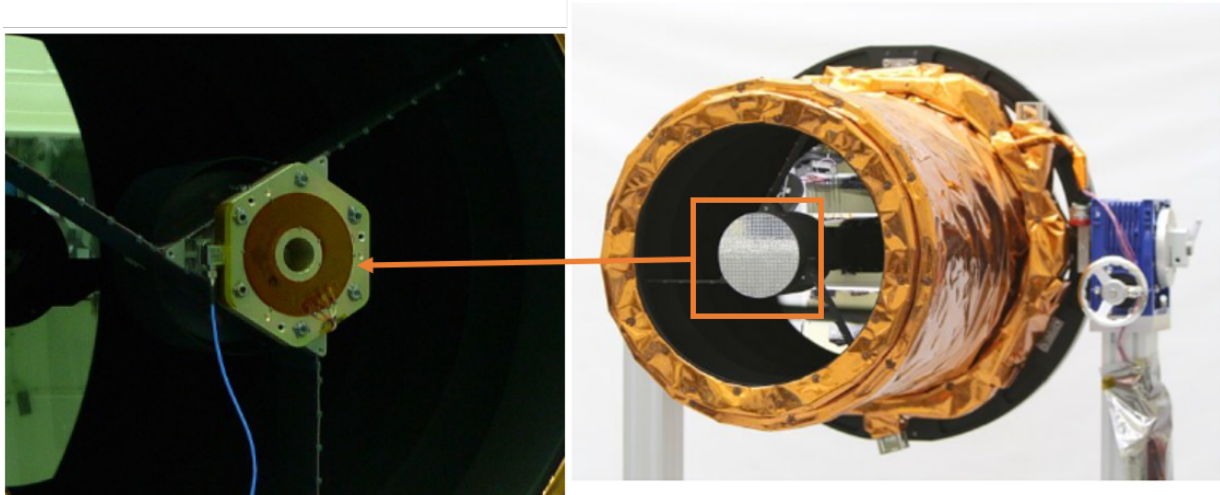


Figure 4.2: Refocusing mechanism on the SpaceEye-1. Image on the left shows the refocusing mechanism installed on the secondary mirror. Image on the right shows the telescope. [23]

A thermal actuator is attached to the M2 mirror as shown in figure 4.2.

4.3 CHEMCAM autofocus mechanism

A refocusing mechanism was developed for a Chemical Camera (CHEMCAM) on-board the Curiosity Rover deployed on Mars [24]. The rover has a two mirror telescope. The purpose of the autofocus mechanism is to focus on a chosen target on the Mars surface.

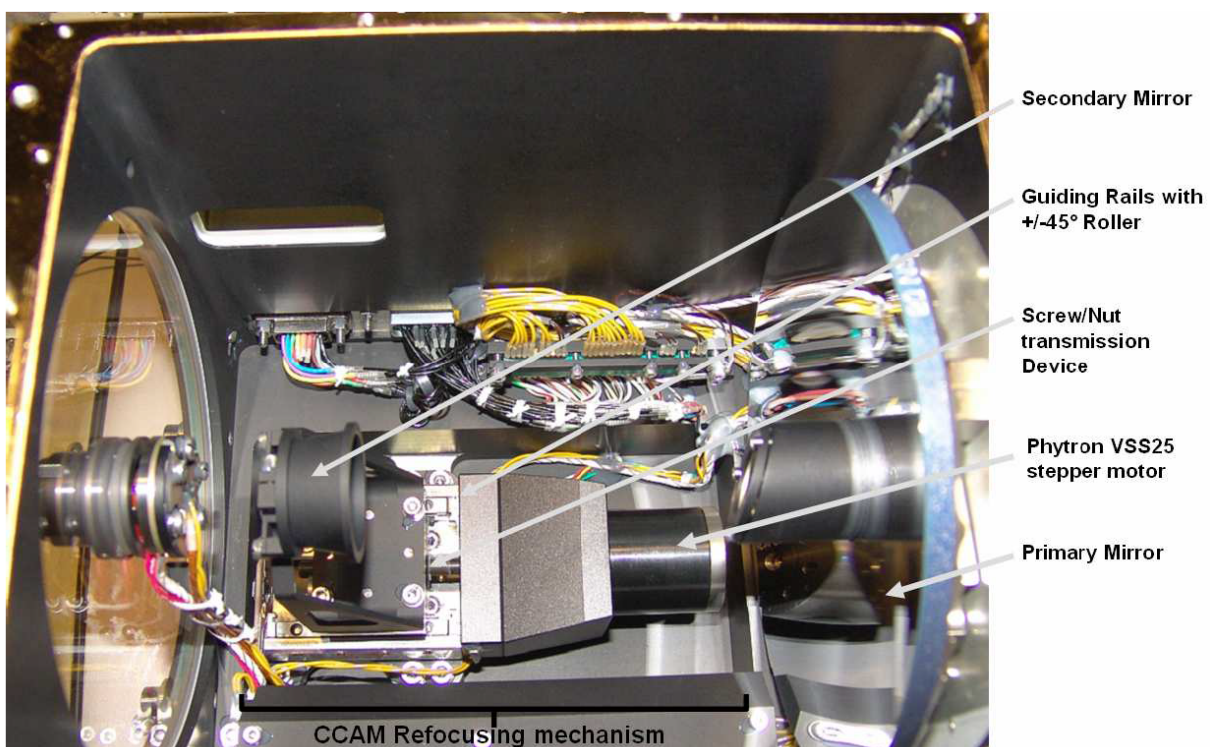


Figure 4.3: Refocusing mechanism on the Curiosity rover [24]

The M2 mirror is driven with a leadscrew actuated by a stepper motor and guided by linear crossed rails as shown in figure 4.3.

4.4 Refocusing mechanism for EO telescopes

A refocusing mechanism was developed for an Earth Observation satellite [25]. The satellite was equipped with a Korsch type four mirror reflective telescope. The refocusing mechanism was installed to compensate long term thermal effects, moisture release from structure and launch induced deformation.

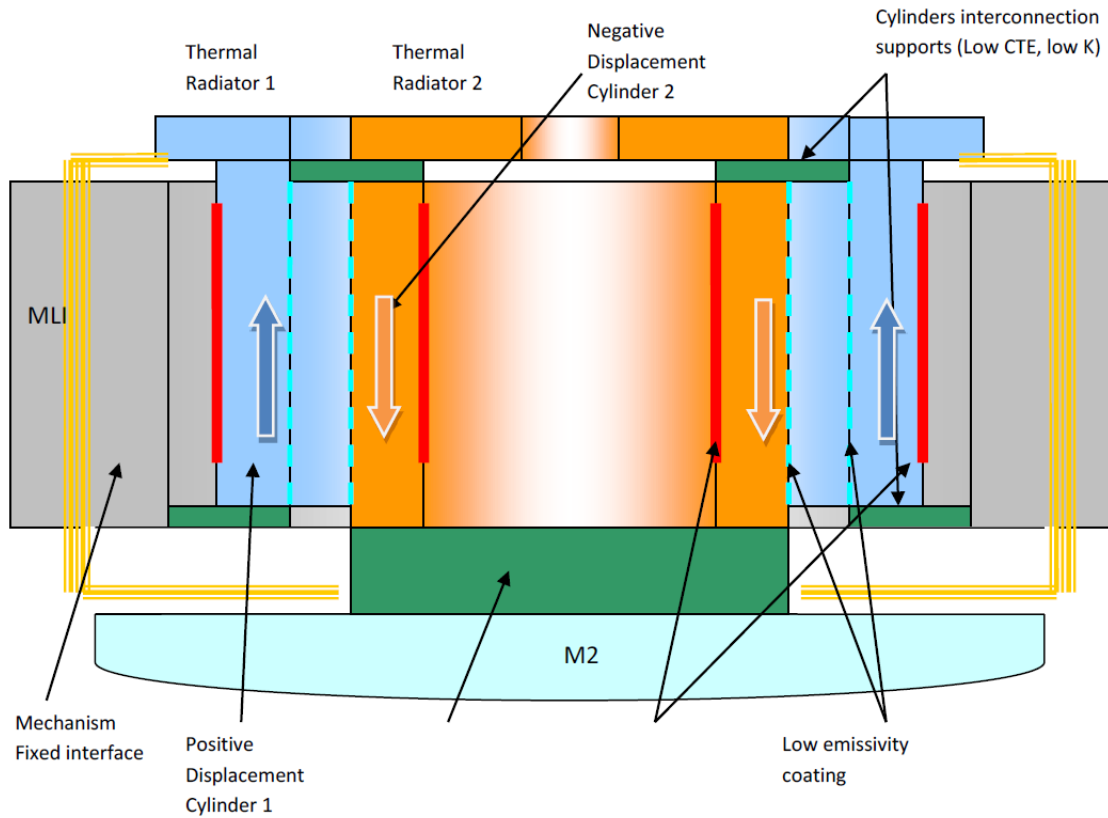


Figure 4.4: Cross section of a refocusing mechanism for an Earth Observation satellite [25]. The colour code for the figure is as follows: Blue: outer cylinder, Orange: Inner cylinder, Green: Connections, Grey: Fixed, Red: electrical heater patch, Yellow lines: Multi-layer insulation, Dashed blue lines: Low emissivity coating. Arrows indicate direction of movement.

The refocusing mechanism was installed on the M2 mirror. The M2 mirror was fixed on a thermal actuator. The actuator works on the principle of expansion/shrinkage of a material on heating/cooling. A schematic diagram of the actuator is shown in figure 4.4.

The mechanism consists of two concentric cylinders. Electrical heater patch is attached on the circumference of the cylinders and a thermal radiator is located on the top of the mechanism. Heater is used to expand and the radiator is used to shrink the cylinder along its length respectively.

The double cylinder design has the following advantages compared to a single cylinder design.

1. Better dynamic performance: The cylinders move in opposite direction to cancel out vibrations.
2. Electrical heater can be used to move the mechanism in both directions whereas a single cylinder design has to rely on thermal radiator for a change in direction of movement.

4.5 Thermal refocusing method for spaceborne imagers

A refocusing mechanism was developed for a Earth observation camera deployed in space. The imager consists of a Korsch type reflective telescope shown in figure 4.5. The refocusing was done to compensate for moisture

release from the CFRP telescope structure.

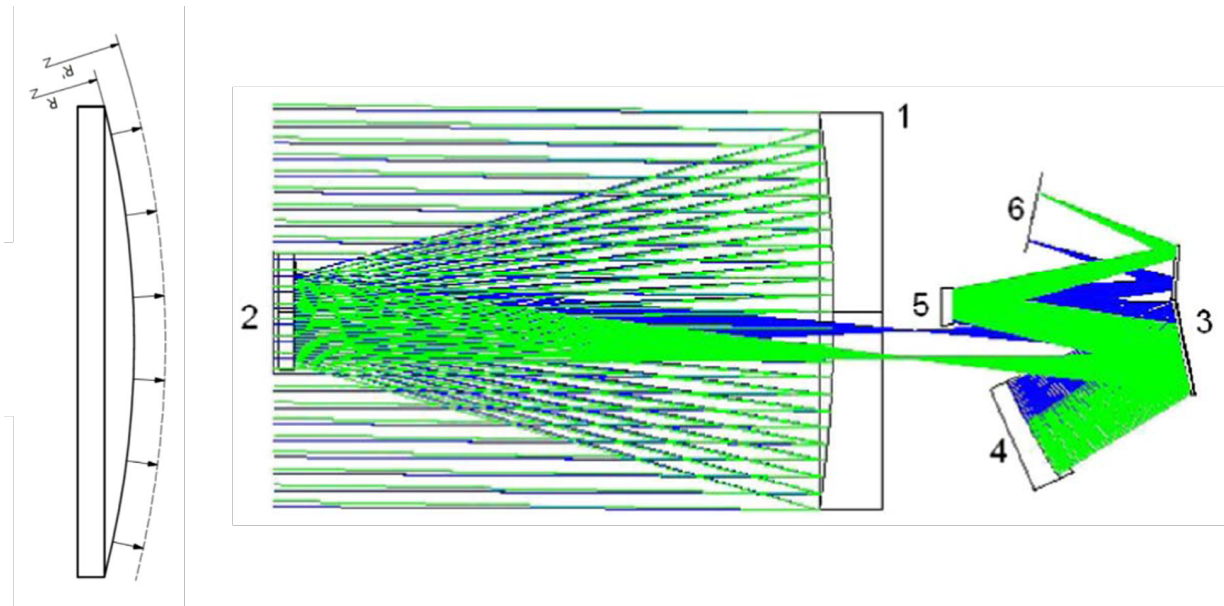


Figure 4.5: Refocusing mechanism with a thermal actuator on the M2 mirror for a Korsch telescope [26]

The refocusing mechanism was installed on the M2 mirror. The actuator works on the principle of thermal expansion. As the temperature of the mirror is changed, its radius of curvature changes and thereby changing its focal length. A schematic diagram of the telescope and the actuation principle is shown in figure 4.5.

4.6 Piezoelectric refocusing mechanism

A piezoelectric actuator made by Cedrat Technologies has been used for a refocusing mechanism [27]. This actuator has been used by EADS-SODERN which is a part of Ariane group, a supplier of space optronics. The actuator has been tested to by space evaluation program according to European Space Agency (ESA) standards.

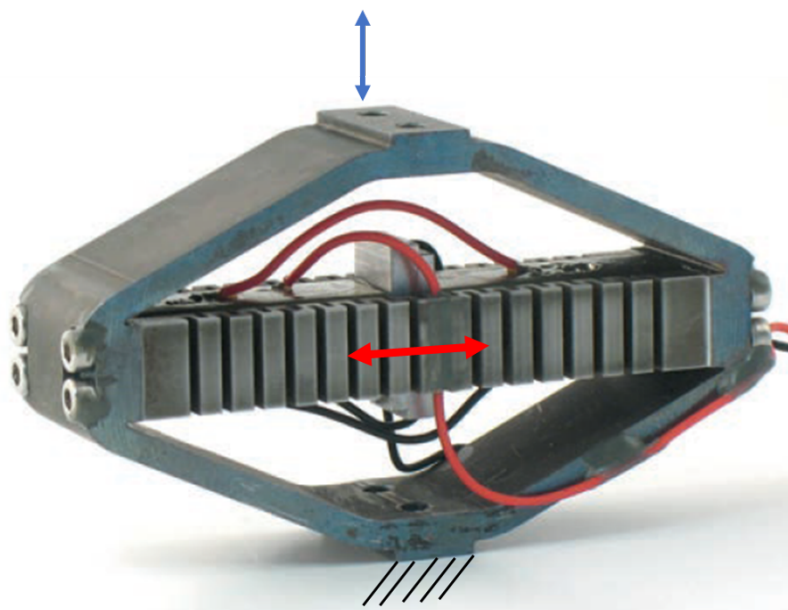


Figure 4.6: Shell type piezoelectric actuator fixed at the bottom. Red arrow shows the movement of piezoelectric material and blue arrow shows the movement of the top surface where a mirror can be mounted [27].

4.7 Comparison and summary

	1	2	3	4	5	6	7
Title	Solar Orbiter	SpaceEye-1	CHEMCAM	EO telescope	Spaceborne imager	Meteosat 3	Cedrat
Actuator	Stepper	Thermal	Stepper	Thermal	Thermal	Stepper	Piezoelectric
Optical element actuated	L2	M2	M2	M2	M2	M2	-
Figure of merit	image contrast	WFE	autofocus	-	MTF	WFE, IE	-
Range	4 mm	2.5 μm	15 mm	15 μm	30 μm	150 μm	130 μm
Precision	25 μm	-	5 μm	100 mm	-	0.06 μm	-
Stability	-	-	3 μm for 10 sec	-	-	-	-
Advantages	COTS	No lubricant	COTS	No lubricant	No lubricant No launch lock No aging	COTS Monolithic structure	COTS No lubricant
Disadvantages	Backlash	Thermal insulation	Backlash	Continuous power Thermal insulation Thermal radiator	Continuous power	Lubricant	Hysteresis Aging

Table 4.1: State of the Art refocusing mechanism comparison

There are three types of actuators used for a refocusing mechanism found in the literature: stepper motor, thermal actuator and a piezo-electric actuator. It is clear from table 4.1 that thermal actuator is robust in a sense that it neither suffers from backlash, hysteresis, aging nor does it require lubricant, launch lock. This makes it attractive for space application. However, it's drawback is that it is inherently slow. The range of this type of actuator is in the order of magnitude of $10 \mu m$.

Stepper motor is the tried and tested option but suffers from backlash. This can be a problem if the refocusing mechanism requires bi-directional movement. Backlash can be compensated but it adds up to the overall alignment time. The motor requires lubricant for its bearings. This can be a problem from cleanliness point of view. If the particles settle on the optics it will deteriorate the optical performance. The range of motion of this type of actuator is in the order of magnitude of millimeters.

Piezo-electric actuators are fast, easily available but suffer from hysteresis and aging. Hysteresis can be compensated by the controller but requires an accurate model. The range of this actuator is in the order of magnitude $100 \mu m$. The resolution is not given in the paper but typically it is in the order of magnitude of 10 nm .

In conclusion, a thermal actuator is a good candidate if the movement of the mechanism is slow. A piezo-electric actuator could be a good choice for a faster operation with fine resolution. Electro-magnetic actuators like a Lorentz force, reluctance force actuator although not found in literature specifically for a RFM could be a potential candidate.

It is clear from literature that the M2 mirror is the choice to place the refocusing mechanism.

4.8 Conclusion

In literature, refocusing mechanisms are used to correct focus error in space telescopes for imaging application. However, there is no refocusing mechanism found in literature used for laser satellite communication. So, it is not clear if one of the existing solutions can be directly applied to our application. This leads to the research question: How to adapt a refocusing mechanism for a laser satellite communication terminal? To answer this question, a system design needs to be carried out. This leads to the following three research sub-questions:

1. Can we use the onboard detectors to close the loop?
2. How the RFM will operate in the existing PAT strategy?
3. What is the best place to place the refocusing mechanism?

These questions will be addressed in Part II of this thesis.

Part II

Refocusing System Design

Chapter 5

Defocus detection

In this chapter, the propagation of the Rx laser beam through the optical system is simulated to quantify the detectable defocus. The following research questions are evaluated in this chapter.

- What is the range of defocus that can be measured with the onboard detectors?
- What is the amount of defocus that can be tolerated by the Rx beam and the Tx beam?

5.1 Rx beam simulation

In this section, the Gaussian beam visualized and its governing equations are introduced. These equations are applied for the simulation for calculating the beam spot at focus for the Rx beam.

5.1.1 Gaussian beam spot at focus

The intensity profile of a Gaussian beam at focus is given by using following equations.

$$I(r, z) = \frac{2P}{\pi w_z^2} \times e^{-\frac{2r^2}{w_z^2}} \quad (5.1)$$

$$D_0 = \frac{4\lambda f}{\pi D_b} \quad (5.2)$$

$$z_r = \frac{4\lambda f^2}{\pi D_b} \quad (5.3)$$

$$D_z = D_0 \sqrt{1 + \left(\frac{z}{z_r}\right)^2} \quad (5.4)$$

Symbols

f : focal length of the focusing mirror/lens.

λ : wavelength of light.

D_b : collimated beam diameter before the focusing lens/mirror.

D_z : beam diameter($1/e^2$) at an axial distance z from best focus.

w_z : D_z or $1/e^2$ beam radius at a distance z.

r : radial distance from optical axis in a plane perpendicular to the axis.

P : optical power incident on the mirror/lens.

I : intensity of light.

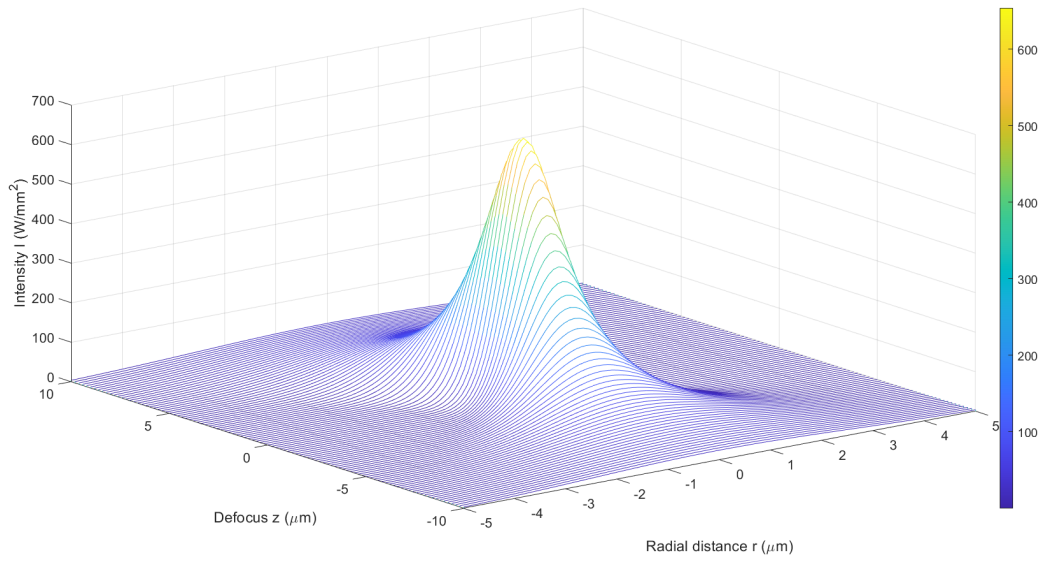


Figure 5.1: Gaussian laser beam through focus.

5.1.2 Optical fiber coupling efficiency

A measure of focus alignment is coupling efficiency. Here, a simulation is carried out to plot coupling efficiency as a function of defocus.

The fiber coupling efficiency is given by the overlap integral of the electric field profiles of
 1) the laser beam at its focus which is a Gaussian and
 2) the mode distribution of the fiber which is also a Gaussian.

The mode distribution of a fiber is given by equation 5.5.

$$\eta = \frac{|\iint E_1(x, y) \cdot E_2(x, y) dx dy|^2}{|\iint E_1(x, y)|^2 dx dy \cdot |\iint E_2(x, y)|^2 dx dy} \quad (5.5)$$

A typical fiber coupling efficiency curve as a function of spot size is shown in figure 5.2.

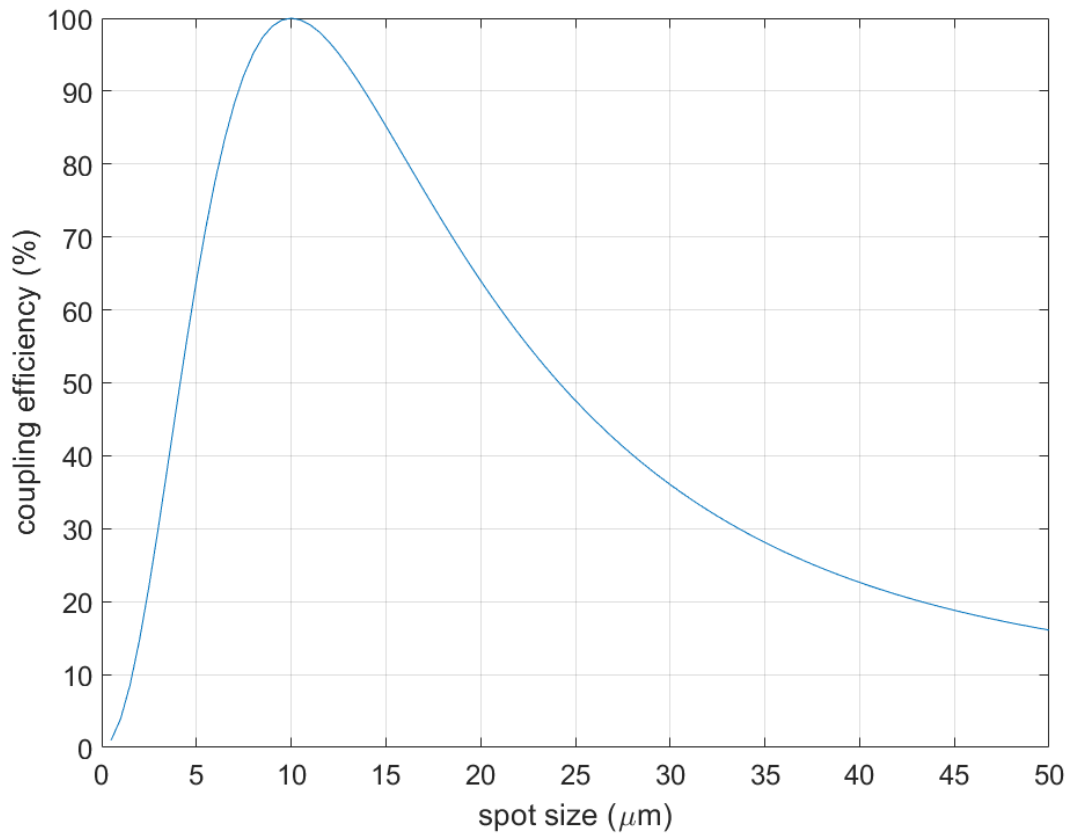


Figure 5.2: Gaussian fiber coupling

The original optical system consists of a lens group. The function of these lenses is to collimate the Rx beam and to correct for aberrations. In this simulation the optical lens group is replaced by a single lens to perform the function of collimating the laser beam. This is a valid assumption because the ray transfer matrix simulation operates in the paraxial regime. The schematic of the optical system analysed for the fiber coupling efficiency simulation is shown in figure 5.3.

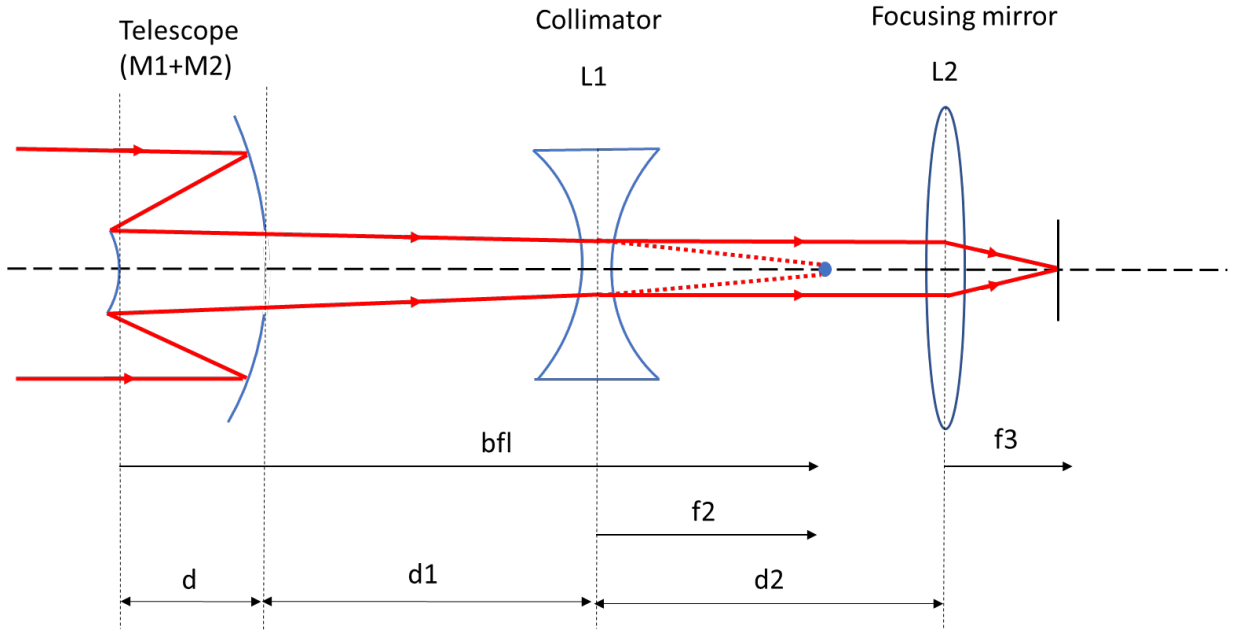


Figure 5.3: Optical system for Rx beam optical fiber coupling efficiency simulation. The schematic is not to scale.

In the simulation all the optical elements are fixed and only the M2 mirror is moved along its optical axis. The propagation of light through the optical system is modeled with ray transfer matrices. The ray transfer matrix for a lens and free space propagation is given by equations[28] 5.6 and 5.7 respectively.

$$\begin{bmatrix} 1 & 0 \\ -\frac{1}{f} & 1 \end{bmatrix} \quad (5.6)$$

$$\begin{bmatrix} 1 & d \\ 0 & 1 \end{bmatrix} \quad (5.7)$$

To model the optical system, the ray transfer matrices are multiplied and the final equation is given by equation 5.8.

$$\begin{bmatrix} u_2 \\ \theta_2 \end{bmatrix} = [L2][D2][L1][D1][M2][D][M1] \begin{bmatrix} u_1 \\ \theta_1 \end{bmatrix} \quad (5.8)$$

Here, u_1 is the ray height measured from the optical axis and θ_1 is the angle made by the ray with the optical axis. This is shown in figure 5.4.

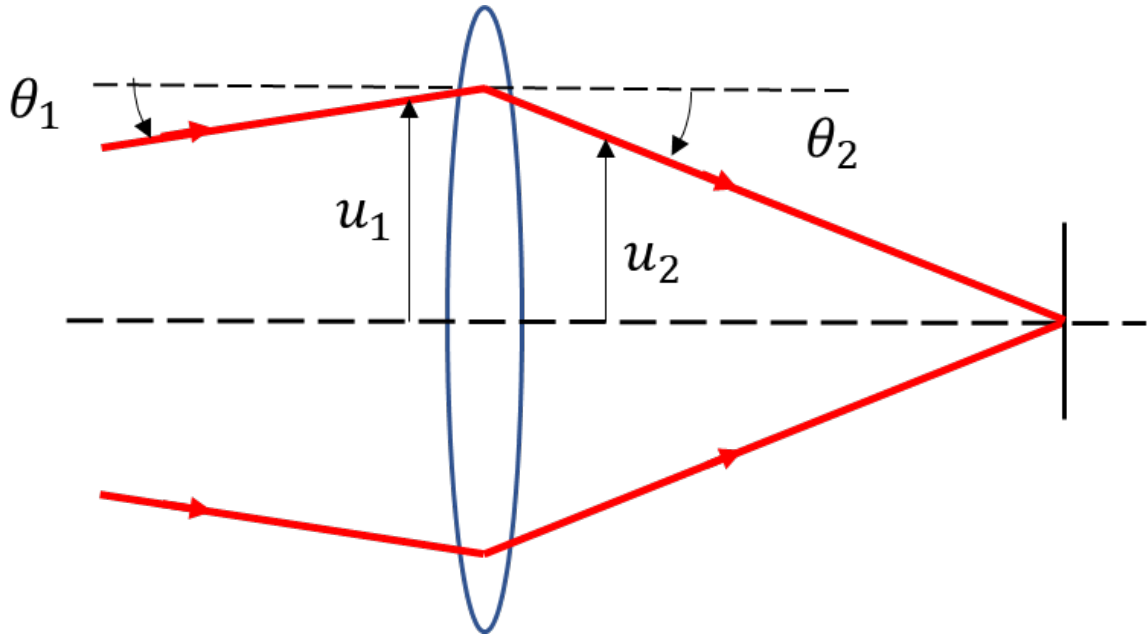


Figure 5.4: Ray height(u) and ray angle(θ) for a beam passing through a lens.

Further, the angle θ_2 and image height u_2 are used to calculate the image position given by equation 5.9

$$s_i = \frac{u_2 f_{L2}}{\tan(-\theta_2)} \quad (5.9)$$

This image distance is used to calculate the electric field distribution of the Gaussian spot at focus given by equation 5.10[29]

$$E_s = \sqrt{\frac{2}{\pi}} \frac{1}{w_z} e^{-\frac{(x^2+y^2)}{w_z^2}} \quad (5.10)$$

The field distribution for a single mode fiber is given by equation 5.11[29]

$$E_f = \sqrt{\frac{2}{\pi}} \frac{1}{w_f} e^{-\frac{(x^2+y^2)}{w_f^2}} \quad (5.11)$$

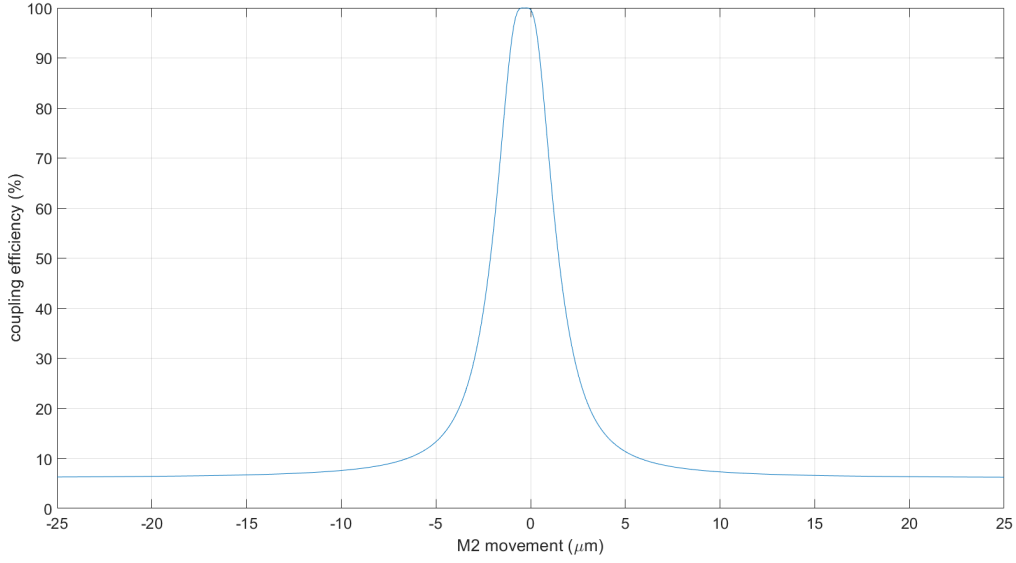


Figure 5.5: Fiber coupling efficiency as a function of M2 mirror movement.

The fiber coupling efficiency as a function of M2 mirror movement is shown in figure 5.5. From the figure it is clear that coupling efficiency decreases as the mirror moves away from the nominal position. The M2 movement that can be detected by the optical fiber is the sensitive part of the curve. Therefore, the detectable range is $\pm 5\mu\text{m}$.

5.1.3 Camera spot size

The Rx laser beam spot size can also be determined by the ACQ camera. The Gaussian beam propagation is given by equation 5.1.

The optical power received by a pixel is converted to gray scale. This is done because each pixel has a certain full well capacity and the camera has a Analog to digital converter. So, the camera can detect the signal in steps. The optical power is converted to number of photons by equation 5.12.

$$N_p = \frac{P}{\frac{hc}{\lambda}} \quad (5.12)$$

The pixels convert the photons to electrons with a certain coupling efficiency.

The conversion of number of electrons to gray scale is given by equation 5.13.

$$gray = \frac{N_e}{2^{12}} \quad (5.13)$$

The gray scale for seen by the pixels is shown in figure 5.6. Note that only a small portion of the camera is simulated because it is sufficient to capture the spot size and is computationally less expensive.

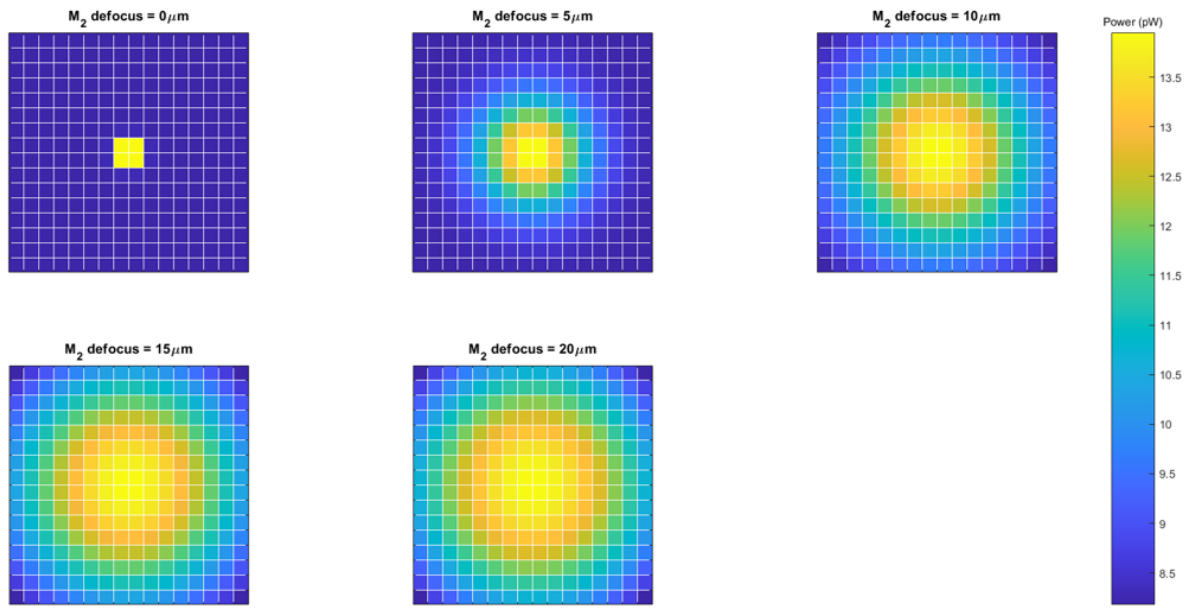


Figure 5.6: Spot size captured by the ACQ camera at different M2 defocus positions.

The gray scale for a horizontal strip of pixels passing through the center of the beam spot is shown in figure 5.7. From the figure it is clear that the detectable range is $\pm 100\ \mu\text{m}$.

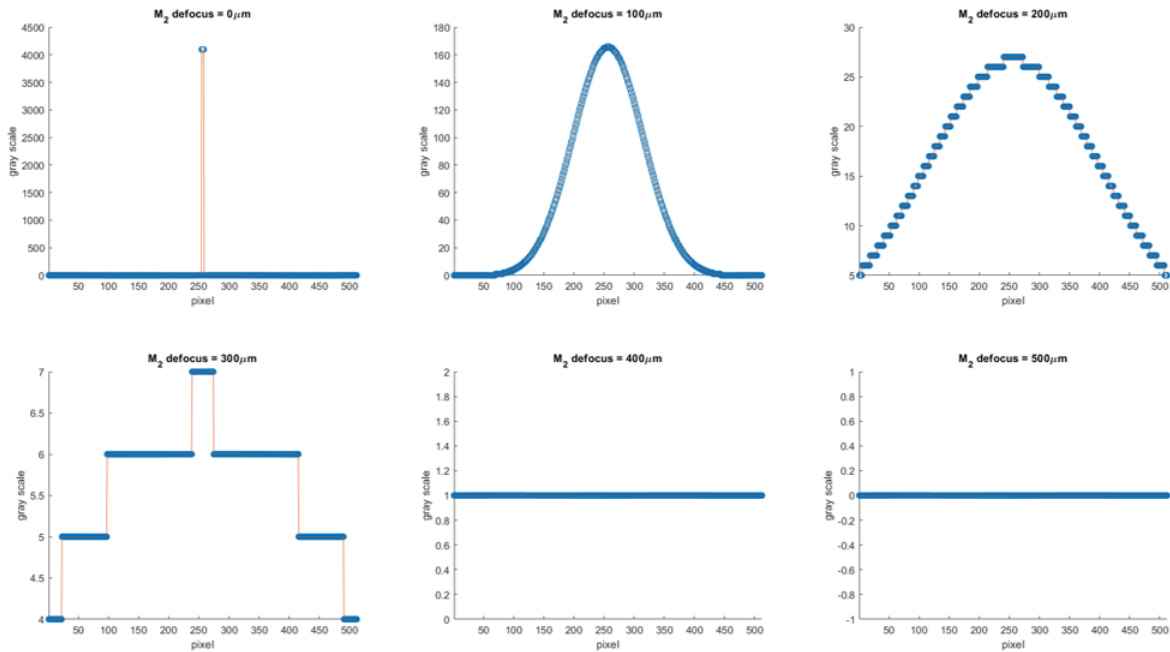


Figure 5.7: Spot size seen by the horizontal strip of pixels passing through the center of the beam spot at different M2 defocus positions.

5.2 Tx beam simulation

The telescope not only focuses the Rx beam but also collimates the Tx beam. Although the Tx beam is ideally collimated, in reality it has a finite divergence. So, it is important to know the divergence angle of the Tx beam. If the divergence is too large then the optical power at the partnering satellite may not be sufficient. The Tx

beam is simulated with Gaussian ray tracing matrices. Note that the Rx beam simulation was modelled by ray tracing matrix and not Gaussian ray tracing matrix because the Rx beam divergence may not be Gaussian. However, the Tx beam is Gaussian at the Tx telescope as well as the Rx telescope. The Rx telescope intercepts a portion of the Gaussian beam. Therefore, the Tx beam simulation is modelled with Gaussian ray tracing matrix. The schematic diagram of the optical system is shown in figure 5.8.

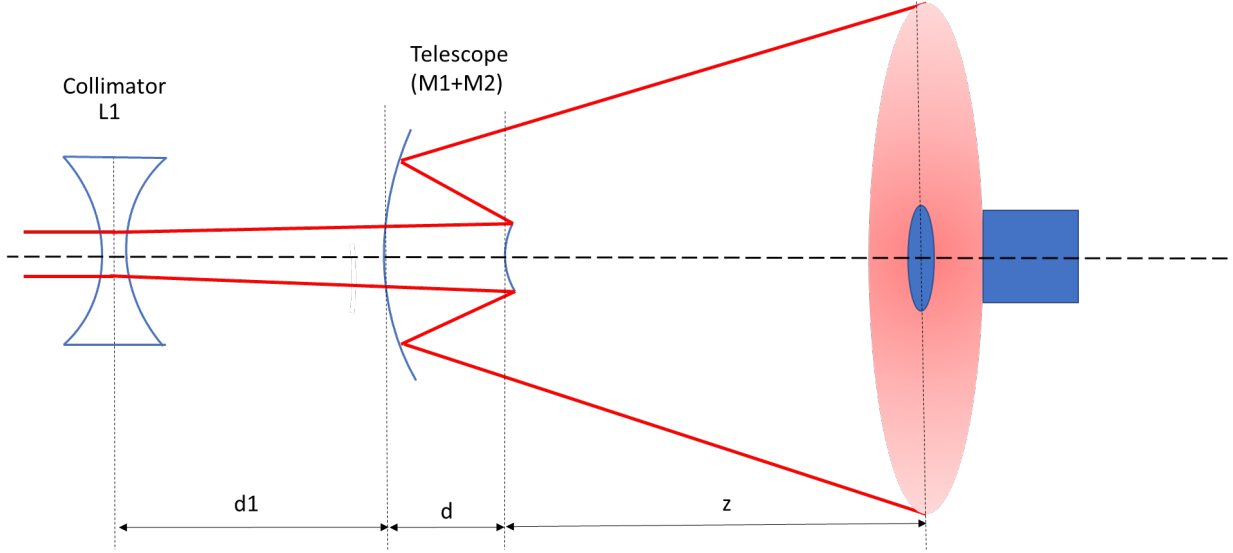


Figure 5.8: Schematic of the optical system used for Tx beam simulation.

The Gaussian beam propagation is modelled by complex beam parameter given by equation 5.14.

$$q = \left(\frac{1}{R} - \frac{i \cdot \lambda}{\pi \cdot w^2} \right)^{-1} \quad (5.14)$$

The ray tracing matrices used are identical to equations 5.6 and 5.8. The ray tracing matrix for the entire optical system is given by equation 5.15. The complex beam parameter at the image plane is calculated by equation 5.16.

$$\begin{bmatrix} a & b \\ c & d \end{bmatrix} = [Z][M1][D][M2][D1][L1] \quad (5.15)$$

$$q_2 = \frac{aq_1 + b}{cq_1 + d} \quad (5.16)$$

Once the complex beam parameter at the image plane is calculated we can extract the $1/e^2$ beam radius and beam radius of curvature which are given by equation[30] 5.17 and 5.18 respectively.

$$w = \sqrt{\frac{\lambda}{\pi \cdot \text{Im}\left(\frac{-1}{q_2}\right)}} \quad (5.17)$$

$$R = \frac{1}{\text{Re}\left(\frac{1}{q_2}\right)} \quad (5.18)$$

The power intercepted by the partnering satellite is calculated by equation 5.19 [30].

$$P = P_0 \left(1 - e^{-2\left(\frac{r}{w}\right)^2} \right) \quad (5.19)$$

where,

P : Optical power intercepted by the partnering satellite

P_0 : Tx laser power

r : radius of partnering satellite telescope

w : laser beam radius at the partnering satellite

The power intercepted by the partnering satellite as a function of M2 mirror movement is shown in figure 5.9. From the figure it is clear that the power intercepted decreases as the M2 mirror moves away from it's nominal position. It is assumed that 10% of the maximum power intercepted by the partnering satellite is the threshold. The M2 movement corresponding to this power level is $\pm 0.75\mu\text{m}$.

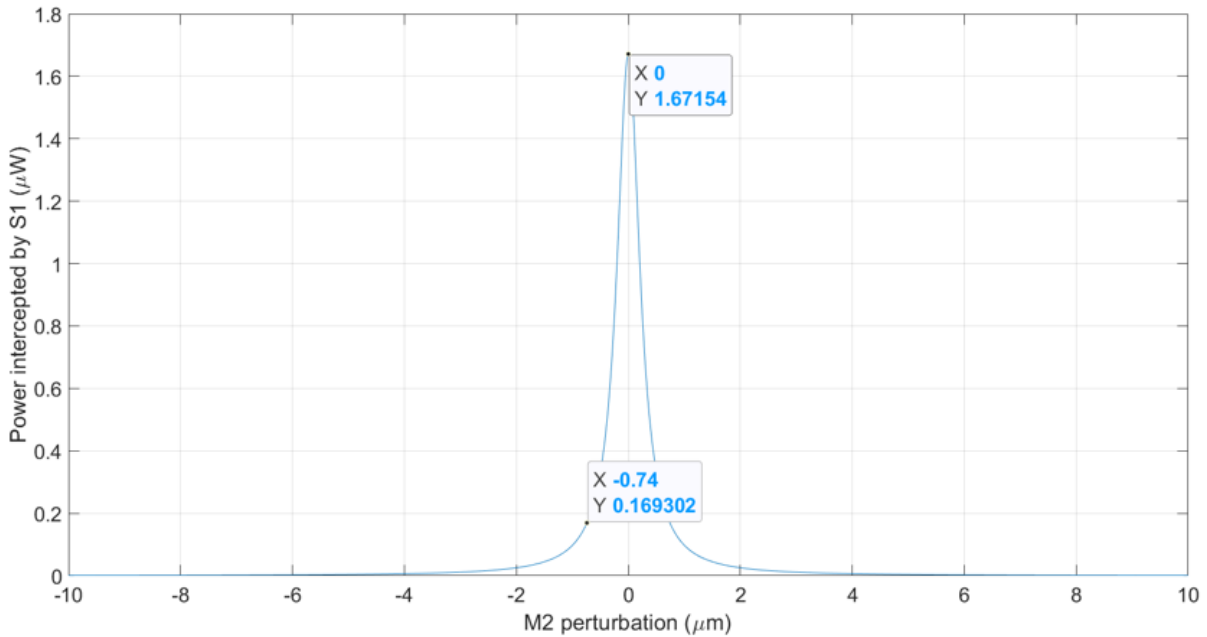


Figure 5.9: Power intercepted by the partnering satellite as a function of M2 mirror movement.

5.3 Conclusion

The Rx beam detectable range for the optical fiber is $\pm 5\mu\text{m}$ and for the ACQ camera is $\pm 100\mu\text{m}$. Therefore, the ACQ camera can be used to detect coarse defocus and the fiber to detect fine defocus. The Tx beam simulation shows that it is more sensitive to defocus compared to the Rx beam and therefore drives the resolution requirement for the RFM.

Chapter 6

Refocusing system operation

The chapter shows the different elements of the refocusing system and how they are work. This is done with the help of the following research questions.

1. What are the different elements of the refocusing system?
2. How could the refocusing system be adapted to work with the PAT strategy?

6.1 The refocusing system

The system breakdown with the inclusion of the refocusing system is shown in figure 6.1.

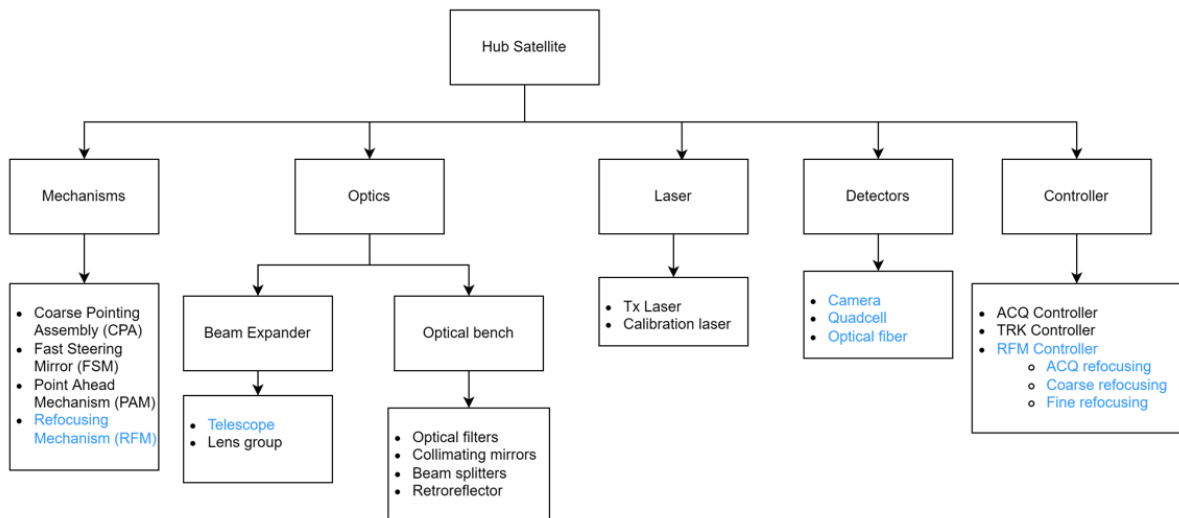


Figure 6.1: A system breakdown with the components of the refocusing system highlighted in blue.

The different elements of the refocusing system highlighted in the system breakdown are shown in figure 6.2.

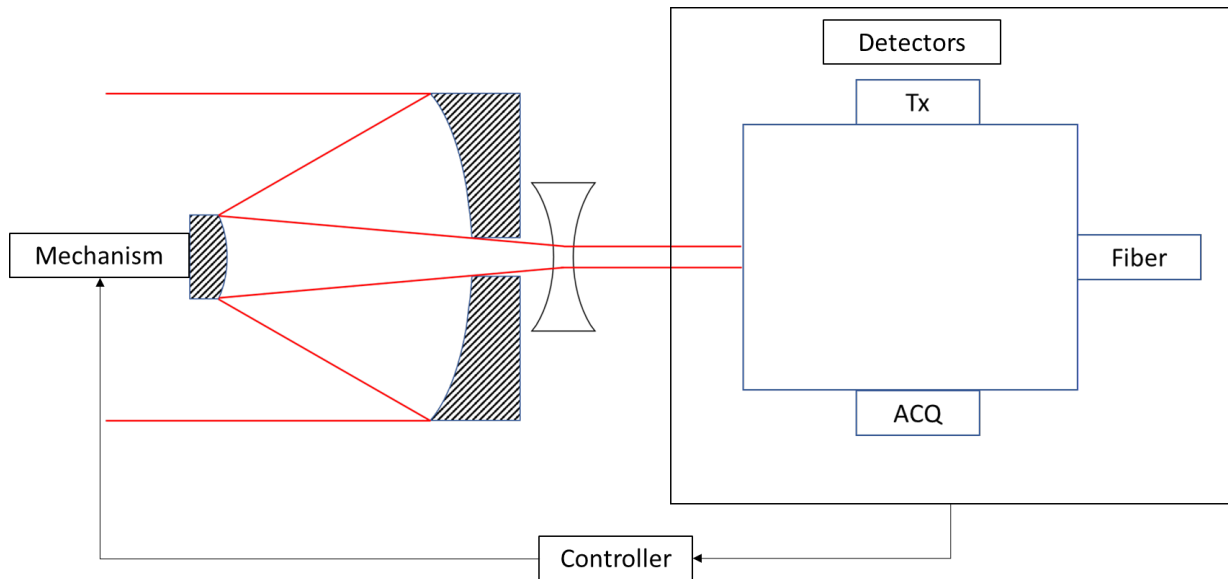


Figure 6.2: A schematic of the refocusing system.

The functions of the different components of the refocusing system are as follows. The refocusing mechanism consists of an actuator and a mechanical guidance. This is the part that generates the mechanical movement. The beam expander consists of the the telescope mirrors and the lens group. One of these will be actuated based on the trade-off. One or more of the on-board detectors will be used to get a feedback on the refocusing of the optical system. The refocusing will be controlled by two methods: extremum seeking control and a fiber alignment algorithm.

6.2 Use case scenarios

A system level design has been carried out to visualize how the refocusing mechanism will work in PAT strategy explained in section 3.2. The aim of this design is to identify key phases that drive the requirements of the mechanism. Two scenarios are conceived which could be adapted for the RFM.

6.2.1 Scenario 1

The working of the refocusing mechanism is shown in figure 6.3. The scenario consists of six phases which will now be explained one by one.

In the coarse pointing phase both UST and HST start pointing at the expected position of each other with their CPA.

The acquisition phase consists of two steps. In the first step of the acquisition phase the UST laser beam scans a circular area in a spiral pattern. This pattern is generated by controlling the PAM onboard the UST. The laser beam hits the ACQ camera of the HST for a short period of time during the scan which is called a blip from here on. The blip occurs when the two satellites momentarily align during the scan. The laser spot captured during the blip is used to check two conditions.

The first condition is whether the spot position on the ACQ camera is good enough to start the fine acquisition phase. Ideally the spot should be at the center of the ACQ camera for perfect line of sight alignment. If the line of sight alignment is not good enough then the fine acquisition phase will fail. If this condition is satisfied then the line of sight alignment is good enough to start the next step. However, if this condition is not satisfied then the line of sight first needs to be improved. This can be done by adjusting the mechanisms on HST. The CPA is used for coarse correction and the FSM for fine correction. After the alignment is complete, a spiral scan is performed again to check the blip's spot position. This loop is followed until the spot position on the ACQ camera is satisfactory.

The second condition concerns with checking the spot size of the blip for focus. If the focus alignment is not good enough then UST may not be able to detect HST laser beam in the next step of the acquisition phase. Multiple blips are required to determine the direction of movement for the RFM. Once the spot size is good enough the next step of acquisition is started.

In the second step of acquisition phase HST scans it's laser beam in a spiral pattern and UST detects a blip on it's ACQ camera. The position of the laser spot on the ACQ camera is captured and checked if it is good enough to start fine acquisition. If this is not the case then the scan is repeated until the position is improved. Note that there is no RFM on the UST.

The next phase is called fine acquisition which is executed to further improve the line of sight alignment and reduce the telescope focus error. In this phase HST and UST alternate as Rx and Tx. Here the steps for the case where UST is a Tx and HST is a Rx are described. The steps for the reverse case are identical with the exception of focus alignment.

The UST scans it's laser beam in a spiral pattern but now with a reduced scan size. HST detects the laser beam as a blip on it's ACQ camera. Two conditions are checked.

The first condition checks if the laser spot is within the FoV of the quadcell. This essentially means that the laser beam should fall on one or more quadrants of the quadcell. If this is not the case then the spiral scan is repeated until the spot is within the FoV of the quadcell.

The second condition checks if the spot size is sufficiently small to reduce the spiral scan size by a predefined step. If the condition is not satisfied then the RFM onboard the HST is adjusted and the spiral scan is repeated until the spot size is sufficiently reduced.

Once both the conditions are satisfied, the spiral scan size is reduced by a step and the two conditions are checked again. This is repeated until the spiral pattern of the laser beam converges to it's divergence angle.

At the end of this phase the quadcell should receive a continuous laser beam. This means that the fine acquisition phase is complete.

The next phase is tracking. In this phase the spot is locked in the XY plane (the plane of the tracking sensor) with a closed loop. Note that at this stage there might be very low or even zero signal at the optical fiber. The range of the RFM is scanned until there is maximum signal at the optical fiber. Extremum seeking control(ESC) is used position the RFM corresponding to best focus. A more detailed discussion about ESC can be found in 8. Now all the detectors, the ACQ camera, the quadcell and the optical fiber receive a continuous laser beam.

Now the satellites are ready for communication. The closed loop is used to keep the HST telescope in focus by correcting drifts. The tracking detector is operated in closed loop to maintain the line of sight alignment between the two satellites.

6.2.2 Scenario 2

The second use case scenario has seven phases. This scenario separates the two functions of line of sight alignment and telescope refocusing at a potential cost of additional hardware. The flowchart for this use case scenario is shown in figure 6.4. The working is explained in the following paragraphs.

The first phase consists of refocusing the telescope. The phase starts with switching on the calibration laser onboard the hub satellite. Note that the calibration laser has a slightly different wavelength which enables it to pass through the bandpass filter. The HST CPA is positioned to reflect the laser beam back to it's own telescope. A check is performed if there is enough optical power at the optical fiber. If there is no signal then the line of sight alignment between the laser and the optical fiber is improved. This can be done by positioning the laser spot at the center of the quadcell by correcting the position of the CPA and FSM. Once there is signal at the optical fiber extremum seeking control is used until the telescope is sufficiently focused to start the acquisition from UST to HST. At the end of this phase the telescope should be perfectly focused.

The next phase is the coarse pointing. In this stage the CPA of the HST and UST are positioned to point and track the position of each other.

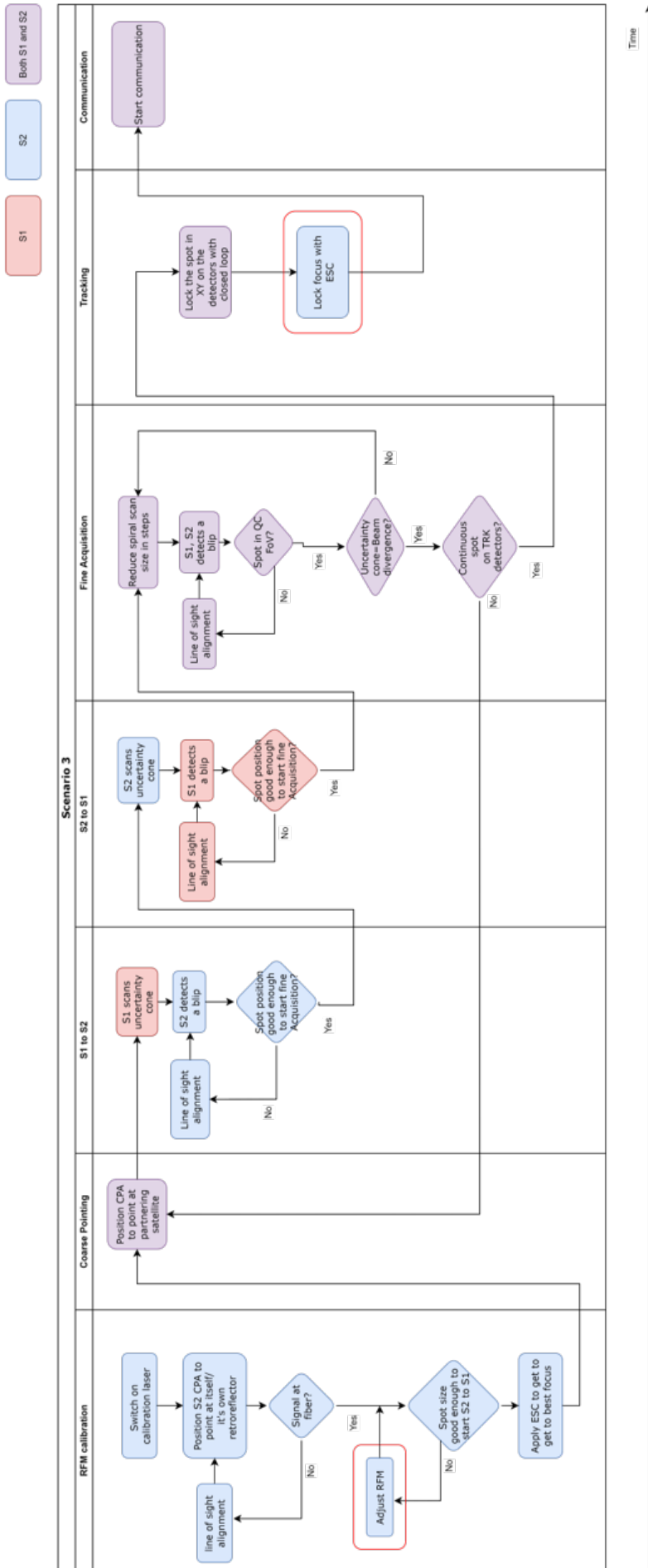


Figure 6.4: Use case scenario 2.

6.3 Conclusion

A system level breakdown is made to show the different elements of the Refocusing system. Two use case scenarios are designed which show how the RFM can be adapted to the PAT strategy. In the first scenario, the RFM alignment is done in parallel with the PAT. Alternatively, in the second scenario, the coarse focus alignment is done first and then the PAT is implemented. A fine alignment is carried out at the end in the tracking mode before start of communication. Another difference is that the second use case requires a retroreflector mounted on the satellite. This will add to the overall cost.

Chapter 7

Mechanism placement

In this chapter, the candidate optical elements for refocusing the optics are presented. A trade-off is carried out to choose the best option. This is done with the help of the following research questions.

- What are the candidate optical elements that can compensate defocus?
- What is the best location to place the refocusing mechanism?

The chapter starts with an overview of the optics in the system and the possible candidates for refocusing. The pros and cons of each candidate are described and a choice is made for the best optical element for refocusing.

7.1 Potential locations

The placement of the mechanism is a crucial decision which restricts the solution space and gives a clear direction for the concept design. There are four possibilities to compensate for the focus error arising due to the change in distance between the mirrors M1 and M2. The options are to individually move one of the following optical elements:

- M1 mirror
- M2 mirror
- A lens within the lens group
- The entire lens group

The mechanical overview of the terminal is shown in figure 7.1. The reasoning for the aforementioned candidates is elaborated in the following paragraphs.

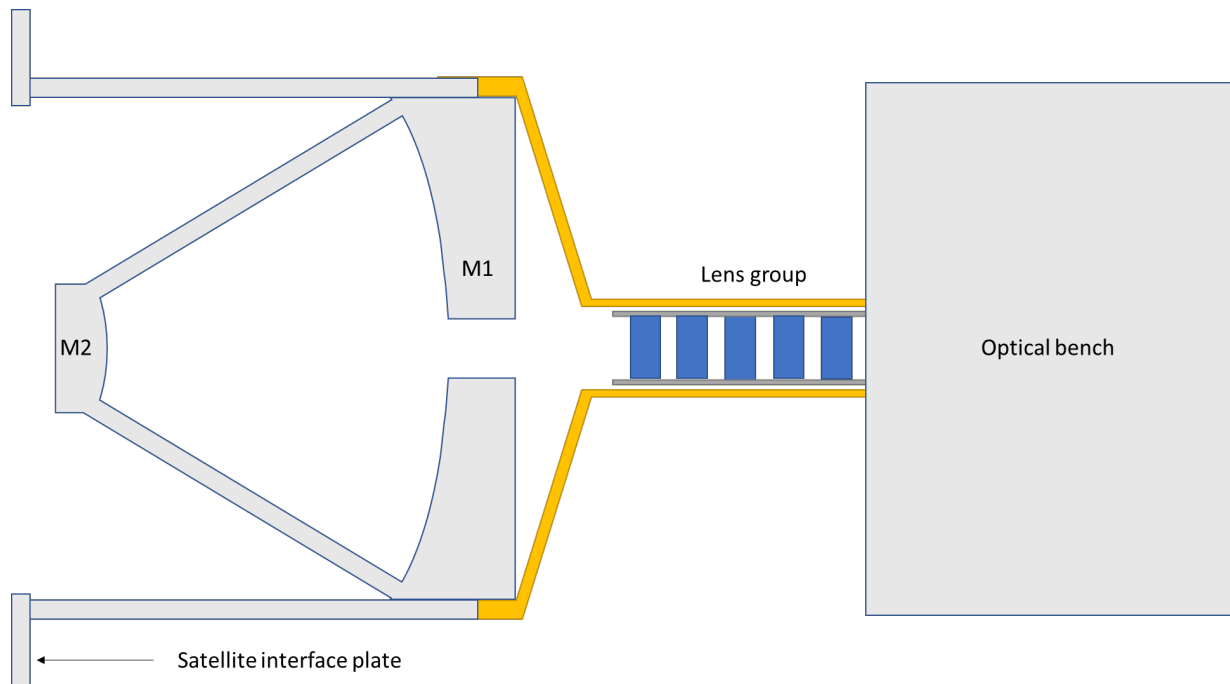


Figure 7.1: Terminal mechanical overview

M1 mirror

The M1 mirror is fixed to the satellite interface plate on one side in the baseline design. The optical bench is rigidly connected to the M1 mirror on the other side. Moving the M1 mirror has two downsides:

1) Make major changes to the baseline design.

This entails choosing alternative component(s) to fix. It is difficult to achieve this as the M2 mirror and the optical bench along with lens group lie on either side of the M1 mirror. Individually fixing these components to the interface plate can lead to relative motion between them which is undesirable in an optical system as it causes blur on the detector.

2) The moving mass(M1 mirror + lens group + optical bench) is too high and vulnerable.

The total mass is in the order of magnitude of kilograms which will require an actuator with a high force. This will lead to high power consumption which is undesirable. The concern of vulnerability stems from the fact that the optical bench houses sensitive optics and detectors. Repeatedly moving these can lead to optical misalignments which will degrade the optical performance of the system.

This leads to the conclusion that moving the M1 mirror is mechanically complex and is best avoided.

M2 mirror

The M2 mirror is attached to the M1 mirror by a spider with the shape of a tripod. The advantages of moving M2 mirror are the following.

1) Compact and lightweight.

The small size and low mass of the M2 mirror will require a low power actuator.

2) Small stroke

The M2 mirror has a high sensitivity to defocus. This means that a small movement of M2 can compensate a large focus error.

3) Modular design

The cassegrain telescope is a common design and a refocusing mechanism for the M2 mirror designed for this use case can be used for other cases irrespective of the optics that follow the telescope. Note that this is not the case with moving the lens group. The mechanism on M2 can possibly be also used for other applications like astronomy, earth observation, imaging, etc.

The disadvantages of moving the M2 mirror are the following.

1) Increase in telescope volume.

The mechanism for moving the M2 mirror will be mounted on top of the telescope. This will increase the overall telescope volume.

2) Increase in obscuration. The mechanism mounted on the M2 may obscure light. This is undesirable as it will reduce the number of photons in both the Rx and Tx beam.

In conclusion, a small moving mass with a small stroke means that a compact and power efficient mechanism can be employed at M2 to refocus the telescope.

A lens within the lens group

There are five lenses in the lens group. A solution is to move one of the lenses to refocus the telescope. However, it has a number of disadvantages listed below.

1) Additional aberrations

An optical analysis performed by TNO shows that refocusing with a single lens introduces other aberrations. This is of course undesirable because it degrades the optical performance of the overall system.

2) Limited space for movement

The stroke of the lens is limited by the neighbouring lens. As the sensitivity of individual lens is low, there is a possibility that to compensate for defocus the lens has to move beyond it's adjacent lens which is physically not possible.

Overall, this solution is not feasible.

The entire lens group

The final possibility is to move the lens group. The advantages for moving the lens group are listed below.

1) Low sensitivity to parasitic motion

The lens group shows very low sensitivity to decenter and tip-tilt motions. This means that the mechanism stability requirements are less stringent.

2) Overall telescope volume

There is sufficient space between the telescope and the lens group to place the mechanism. This means that adding the mechanism does not increase the overall volume of the telescope.

The disadvantages of moving the lens group are the following.

1) Large stroke

The sensitivity of the lens group is small. This means that a large stroke is required to refocus. Large displacement of the lens group will compensate for focus error but might introduce other optical aberrations which will degrade the performance. Large movement also means that the actuator will consume more power.

2) Non-linear sensitivity

The lens group exhibits a non-linear sensitivity to defocus. This means that it is difficult to control. Overall, placing a mechanism at the lens group is possible and mechanically desirable. However, the optical performance has to be judged to see if this solution is feasible.

7.2 Trade-off

In the previous section it was established that the possible solutions are moving the M2 mirror or the lens group. In this section these two are compared to select the best location to place the RFM.

The sensitivity table for the two optical elements is shown in table 7.1. In the table Dx and Dy represent decenter displacement. Dz represents the axial displacement. Rx and Ry represent the tip-tilt. It is seen that the sensitivity to WFE change in Dz is much higher for the M2 mirror compared to the lens group. The other important thing to note is that the WFE change of the lens group is non-linear.

		Minimum		Maximum	
		Value	WFE Change (nm)	Value	WFE Change (nm)
M2	Dx (mm)	-0.001	5.8	0.001	5.8
	Dy (mm)	-0.001	6.6	0.001	5.8
	Dz (mm)	-0.001	70.5	0.001	72.6
	Rx (deg)	-0.0012	1.7	0.0012	1.7
	Ry (deg)	-0.0012	1.7	0.0012	1.7
Lens Group	Dx (mm)	-0.001	0.0	0.001	0.0
	Dy (mm)	-0.001	0.0	0.001	0.0
	Dz (mm)	-0.001	2.1	0.001	0.2
	Rx (deg)	-0.0026	0.0	0.0026	0.0
	Ry (deg)	-0.0026	0.0	0.0026	0.0
		Minimum		Maximum	
		Value	WFE Change (nm)	Value	WFE Change (nm)
M2	Dx (mm)	-0.002	15.4	0.002	15.4
	Dy (mm)	-0.002	16.8	0.002	15.4
	Dz (mm)	-0.002	143.2	0.002	145.2
	Rx (deg)	-0.0024	6.0	0.0024	5.4
	Ry (deg)	-0.0024	5.4	0.0024	5.4
Lens Group	Dx (mm)	-0.002	0.0	0.002	0.0
	Dy (mm)	-0.002	0.0	0.002	0.0
	Dz (mm)	-0.002	4.2	0.002	2.2
	Rx (deg)	-0.0052	0.0	0.0052	0.0
	Ry (deg)	-0.0052	0.0	0.0052	0.0

Table 7.1: Sensitivity table for the mirror M2 and the lens group.

The conclusions from the sensitivity table along with other important properties considered for the trade-off are summarized in table 7.2.

Property	M2 Mirror	Lens group
Defocus sensitivity	High 68 nm WFE / μm	Low 0.163 nm WFE / μm
Decenter sensitivity	High 6 nm WFE / μm	Low 0.0002 nm WFE / μm
Obscuration	May increase	No effect
Mechanism size restriction	Must be compact in radial direction (<26 mm)	Must be compact in axial direction (<45 mm)
Mounting surfaces	Circumference, back surface	Circumference
Mass	Low 7.5 grams	High 15.33 grams

Table 7.2: Mechanism placement trade-off.

The distinguishing factor between the two is sensitivity in the Dz direction. The problem with the lens group

refocusing is that the sensitivity is non-linear. This was further investigated and the the optical model built by TNO shows that for the required displacement for the lens group corresponding to $\pm 30\mu m$ adds other aberrations which could exceed the WFE budget. These additional aberrations are not introduced when the M2 mirror is used for refocusing simply because refocusing the M2 brings the telescope to it's nominal position.

7.2.1 Conclusion

In conclusion, a high level trade-off was performed to eliminate the obvious candidates for the RFM. Two potential locations the M2 mirror and the lens group were identified. Finally, the M2 mirror was selected to place the RFM as the lens group refocusing adds other aberrations which could violate the WFE requirement.

Chapter 8

Extremum seeking control

The refocusing mechanism is required to search and maintain the best focus. A control algorithm to perform both these tasks is extremum seeking control (ESC). The chapter starts with the basic principle of extremum seeking control. Further, a simulation of the ESC is carried out to show it's working. Following research questions are evaluated.

- How does extremum seeking control work?
- Can the ESC work in presence of jitter signal?
- What are the mechanism requirements based on ESC?

8.1 Extremum seeking control

Extremum Seeking Control(ESC) is a gradient based real time optimization technique[31]. A key aspect of ESC is that it is adaptive which means it not only finds the optimum of the objective function but also tracks the optimum in response to drifts. Throughout this chapter we assume the extremum to be a maximum.

The control loop for ESC is shown in figure 8.1.

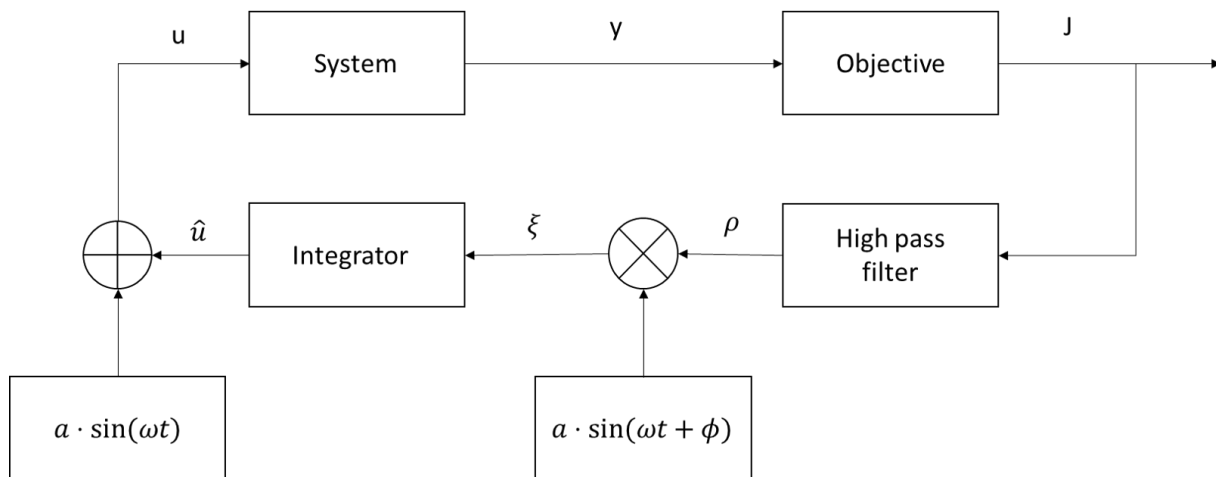


Figure 8.1: Extremum seeking control loop.

The meaning of symbols in figure 8.1 is as follows.

- u: system input signal.
- y: system output signal.

J : objective function to be minimized/maximized.

ρ : high pass filtered signal.

ξ : demodulated signal.

u^* : input signal corresponding to extremum objective function.

8.1.1 Working of ESC

The working of ESC is as follows [32]. The working follows the flow of signal as shown in figure 8.1.

Consider the starting point for the input at a point \hat{u} as shown in figure 8.2a. If we apply a sinusoidal perturbation to the input signal as shown in 8.2a then the corresponding objective function change is also a sinusoidal in phase with the perturbation. The objective function signal(J) is high pass filtered to remove the DC component. The filtered signal(ρ) is integrated with the perturbation. As both the signal are in phase, their multiplication(ξ) is positive as shown in figure 8.2b. This means that the slope of the objective function for the given point(\hat{u}) is positive and the magnitude of input signal must be increased to reach the maximum. Therefore, the sign of demodulated signal gives the direction of input signal movement. The demodulated signal is integrated to get the magnitude of change in the input signal. This magnitude is dependent on the slope of the objective function at that point.

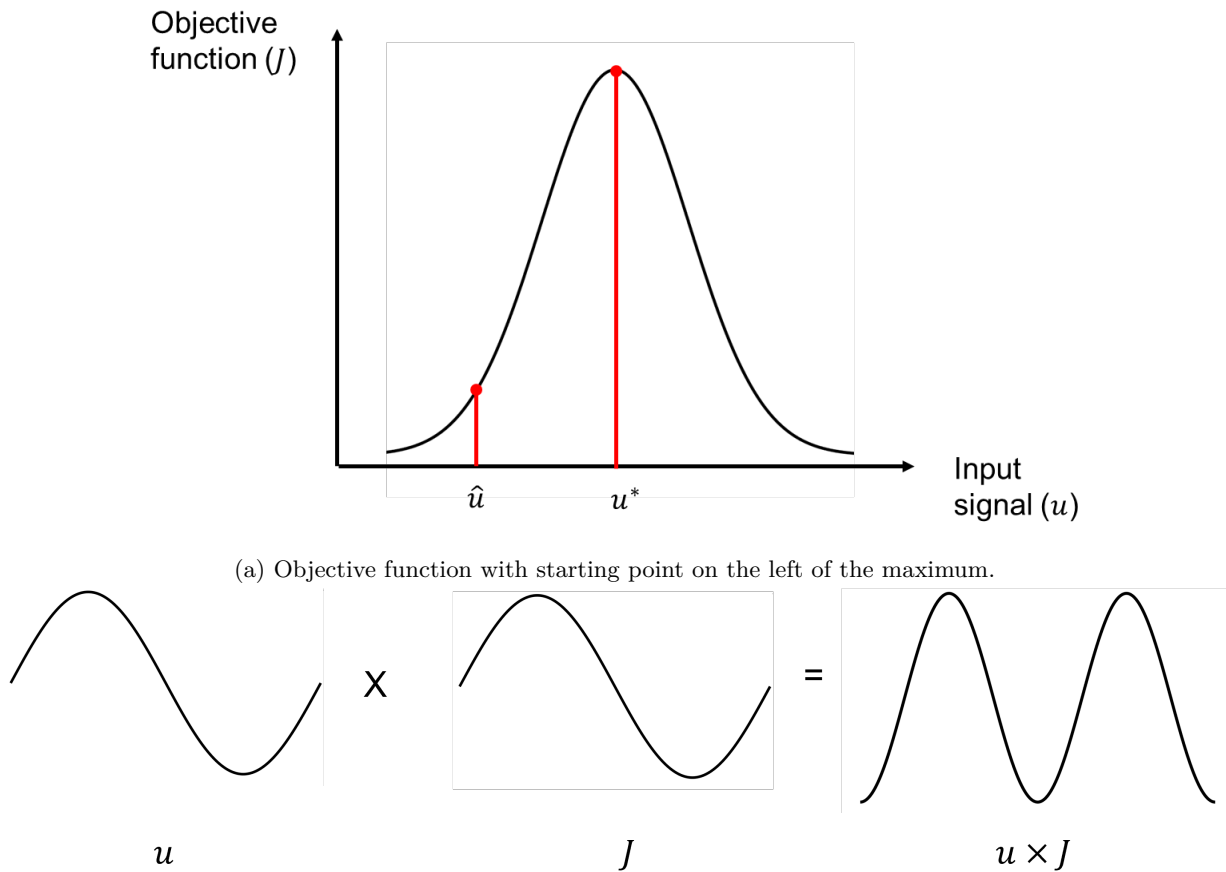


Figure 8.2: Extremum seeking control for $\hat{u} < u^*$

Similarly, if the starting point is on the right hand side of the maximum then signals u and J are out of phase and the sign of the demodulated signal is negative as shown in figure 8.3. This means that the magnitude of the input signal must be reduced. The change in magnitude of the input signal is obtained by integrating the demodulated signal with the input perturbation.

After the input signal reaches the peak of the objective function, the demodulated signal goes to zero and the input is said to be converged.

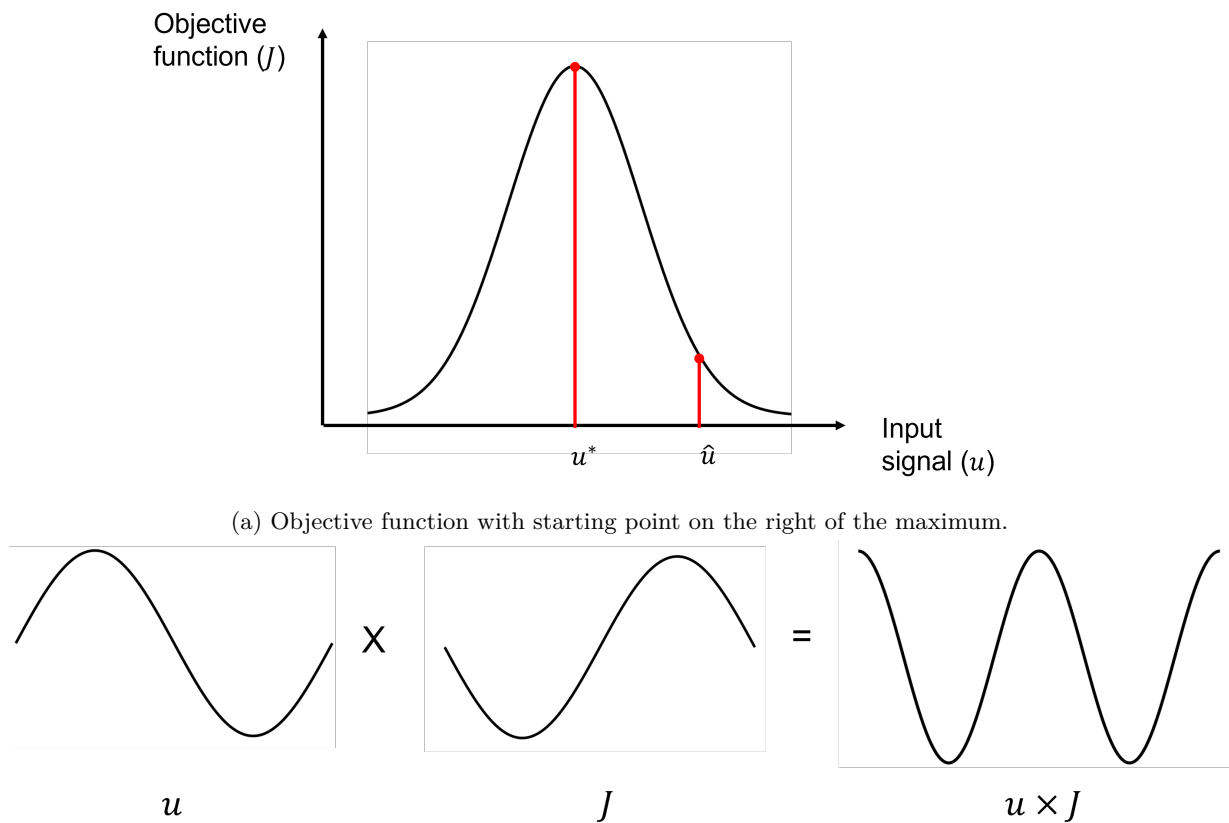


Figure 8.3: Extremum seeking control for $\hat{u} > u^*$

8.2 Simulink model

Extremum seeking control simulink block diagram is shown in figure 8.4.

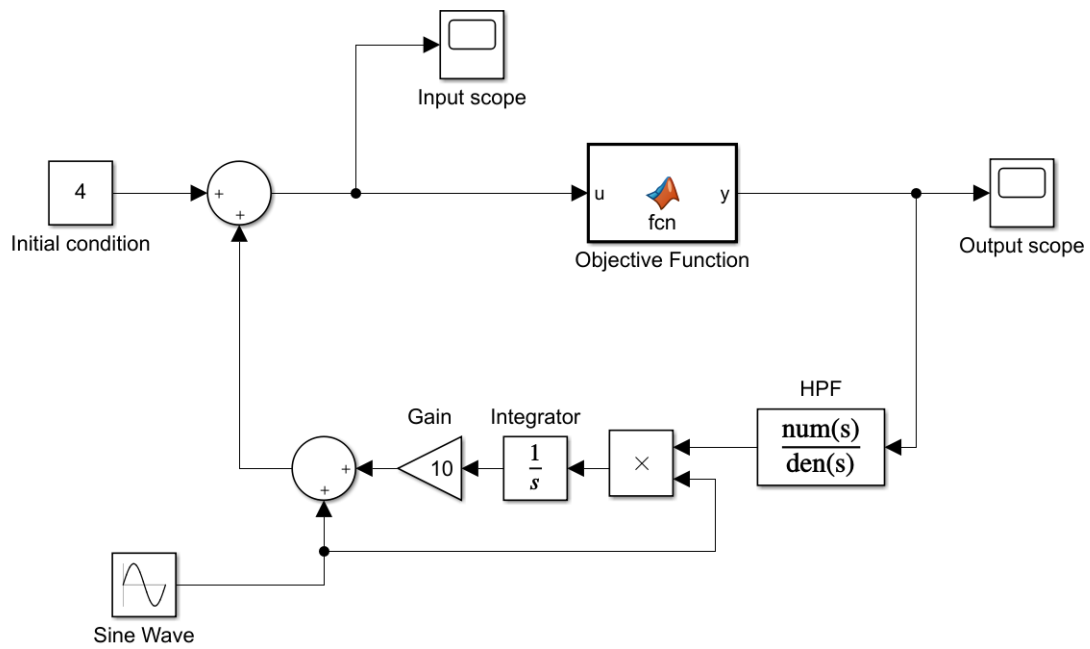


Figure 8.4: ESC simulink block diagram

The objective function for the ESC model is a Gaussian fit curve of the fiber coupling efficiency as a function of M2 mirror displacement shown in figure 8.5. The Gaussian function equation is of the form of equation 8.1.

$$y = d + a \cdot \exp -((x - b)/c)^2 \tag{8.1}$$

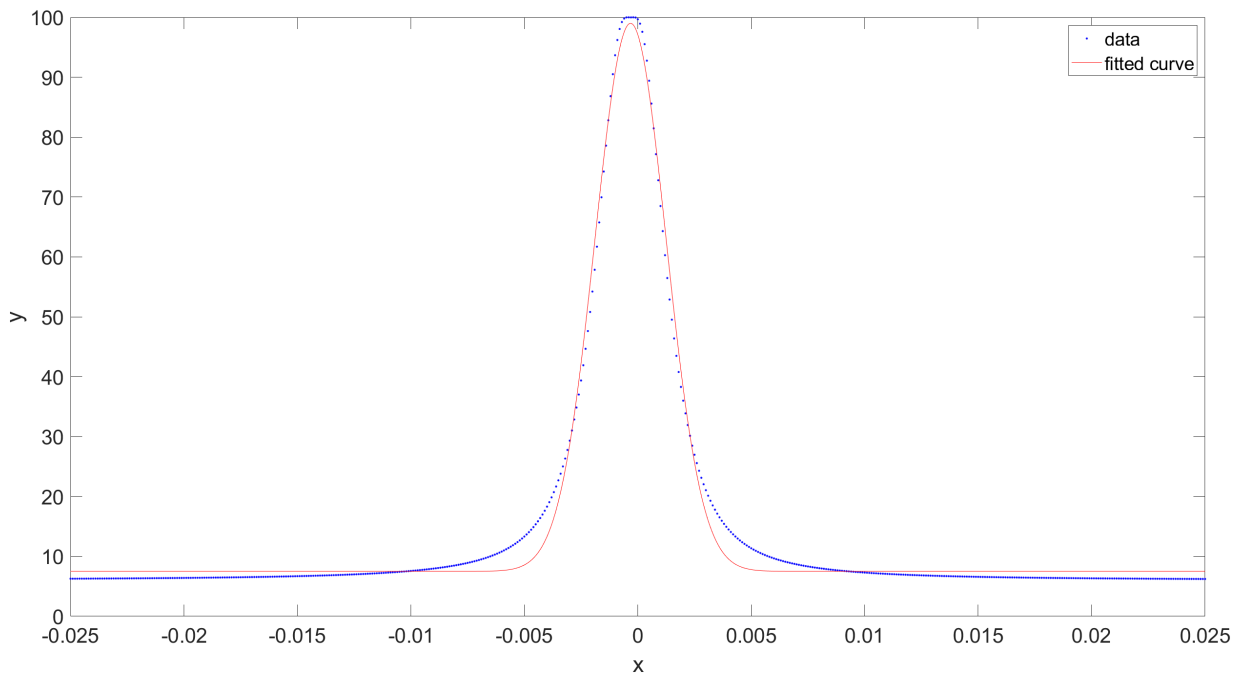


Figure 8.5: Fiber coupling efficiency as a function of M2 displacement fitted to a Gaussian.

8.3 ESC with white noise

The exact nature of the disturbances on-board is unknown therefore white noise is added to the control simulation to see if it affects the performance. The simulink model of the ESC with added white noise is shown in figure 8.6.

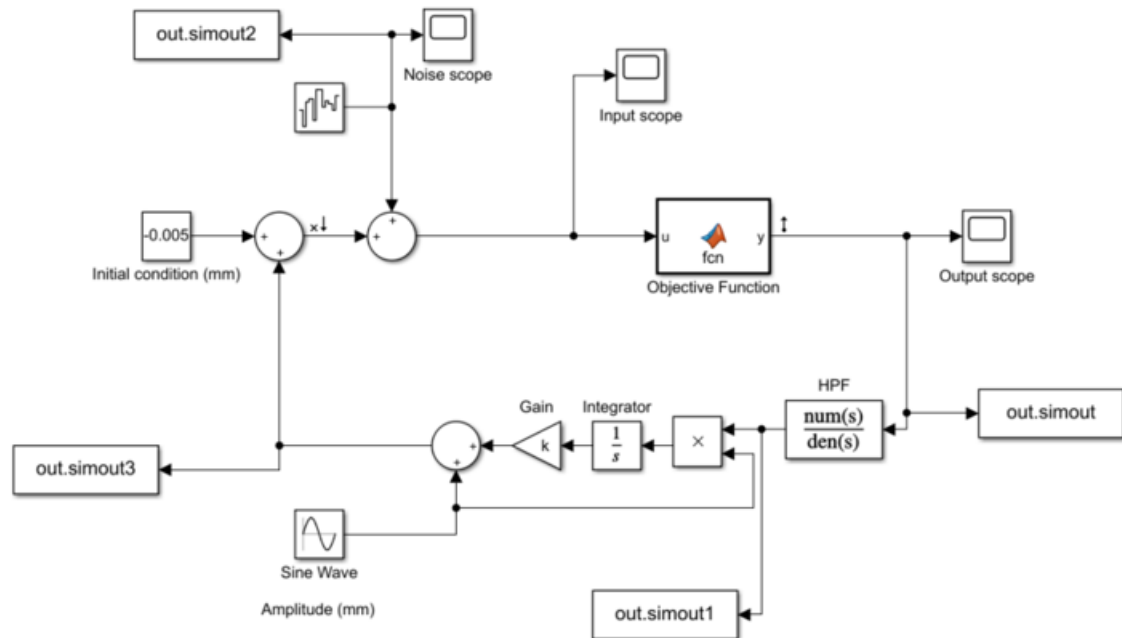


Figure 8.6: ESC with white noise simulink block diagram

White noise in time domain is shown in figure 8.7.

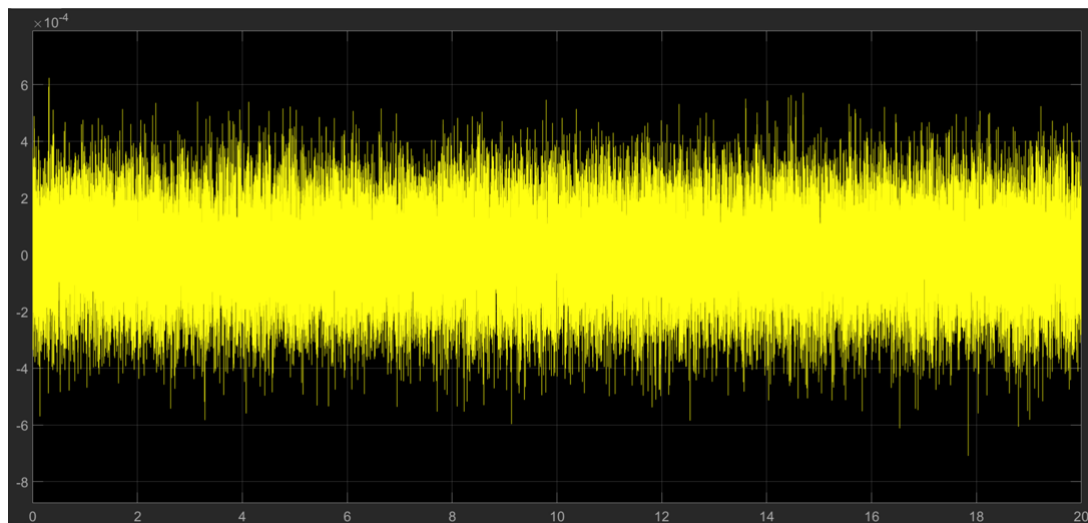


Figure 8.7: White noise in time domain y-axis: millimeters x-axis: seconds

The convergence of coupling efficiency without white noise is shown in figure 8.8.

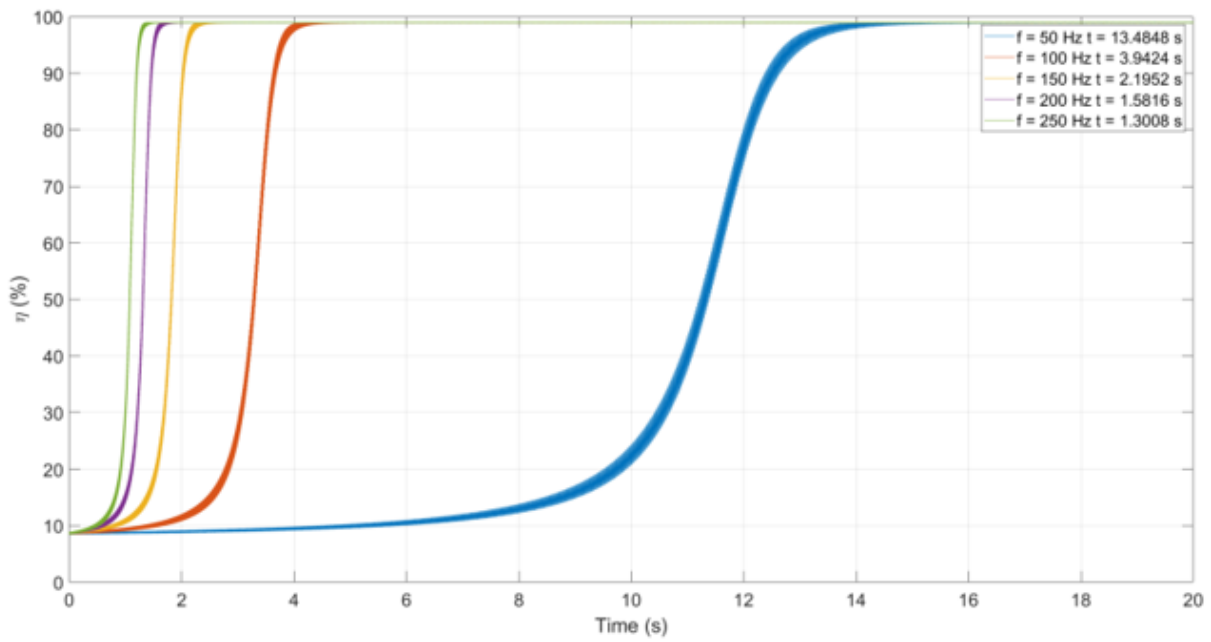


Figure 8.8: ESC without noise.

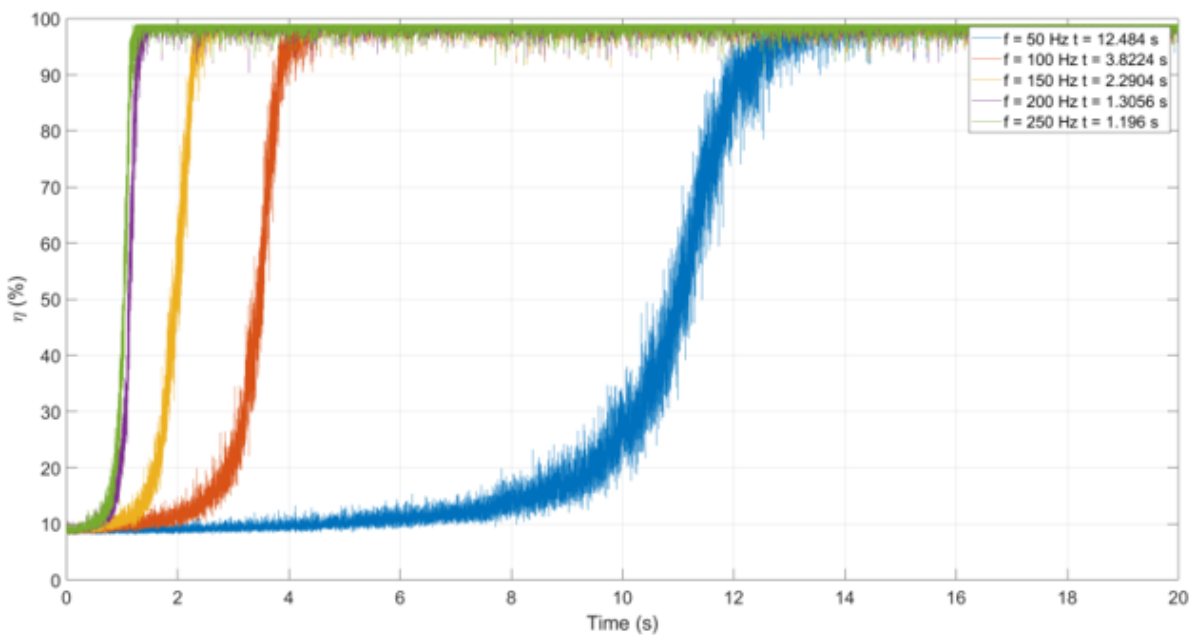


Figure 8.9: ESC with noise.

Figure 8.9 shows that ESC converges in the presence of white noise. Comparing this figure with the 8.8, it is evident that the ESC converges to the point of maximum coupling efficiency with a similar convergence time.

8.4 Requirement drivers

In this section a case is made for choosing the convergence time for the RFM. This choice directly drives two requirements namely, the mechanical dynamic performance and the resolution of the mechanism.

Convergence time

The pointing, acquisition and tracking strategy typically takes a minute to completely align two partnering satellites. Refocusing the telescope will take additional time. The total time available for the PAT and refocusing is assumed to be 90 seconds. The convergence time of the RFM is a part of this total time. The distribution of this additional 30 seconds used for refocusing depends on the use case scenario implemented.

8.5 Conclusion

Extremum seeking control can be used to maintain the telescope in focus with the refocusing mechanism. The simulink simulation shows that ESC can work in the presence of jitter signal. Requirements for mechanism resolution speed are derived based on the convergence time requirement.

Chapter 9

System requirements

In this chapter the operational and environmental requirements for the refocusing system are presented. The requirements are discussed one by one and have the following structure. First the requirement is defined, then the source of the requirement is presented. Finally a number is attached to the requirement. All the requirements are summarized in a table at the end of the chapter. During the project the possibilities for both the M2 mirror and the lens group were investigated. Even though it was shown in chapter 7 that M2 mirror will be actuated, here the system requirements for both the options is presented. The following research questions are evaluated in this chapter.

1. What are the system level operational requirements?
2. What are the environmental requirements?
3. What are the functional components of the RFM?

9.1 Operational requirements

The operational requirements concern the time frame after the laser satellite is in orbit. This includes the PAT strategy, actual communication and the idle time between communication.

Range

The range of motion required for the mechanism is based on two factors namely the change in distance between the two telescope mirrors due to gravity release. The launcher for the laser communication terminal is unknown at the time of writing so it is difficult to estimate a value. Therefore, it is assumed that this error is $\pm 10\mu m$ which is agreed upon with TNO.

The second factor that drives the range requirement is introduction of focus error due to the thermal load. A simulation has been carried out by TNO to quantify the focus error. The thermal load consists of the sunlight, earth albedo and earth IR incident on the telescope. The heat load changes as the satellite revolves around the earth. In the worst case scenario the the focus error introduced between the telescope mirrors is $\pm 20\mu m$.

Note that The gravity release is a one time event whereas thermal load is is a recurring event. In the worst case scenario, the total range of motion required will be the addition of these two factors which is $\pm 30\mu m$.

Minimum incremental motion

Minimum incremental motion is the theoretical value for a step that the mechanism can make. It is driven by the fraction of the sensitive part of the power curve for the Tx beam. It was shown in figure 5.9 that the sensitive part of the curve is within $\pm 0.75\mu m$ of the nominal position of the M2 mirror. It is assumed that the minimum incremental motion is a factor 100 times lower than this value.

Repeatability

Repeatability is the ability of the mechanism to repeatedly reach a number of points within its range with a certain deviation. This is important during the ACQ phase because there is no signal at the TRK detector and the RFM will work in open loop. It is assumed that the repeatability is a factor 10 higher than the minimum incremental motion.

ACQ stability

Acquisition stability is the ability of the mechanism to hold its position during the acquisition phase. The mechanism must maintain its position during the ACQ phase because the Rx signal is intermittent. This means that the mechanism has operated in open loop. If the mechanism moves outside the sensitive region of the Tx beam then the acquisition phase will fail. So, this is driven by the Tx beam curve. It is assumed that the mechanism must remain within $\pm 0.075\mu m$ during the ACQ phase. ACQ typically takes a minute to establish an inter-satellite link

Long term stability

Long term stability means the ability of the mechanism to hold its position between two consecutive links. It is desirable to reposition the stage faster so that the time required to establish a link is small. This is assumed to be a fraction of the Tx beam curve which is $\pm 7.5\mu m$.

Mechanical dynamic performance

Mechanical dynamic performance is the frequency with which the mechanism is expected to move to achieve refocus. This is driven by the control algorithm which determines the time required to refocus. An ESC simulation carried out in shows that the time required to refocus is 3.8 seconds which requires a jitter frequency of 100 Hz. Refer figure 8.9

Decenter

Decenter means the position error of the M2 mirror in the plane perpendicular to its optical axis that can be tolerated. It is driven by the WFE requirement of 100 nm RMS. The corresponding error motion is determined from the sensitivity table for the telescope which is $\pm 2\mu m$.

Tip-tilt

Tip-tilt is the angular position error of the M2 mirror about the axes located in a plane perpendicular to mirror's optical axis. The requirement is driven by the allowable WFE for the telescope. The allowable WFE is 100 nm which corresponds to $\pm 125\mu rad$ tip-tilt error.

All the values motivated are for the M2 mirror. However, the values for lens group depends on the sensitivity ratio of the M2 mirror and the lens group is a factor 270. Applying this factor, the values of lens group are calculated. The operational requirements for the refocusing mechanism are summarized in table 9.1.

	Requirement	Value for M2	Value for Lens group
1	Initial displacement [μm]	± 10 M2 movement(Assumed)	± 3500 LG movement
2	Motion range [μm]	$> \pm 20$ (thermal) + ± 10 (initial displacement) = ± 30 M2 movement	$> \pm 7000$ (thermal) + ± 3500 (initial displacement) = ± 11.5 mm LG movement
3	Minimum incremental motion [μm]	0.0075 M2 movement	2.6 LG movement
4	Repeatability [μm]	± 0.075 M2 movement	± 26 LG movement
5	ACQ stability [μm for mins]	± 0.075 M2 movement for 1 min	± 2.6 LG movement for 1 min
6	Long term stability [μm for mins]	within 7.5 μm for 30 mins	within 2.6 mm for 30 mins
7	Mechanical dynamic performance [Hz]	> 100	100 Hz
8	Decenter [μm]	± 2 M2 movement	± 30 [mm] L1 movement
9	Tip-tilt	± 125 μrad	

Table 9.1: Refocusing mechanism operational requirements table.

9.2 Environmental requirements

In this section the environmental requirements are discussed and summarized in table 9.2 . The first requirement is the operational temperature range. The mechanism should be able to survive this temperature change. This means that the material expansion/contraction should not lead to mechanical failure.

The second requirement is the launch load. This is the large acceleration experienced by the mechanism, The stresses developed by these accelerations should be within the yield strength of the materials to avoid mechanical failure.

	Requirement	Values for M2	Values for LG
1	Operational temperature range [$^{\circ}C$]	-15 to +35	-15 to +35
2	Launch load	Static 100g in all directions	Static 100g in all directions

Table 9.2: Refocusing mechanism environmental requirement table.

9.3 Functional design

Now that the system level requirements are derived, the different elements of the mechanism will be explained. The M2 mirror that is to be moved is shown in figure 9.1.

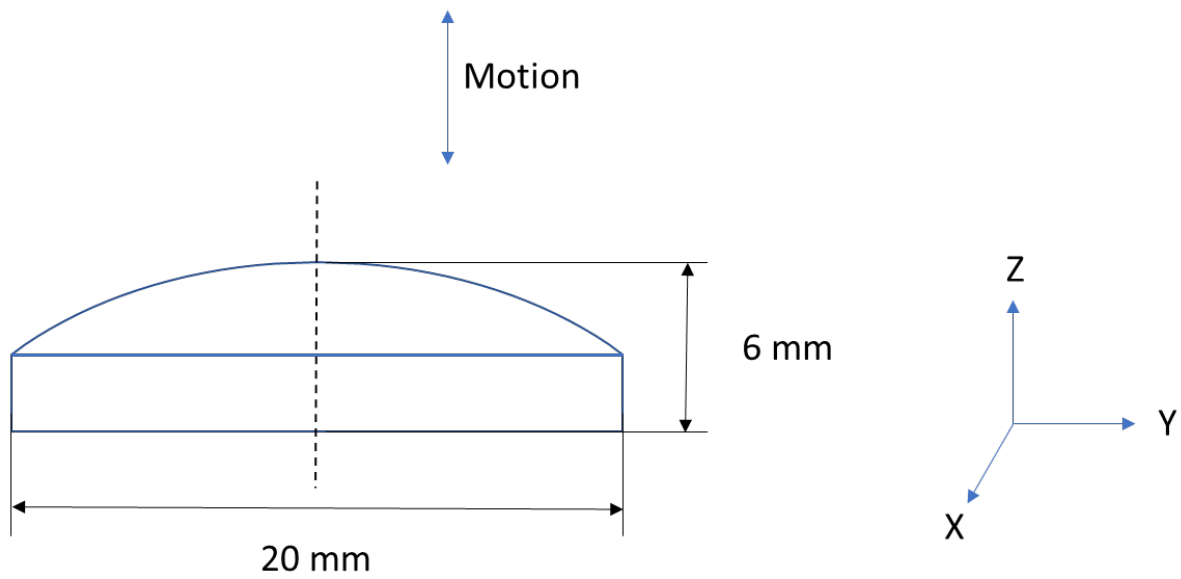


Figure 9.1: Dimensions of the M2 mirror.

The mirror is to be moved along its optical axis it needs an actuator. Further, the mirror needs to be restricted in the remaining five degrees of freedom so it needs a guidance. Also, there needs to be a coupling between the actuator and the mirror to transfer force. Finally, all these components need to be integrated to the telescope, so we need a housing. A schematic of the functional block diagram is shown in figure 9.2.

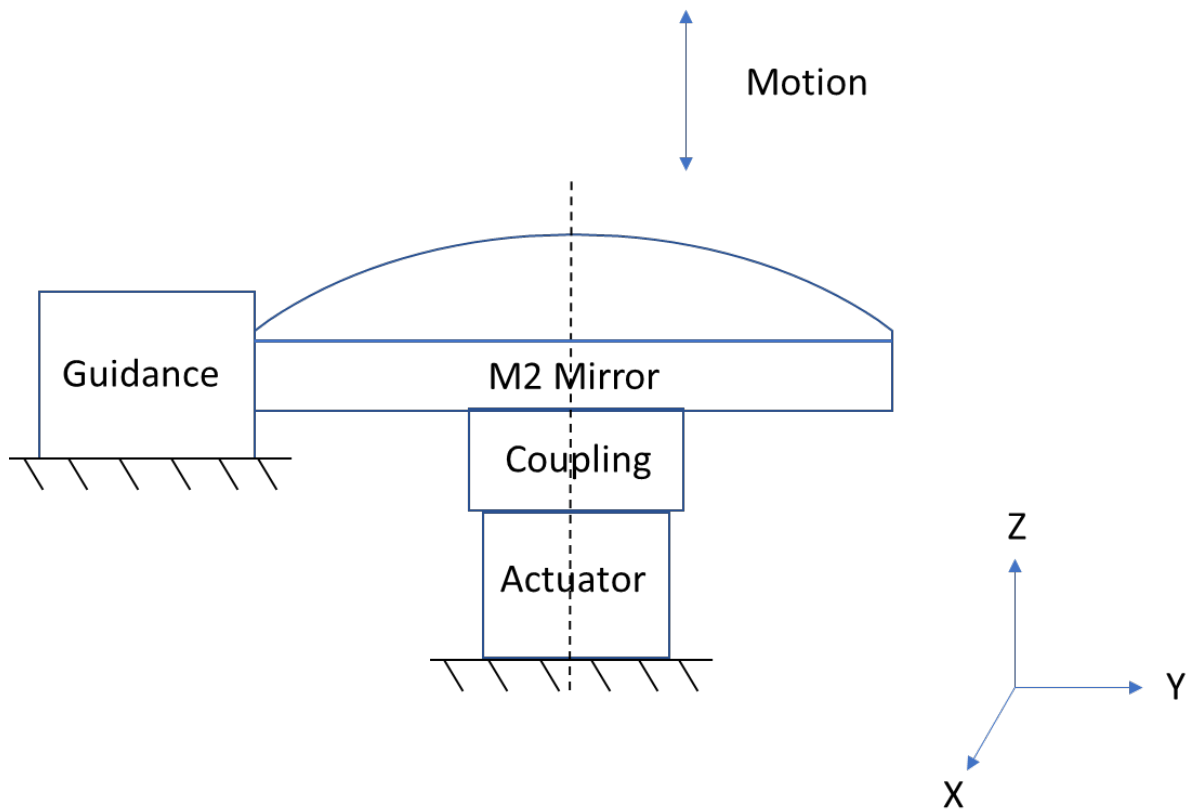


Figure 9.2: RFM functional block diagram.

9.4 Conclusion

A list of operational requirements was derived based on the analysis carried out in Part II of the thesis. A functional design was presented showing the different blocks required to design the mechanism.

Part III

Mechanism Design

Chapter 10

Actuator selection

At the end of the previous chapter a functional design of the RFM was shown. One of the blocks was the actuator. In this chapter the steps taken to select an actuator are presented. The following research questions are evaluated.

- What are the possible actuators that can satisfy the requirements?
- What is the best solution?

The chapter begins with a high level trade-off of the actuators. In this stage, the possible actuators are selected. In the next part of the chapter a more detailed comparison is carried out and finally a selection is made.

10.1 Definitions and selection criteria

In this section, the definition of terms used to compare the actuators is presented. Further, a selection criteria is given.

Static power consumption: It is the power consumed (Watts) by the actuator to hold a certain position within its range of motion. It is desirable to have low static power consumption because of two reasons. 1) To reduce the overall power consumption of the terminal 2) Some part of this power is converted to heat. In this case, the actuator acts as a heat load for the mirror. This can deform the mirror's reflecting surface and lead to surface form error.

Launch lock: It is a device used to hold the moving mass of the actuator in place during launch. A launch lock is best avoided as it adds complexity to the design.

Speed: In this context, the speed is referred to the required jitter frequency of 100Hz. The actuator which cannot meet this requirement is not suitable.

10.2 High level actuator trade-off

The three types of actuators are considered for the RFM and are summarized with their advantages and disadvantages in table 10.1. The rotary motor (can be a stepper or a DC motor) needs a screw to convert rotary motion to linear motion. The screw and nut always has some play which affects the precision. Although techniques like pretension it adds to the complexity. Additionally, it will not meet the minimum incremental motion requirement. A gearbox can be introduced to reach the minimum incremental motion but this will make the system slow. Therefore, this is not a solution. The thermal actuator is a robust actuator but slow in nature and will not meet the jitter frequency requirement. So, thermal actuators are not a possible solution. Linear actuators consists of electromagnetic and piezo-electric actuators. These kind of actuators generate linear motion and can have high speed and resolution. These are a set of possible solution and are studied in more detail in the following sections.

	Actuator	Advantages	Disadvantages	Comments
1	Linear actuators	Fast Compact	static power consumption	Possible solution
2	Rotary motor + screw	No launch lock required	Required range and resolution not possible Bulky Backlash, play, friction Complex design	Not possible
3	Thermal actuator	No launch lock required No moving parts/joints means inherently stable	Slow Finite static power consumption	Not possible because it's slow

Table 10.1: Actuator high level trade-off.

10.3 Linear actuators

In this section the three possible actuators are studied in detail. These are divided into three subsections. The individual study consists of the working principle, advantages, disadvantages. There are many sub-variants of the three actuation principles that are considered. Therefore, first an argument is made for the most suitable sub-variant for this application and then the pros and cons are considered. In the end, all the relevant properties are summarized in a table.

Piezoelectric actuator

The first actuator considered is a piezoelectric actuator. There are a variety of actuators available in different shapes and sizes. One degree of freedom piezoelectric actuators are generally divided into two categories based on the direction of the piezoelectric coefficient used for actuation. Piezoelectric coefficient d_{33} refers to the expansion of the material along the direction of applied voltage. Whereas, piezoelectric coefficient d_{31} refers to the expansion of the material perpendicular to the direction of the applied voltage. In general, the piezoelectric coefficient d_{33} is larger than d_{31} and is suitable for a large range. To further increase the range of the actuator, the piezoelectric elements are stacked together. The displacement of a piezoelectric element is given by equation 10.1.

$$\Delta l = nd_{33}V \quad (10.1)$$

where, n is the number of piezoelectric elements, d_{33} is the piezoelectric coefficient and V is the applied voltage. The displacement can be calculated for a typical ceramic PZT actuator with the above equation with the following numbers. Assuming 20 stacks with a d_{33} of 500 pm/V applied with a 1000V gives the maximum displacement of $10\mu m$ which is less than the required $60\mu m$.

To further increase the range, mechanical amplification is applied similar to the one in section 4.6. The amplified piezoelectric actuator is commercially available which can meet the required range [27].

Although the range requirement is met there are a few disadvantages for the piezoelectric actuator. The actuator require a high voltage supply. This needs dedicated drive electronics which will add to the power consumption. Also the size of the electronics is large. The actuator exhibits non-linear behaviour in the form of hysteresis and creep. Although these can be corrected for by closing the loop, the mechanism operates in open loop during the ACQ stage and any instabilities and drifts will cause failure. A method to correct hysteresis is to model the behaviour and calibrate but this can be complex and therefore not desirable. Ageing is also an issue as the mechanism is expected to operate for 15 years.

Voice coil actuator

The voice coil actuator is an electromagnetic actuator that works on Lorentz force. First the range of the actuator is considered. A commercially available voice coil actuator typically has a range of a few millimeters [33]. This is an overkill for the requirement of the RFM. Another key property to consider is the power dissipation as a function of the mover position. It depends on the motor constant of the actuator. Motor constant is the amount of force generated per square root of power. A large motor constant indicates a more power efficient actuator.

The voice coil actuator is a possible solution.

Hybrid actuator

A hybrid reluctance actuator is an electromagnetic actuator with a permanent magnet in combination with a reluctance actuator. The actuator considered here is the one that is developed by TNO [34]. The range of motion of such an actuator is typically $100\mu\text{m}$. The actuator has a large motor constant which makes it more efficient than a voice coil actuator.

Actuator selection

After considering the possible actuators it is decided to choose the hybrid actuator because it ranks in between the piezoelectric and voice coil in terms of range. It has a linear force current relation, and is power efficient. Also, as it is developed in house it can be tuned to meet the specific requirements of the RFM.

Actuator	Range (order of magnitude)	Resolution	Static power consumption	Force-current linearity	Mechanical stiffness	Speed	Actuator specific
Units	(μm)	(nm)	(-)	(-)			(-)
Piezoelectric stack	~ 10	~ 1	+++	No	+++		High voltage electronics, Weak in tensile load, shock load
Voice coil	~ 1000	~ 100	+	Yes	++		
Hybrid reluctance	~ 100	~ 10	++	Yes	++		
Requirement	60 micron	9 nm	As low as possible.	Yes	-	100 Hz	-

Table 10.2: Actuator trade-off table

10.4 Hybrid actuator

As the hybrid actuator is our chosen concept, this section will shortly explain the working principle. The relevant equations are given in subsection 11.5.

The schematic of the hybrid actuator is shown in figure 10.1. The force is generated by the the imbalance in magnetic flux in the two airgaps. The magnetic flux in the airgaps is a combination of the coil generated flux and the permanent magnet flux. The magnitude of direction of electric current in the coils determines the direction of motion.

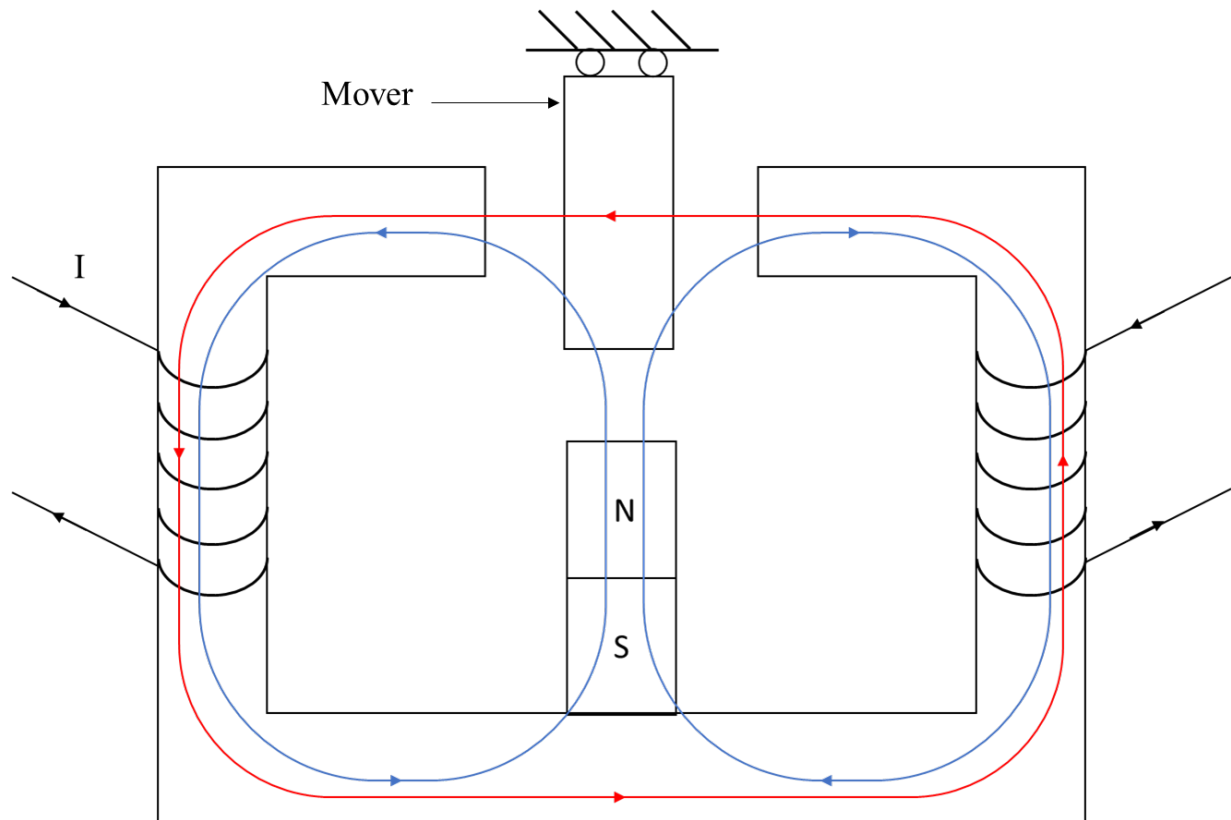


Figure 10.1: Schematic of the hybrid actuator.

10.5 Conclusion

A high level actuator trade-off is carried out which results in three possible actuators namely piezo-electric actuator, voice coil actuator and a hybrid actuator. The hybrid actuator is better than voice coil actuator in terms of power efficiency. The piezo-electric actuator suffers from hysteresis, creep and ageing. Therefore, hybrid actuator is the best solution for the refocusing mechanism.

Chapter 11

Mechanism design

In this chapter the guidance for the mechanism is designed. The chapter starts with the different concepts considered for the guidance and the reasoning for selecting the final concept. After the concept selection, the final concept is dimensioned based on the requirements imposed on the mechanism. At the end of the chapter a summary table is provided to show that the designed guidance satisfies the mechanism requirements.

In this chapter the following research questions are evaluated.

- What are the different possible concepts for the guidance?
- What is the best choice for the RFM?
- What is the size of the guidance?

11.1 Guidance concepts

The function of the guidance is to allow translation of the moving body(in this case the M2 mirror) and constraint it's remaining five degrees of freedom. Flexure mechanisms are free of friction which makes them suitable for precise positioning. Additionally, they do not require lubrication which makes them suitable for space application where cleanliness is a requisite. Freedom and constraint topology (FACT) is a design library used to design parallel flexure mechanisms. The complete library is shown in Appendix A. For one degree of freedom translation, the constraint topology dictates that the flexures must lie in two parallel planes perpendicular to the direction of motion.

A variety of straight guidance concepts are available in the literature. These concepts are summarized in appendix A. Concepts 1, 2 and 5 are the most promising. The concepts compared here are considered to be of same size to make a fair comparison.

Concept 5 is a compound leaf flexure mechanism with four leaf flexures. Two of these leaf flexures connect the ground and an intermediate body. An inverted version of this is attached to the intermediate body to cancel out the shortening effect of the flexures. This results in a straight line motion. A drawback of this concept is that it is under-constrained. As a result, the intermediate body is free to translate. This can be a problem during launch as the intermediate body can have excessive excursion which may lead to failure. As the concept is not rotationally symmetric, the mounting of the mirror will shift the center of mass of the assembly away from the optical axis of the mirror. This will introduce moments which can lead to error motion.

The mirror is irradiated with the Tx laser beam. A small fraction of this laser power is absorbed by the M2 mirror. This heat has to be dissipated to the telescope. The only heat path between the mirror and the telescope is through the guidance. This has to be as short as possible to keep gradients low. Otherwise, the mirror position will drift and degrade the optical performance. For concept 5, the heat path from the mirror to the telescope is twice the length of a flexure which is quite long compared to other concepts. This will introduce large thermal gradients. This can be a problem as the optical axis can shift laterally.

Concept 2 is a construction of five folded leaf flexures connecting the moving body to the ground. The fold of the leaf flexures constrains one degree of freedom and make the design exactly constrained. A feature of this concept is the near rotational symmetry. A drawback of this concept is that the folds need to sharp to avoid error motion[35]

The heat path between the mirror and the telescope is equal to the length of the a folded leaf flexure. However, there are five such heat paths so the heat can be dissipated better than concept 5.

Concept 1 has five struts which connect the moving body to the ground. Each strut constrains one degree of freedom which makes the design exactly constrained. Furthermore, The design is nearly rotationally symmetric which gives a nearly uniform radial stiffness. On the other hand, a drawback of this concept is the shortening effect of the flexures. This means that the movement of the body along it's DoF will cause a rotation about it's axis. However, this is not a problem because the mirror is rotationally symmetric.

The heat path between the mirror and the telescope is the shortest for concept 1 compared to other concepts. Moreover, there are five struts which represent five heat paths. However, the strut cross-section area is the least which still results in a large thermal gradient.

11.2 Concept choice

The comparison of the three concepts is summarized in table 11.1. From the comparison it is clear that concept 1 and 2 are superior to concept 5. Further, concept 1 and 2 are very close and with two differences. First there is shortening effect in concept 1 but this is not a problem as discussed in the previous section. The second difference is the length of heat path. Although concept 1 has shorter heat path

	Concept 1	Concept 2	Concept 5
Exactly constrained design	Yes	Yes	No
Rotational symmetry	Yes	Yes	No
Shortening effect	Yes	No	No
Thermal center	Conincides with the optical axis	Conincides with the optical axis	Does not conincide with the optical axis
Heat path	+	-	-

Table 11.1: Concept comparison summary.

An additional strut is added in the design to add symmetry which results in uniform radial stiffness. Although, this makes the design over-constrained in the rotation about the axis of the moving body, it is not a problem because the mirror is rotationally symmetric. The schematic diagram of the tangential flexure concept is shown in figure 11.1. Mounting individual rods as struts increases the number of interfaces between the moving body and the fixed world. This is circumvented by making two identical monolithic circular membranes with three flexure cut-outs. One such membrane is shown in figure 11.2.

Each strut will be called a flexure and a set of three flexures lying in one plane will be called a membrane hereafter.

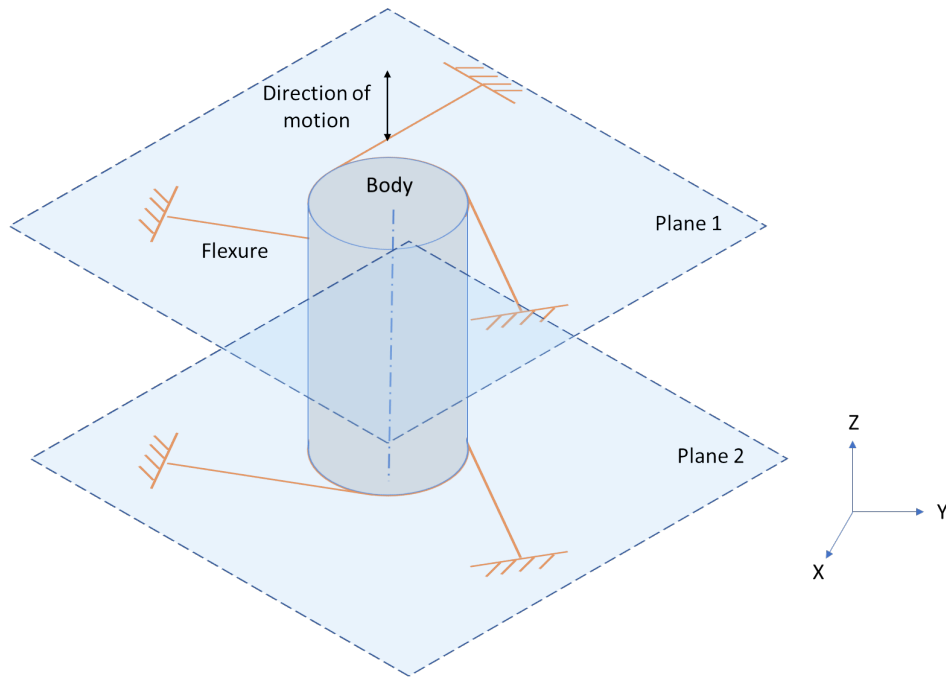


Figure 11.1: Tangential flexure concept. Note that the co-ordinate system for the guidance is in uppercase.

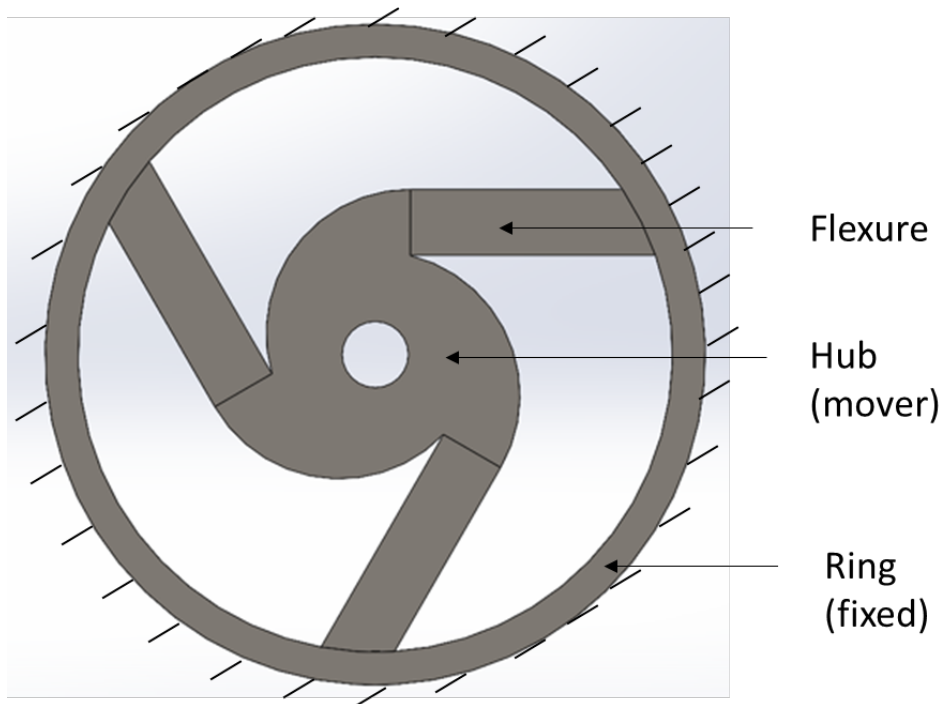


Figure 11.2: A membrane of the tangential flexure concept.

11.3 Guidance design

In this section, the dimensions of the guidance flexures are determined. First the requirement is established based on the system level requirement and then the dimensions are realised based on the design equations.

11.3.1 Requirement

Axial stiffness

The first requirement for the guidance is to have an appropriate axial stiffness. The combined stiffness of the actuator and the guidance should achieve the required range of ± 30 . This is mathematically represented by equation 11.1.

$$k_A = \frac{F}{Z} - k_G \quad (11.1)$$

where, k_A is the stiffness of the actuator, F is the peak force generated by the actuator, Z is the range of the mechanism and k_G is the stiffness of the guidance in the axial direction. The stiffness of the actuator is tunable within the range $1e5$ N/m and $1e6$ N/m. The plot of guidance stiffness as a function of actuator stiffness is shown in figure 11.3.

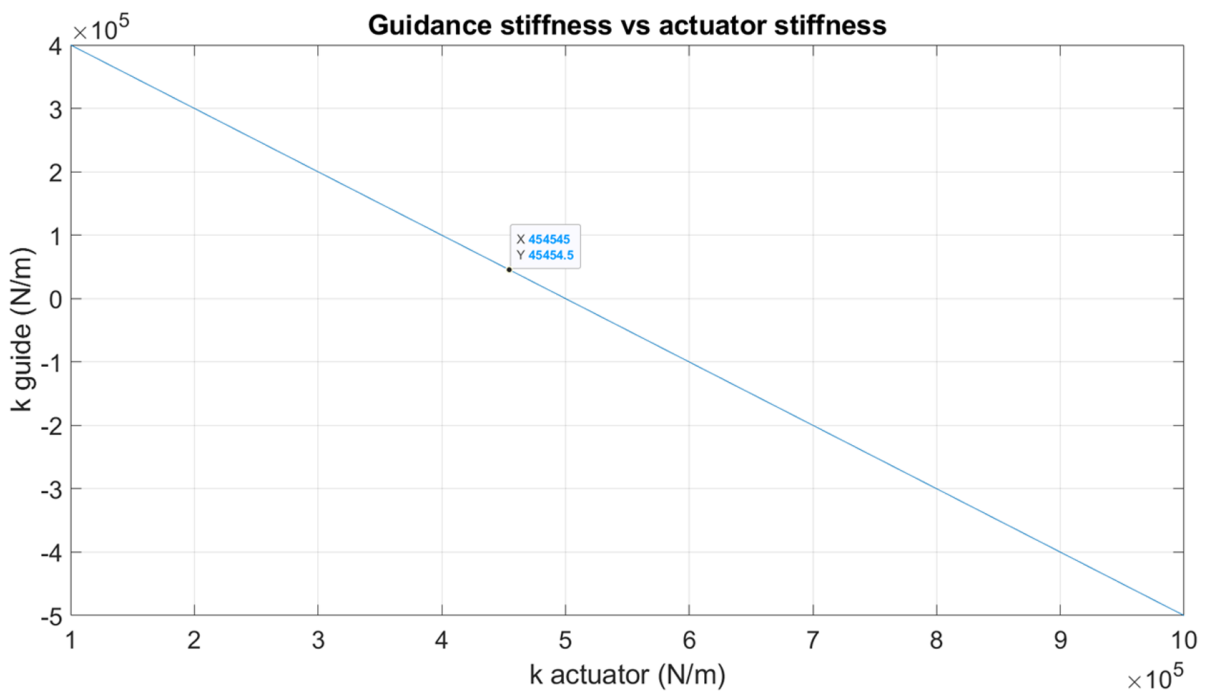


Figure 11.3: Guidance stiffness as a function of actuator stiffness.

The feasible region for the guidance stiffness lies above $y = 0$ and below the plot line. A range of solution is possible but it is better to have low stiffness to reduce the power consumption. Therefore, an actuator stiffness of $5e4$ N/m is chosen. This corresponds to a guidance stiffness of $4.5e5$ N/m. So the axial stiffness of the guidance should be lower than $4.5e4$ N/m to meet the range requirement.

Radial stiffness

The second requirement is the radial stiffness of the guidance. It is driven by the resonance frequency of the guidance-mirror combination. It is assumed that the mechanism will survive launch if this resonance frequency lies above the maximum frequency of random vibrations experienced during launch. The random vibration spectrum has a maximum frequency of 2 kHz according to a NASA practice [36].

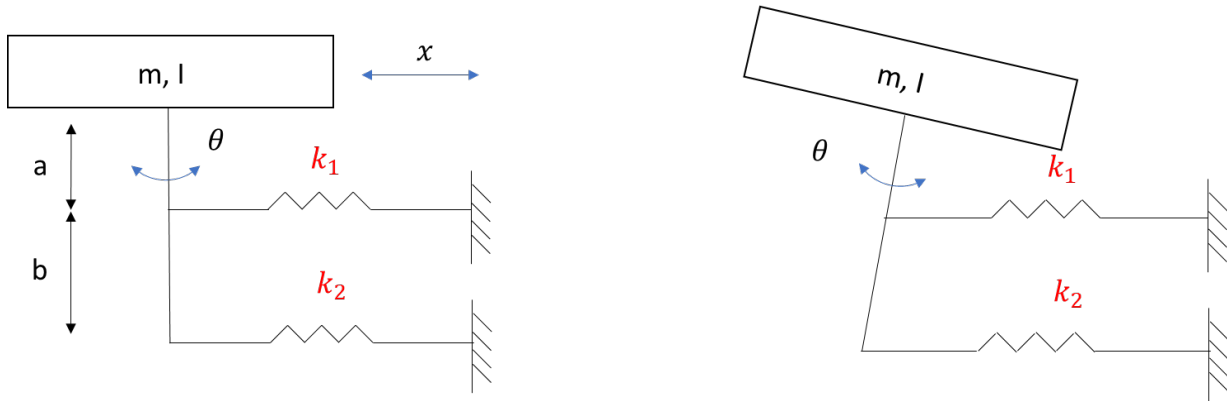


Figure 11.4: A schematic of the mirror-guidance combination.

The guidance-mirror combination is modelled as shown in figure 11.4. This model can have two motions. A translation in x direction and an in plane rotation. The resonance frequency of this model is a function of the inertia of the mirror and the stiffness of the guidance. The resonance frequency for the translation is given by equation 11.2.

$$f_1 = \frac{1}{2\pi} \sqrt{\frac{k_{radial}}{m}} \quad (11.2)$$

where, k_{radial} is the radial stiffness of the guidance. $k_{radial} = k_1 + k_2$. m is the mass of the mirror.

The resonance frequency for the rotation is give by equation 11.3.

$$f_2 = \frac{1}{2\pi} \sqrt{\frac{k_{radial} (a^2 + (a+b)^2)}{2 \left(\frac{mr^2}{4} + \frac{ml^2}{12} \right)}} \quad (11.3)$$

where, a and b are distances as shown in figure 11.4, l is the thickness of the mirror, m is the mass of the mirror and r is the radius of the mirror. Substituting the values for the parameters and setting f_1 as 2kHz results in a radial stiffness of $6.08e5$ N/m.

A plot of f_2 as function of disk spacing b is shown in figure 11.5. It is clear that the disk spacing should be greater than 4 mm for f_2 to be greater than 2kHz.

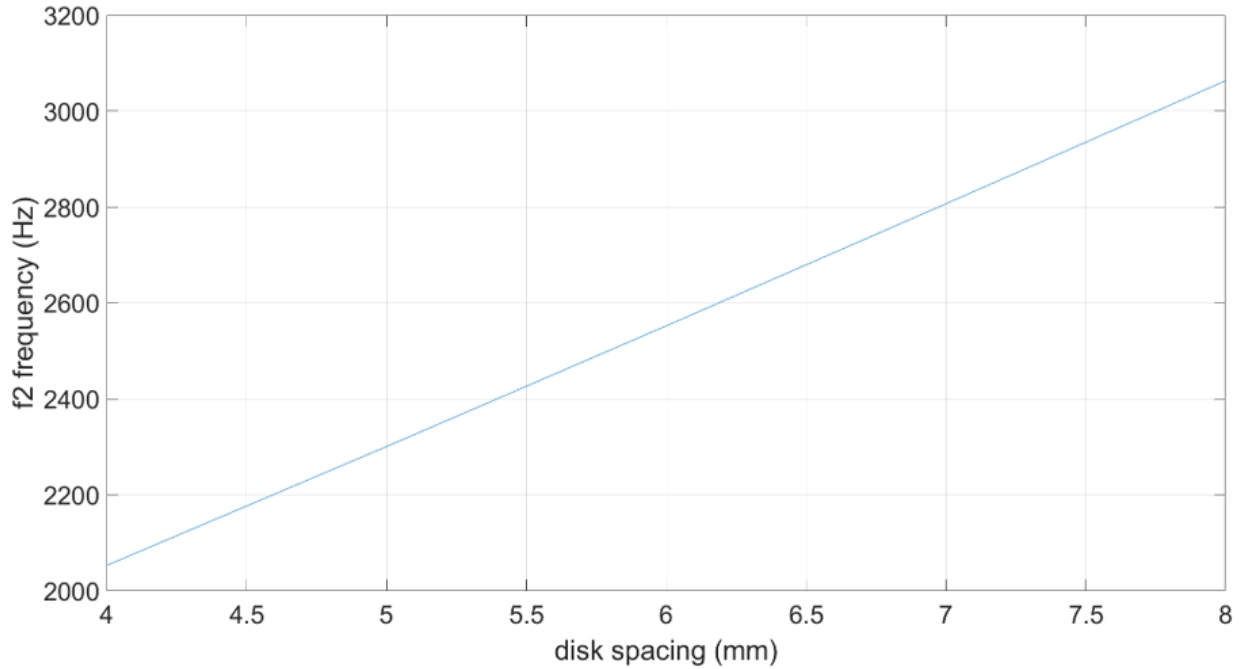


Figure 11.5: Resonance frequency f_2 as a function of disk spacing.

In conclusion, $k_{axial} < 4.5e5 N/m$ and $k_{radial} > 6.08e5$.

11.3.2 Material selection

The flexures are required to operate at a frequency of 100 Hz. The material should sustain the stress introduced by this cyclic loading in order to be mechanically safe. This means that fatigue strength is the driving requirement for the flexure material. Stainless steel ASTM 301 is a material which has high fatigue strength and is easily available in strip form. The material properties[37] are summarized in table 11.2.

Material	Density	Youngs modulus	Poissons ratio	CTE	Yield strength	Fatigue strength	Thermal conductivity	Specific heat capacity
	(kg/m^3)	(GPa)	(-)	(m/K)	(MPa)	(MPa)	(W/mK)	(J/kgK)
Stainless steel 301	7900	185	0.33	15.5	1050	555	15	500

Table 11.2: Flexure material properties.

11.3.3 Axial stiffness

Each flexure can be modelled as a cantilever beam fixed at one end and a point load acting at the free end as shown in figure 11.6. Note that the shape of the deformed beam is S-shape due to the parallel configuration of the flexures. The deflection equation for this configuration of beam is given by equation 11.4a. The area moment of inertia for a beam with rectangular cross-section is given by equation 11.4b. Substituting equation 11.4b in equation 11.4a and rearranging for stiffness gives equation 11.4c.

$$\delta = \frac{Wl^3}{12EI} \quad (11.4a)$$

$$I = \frac{bd^3}{12} \quad (11.4b)$$

$$k = \frac{W}{\delta} = \frac{Ebd^3}{l^3} \quad (11.4c)$$

Here, W is the point load, δ is the tip deflection, k is the beam stiffness, l is the beam length, b is the width of the beam and d is the thickness of the beam, I is the area moment of inertia and E is the Young's modulus of the beam material.

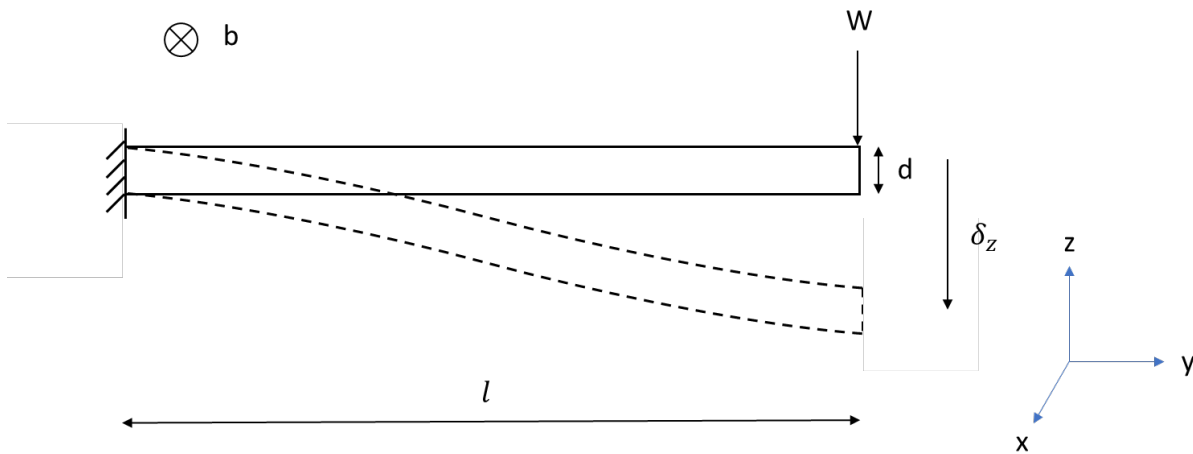


Figure 11.6: The flexure is modelled as a cantilever beam under a point load at it's free end. The original shape is shown in solid and the shape of the deformed beam is shown in dashed. Note that the co-ordinate system for a flexure is in lowercase.

Further, The axial stiffness of the six flexures are in a parallel configuration. Therefore, the total axial stiffness of the guidance is six times the individual stiffness of each flexure. The total axial stiffness of the guidance is given by equation 11.5

$$k_{axial} = \frac{6 \cdot Ebd^3}{l^3} \quad (11.5)$$

11.3.4 Radial stiffness

The radial stiffness of a membrane is modelled as a combination of in plane bending and expansion/contraction of the flexure as shown in figure 11.7. The in plane bending stiffness and axial stiffness is represented by springs with blue and orange colour respectively. The radial stiffness of a membrane is given by equation 11.6.

$$k_{radial} = \frac{n}{2}k_{axial} + \frac{n}{2}k_{bending} \quad (11.6)$$

where, n is the number of flexures in a membrane. In this case it is three.

For a flexure, the axial stiffness is given by equation 11.7.

$$k_{axial} = \frac{EA}{l} = \frac{Ebd}{l} \quad (11.7)$$

The in plane bending stiffness is modelled similar to the bending stiffness in sub-subsection 11.3.3.

$$\delta = \frac{Wl^3}{12EI} \quad (11.8a)$$

$$I = \frac{db^3}{12} \quad (11.8b)$$

$$k_{bending} = \frac{Edb^3}{l^3} \quad (11.8c)$$

$$(11.8d)$$

Finally, substituting equations 11.8d and 11.7 in equation 11.6 results in equation 11.9.

$$k_{radial} = \frac{3 Ebd}{2 l} + \frac{3 Edb^3}{2 l^3} \quad (11.9)$$

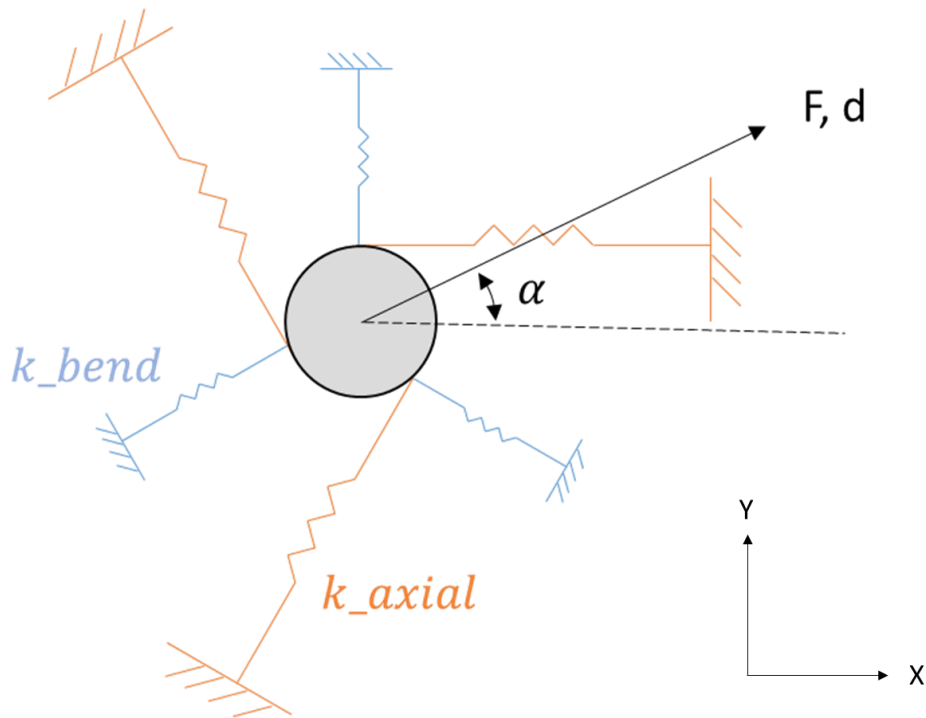


Figure 11.7: A schematic of the radial stiffness of one of the membranes. Here, F and d is the direction of external force and displacement respectively. Angle α is the angle between the direction of displacement and the x axis.

11.3.5 Resolution

The resolution of the mechanism depends on the amplifier resolution given by equation 11.10. Assuming a 12 bit amplifier the resolution of the mechanism is 15 nm.

$$resolution = \frac{range}{2^{bits}}; resolution = \frac{60}{2^{12}} \approx 15nm \quad (11.10)$$

11.3.6 Resonance frequency

The resonance frequency of the mechanism is the combination of the actuator and guidance axial stiffness and the total moving mass. This is given by equation 11.11.

$$f = \sqrt{\frac{k_{actuator} + k_{guide}}{m_{mirror} + m_{guide} + m_{actuator}}} \quad (11.11)$$

This results in a resonance frequency of 1145 Hz.

11.3.7 Stress criteria

The bending stress in a flexure generated due to axial motion is given by equation 11.12.

$$\sigma_b = \frac{3Ed\delta}{l^2} \quad (11.12)$$

11.3.8 Flexure dimensions

The length of the flexures is driven by the obscuration ratio diameter. This results in a length of 10 mm. The thickness of the flexures is chosen based on the standard sheet thickness commercially available. The flexure width is a free parameter and one possible combination is $b = 2\text{mm}$ and $d = 0.2\text{mm}$. The guidance is visualised in figure 11.8.

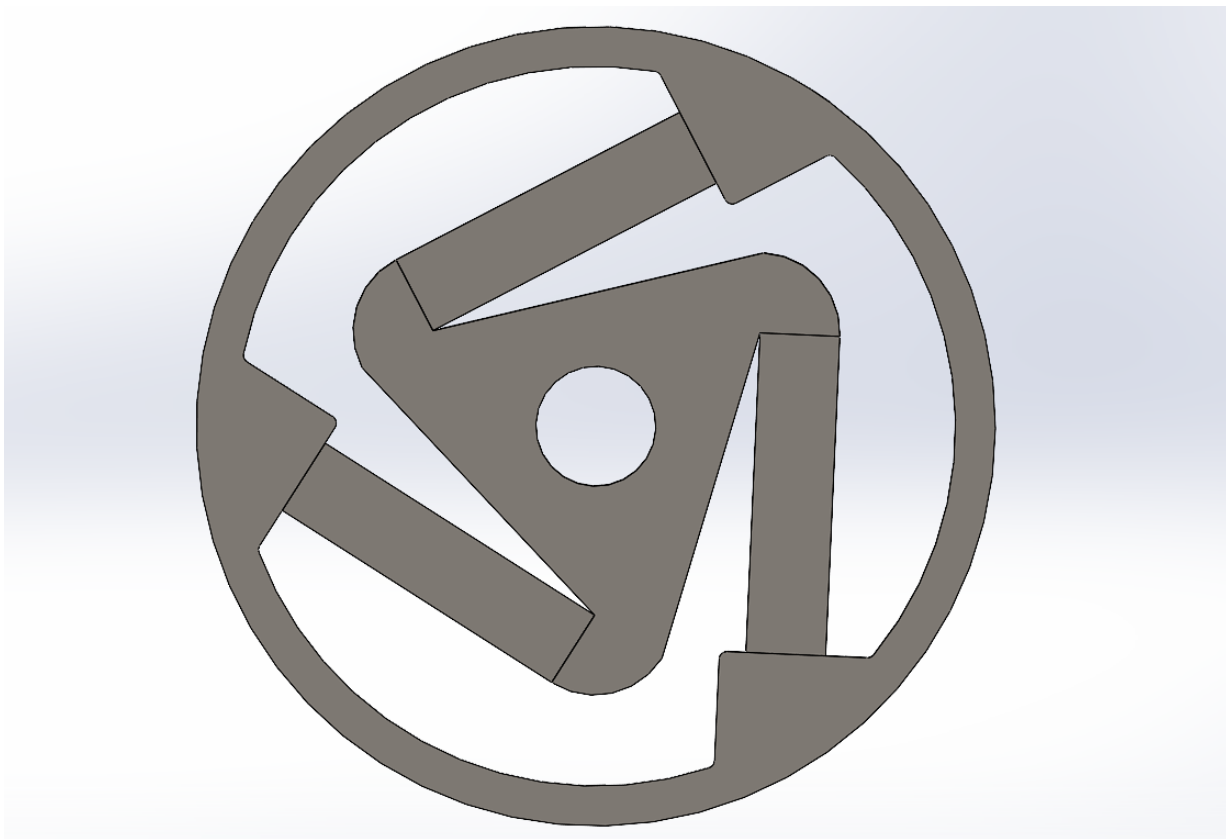


Figure 11.8: Flexure design

11.4 Strut

The strut forms the connection between the actuator and the mirror. The strut has two functions: 1) It should be highly stiff in the longitudinal direction to effectively transfer the force from the actuator mover to the mirror. 2) It should be compliant in the radial directions and allow rotations to compensate for misalignments. The strut is visualized in figure 11.9. The rod portion of the strut provides high longitudinal stiffness and the two notches on either side of the rod provide rotational and radial compliance.

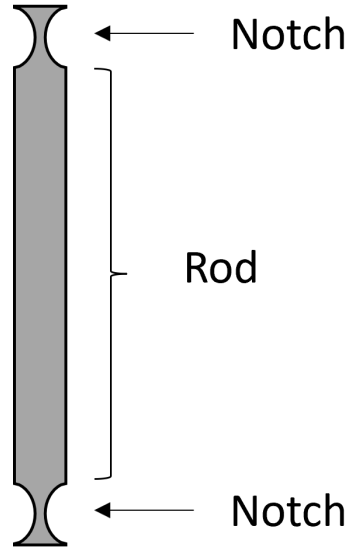


Figure 11.9: A schematic of the strut.

The strut consists of two parts, the rod and two notches. The dimensions of the strut are based on the axial stiffness and the compliance of the notches. The rotational and axial stiffness of the notch is given by equation 11.13 and 11.14 [38] respectively.

$$k_{\theta_y} = k_{\theta_z} = \frac{Et^{\frac{7}{2}}}{20R^{0.5}} \quad (11.13)$$

$$k_x = \frac{Et^{\frac{3}{2}}}{2R^{0.5}} \quad (11.14)$$

where, E is the young's modulus, t is the thickness of the notch and R is the radius of curvature of the notch.

The axial stiffness of the rod is given by equation 11.15.

$$k_{rod} = \frac{EA}{L} = \frac{E\left(\frac{\pi}{4}d^2\right)}{L} \quad (11.15)$$

where, E is the Young's modulus, A is the cross-section area of the rod, L is the length of the rod and d is the diameter of the rod.

The axial stiffness of the strut is a series combination of the rod and two notches and is given by equation 11.16.

$$(k_{strut})^{-1} = (k_{shaft})^{-1} + (0.5k_{notch})^{-1} \quad (11.16)$$

It is assumed that for the strut to be considered stiff, it's axial stiffness should be 5 times higher than the guidance axial stiffness. Similarly, the rotational stiffness of the notch is assumed to be 10 times lower than the rotational stiffness of the guidance.

11.4.1 Strut dimensions

The dimension of the notch is $t = 0.6$ mm and $R = 2$ mm based on the rotational stiffness requirement. The axial stiffness criteria for the strut results a rod diameter of 1 mm. The length of the strut is based on the distance between the mirror and the actuator mover which is 19 mm. The strut is shown in figure 11.10.

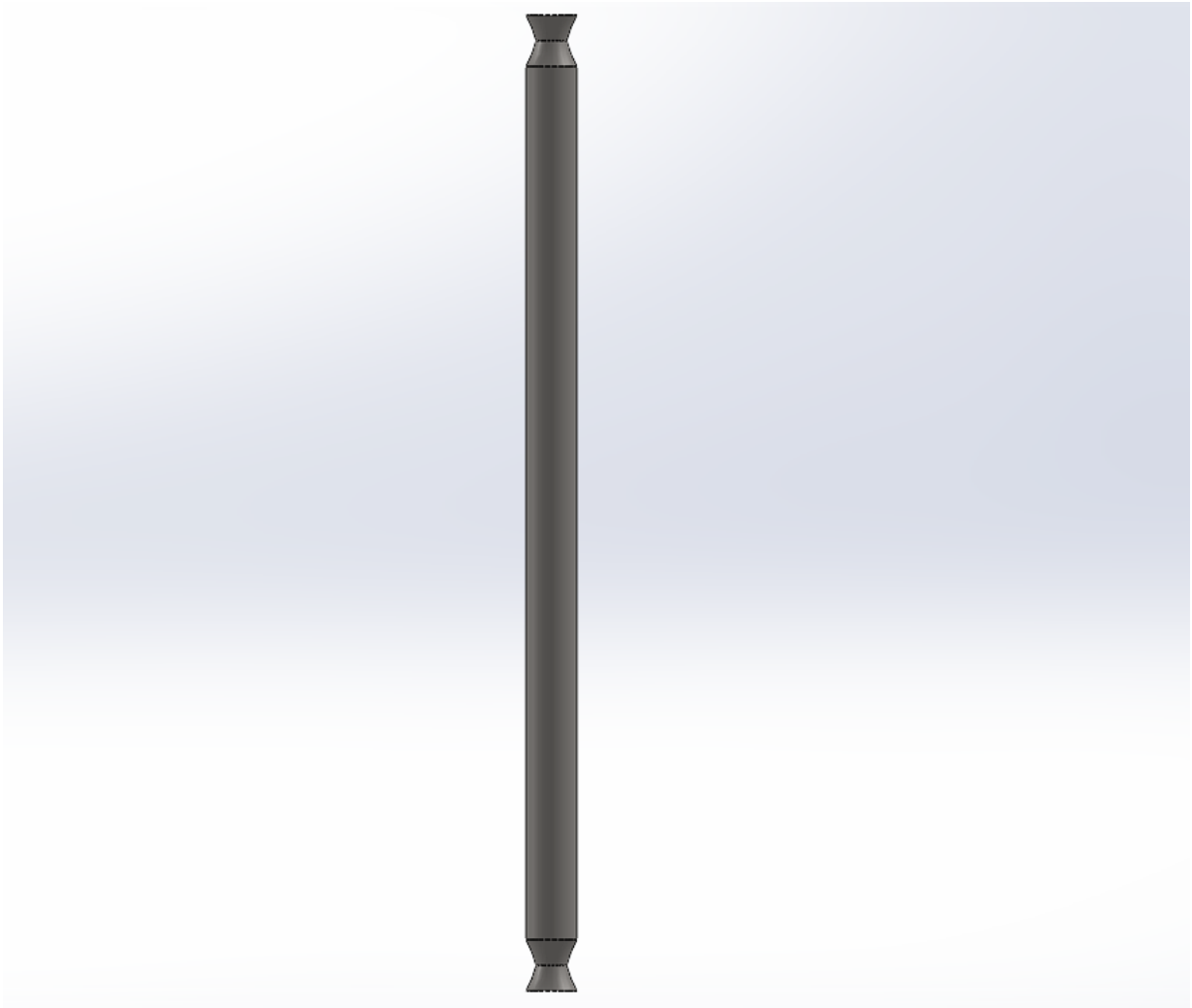


Figure 11.10: Strut.

11.5 Power consumption

Now that we have the stiffness of the actuator and the guidance, we can calculate the power consumption for the mechanism. The static power consumption for a hybrid actuator is given by equation 11.17.

$$P = F/K_a \quad (11.17)$$

where, P is the static power consumption, F is the force required to hold a certain position and K_a is the actuator constant. The force required to hold a certain position is given by equation 11.18.

$$F = kx \quad (11.18)$$

where, k is the stiffness and x is the position. The stiffness of the actuator is a combination of the stiffness of the actuator and the guidance.

The plot of power consumption as a function of position is shown in figure 11.11. The power consumption is zero at neutral position and increases quadratically away from the neutral position. The maximum static power consumption at a position of 30 μm away from the neutral position is 55 mW.

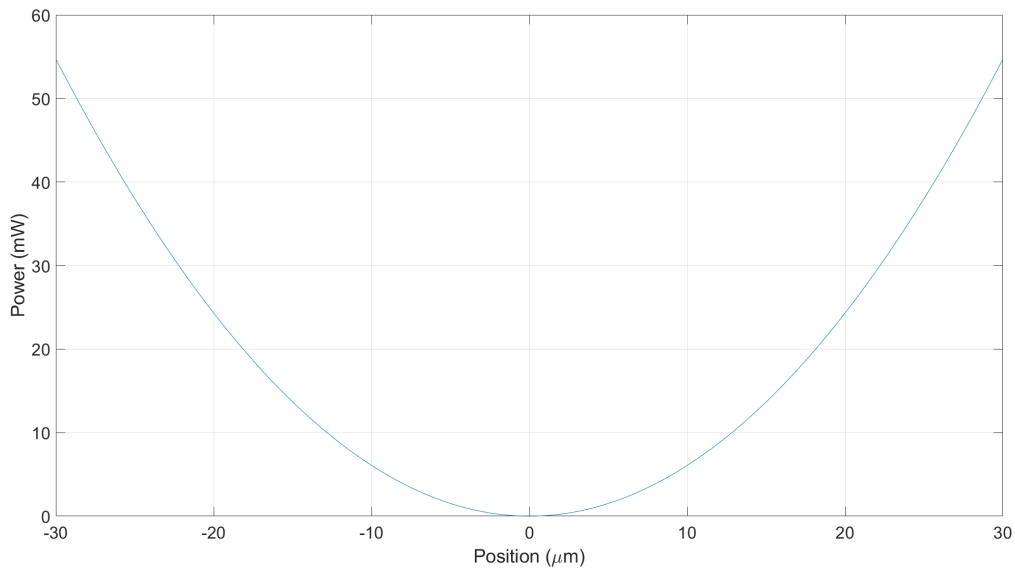


Figure 11.11: Static power consumption for a hybrid actuator.

11.6 Design overview

The overview of all the subsystem requirements and the designed values is given in table 11.3. It is clear that all the sub-system requirements are met.

Subsystem	Functions	Requirements	Values
Guidance	Constrain the mirror to axial motion within a certain range	$k_{\text{axial}} < 5e4 \text{ N/m}$ $k_{\text{radial}} > 6.08e5 \text{ N/m}$ range: ± 30 micron diameter < 30 mm	$k_{\text{axial}} = 1.78e4 \text{ N/m}$ $k_{\text{radial}} = 2.31e7 \text{ N/m}$
Actuator	Provide force within a certain range	range = ± 30 micron	$F = \pm 15 \text{ N}$ $k_A = 4.5e5 \text{ N/m}$
Strut	Transfer the force from the actuator to the mirror Stiff in axial direction Compliant in tip-tilt, decenter	$k_{\text{strut}_z} = 5 * k_{\text{guidance}_z}$ $= 5 * 5e4 = 2.5e5 \text{ N/m}$ $k_{\text{tilt}} = (1/10) * k_{\text{guidance}_\text{tilt}}$ Survive launch	$k_{\text{shaft}} = 100 * k_G$ $= 5e6 \text{ N/m}$ $\Rightarrow k_{\text{notch}} = 10 * k_G$ $= 5.25e5 \text{ N/m}$
Housing	Sustain actuator reaction force	Survive launch	-

Table 11.3: Subsystem design overview.

11.7 Final design

The final design is shown in figure 11.12. It shows two bolting flanges (the third flange is not visible in the figure) which will be bolted to the telescope.

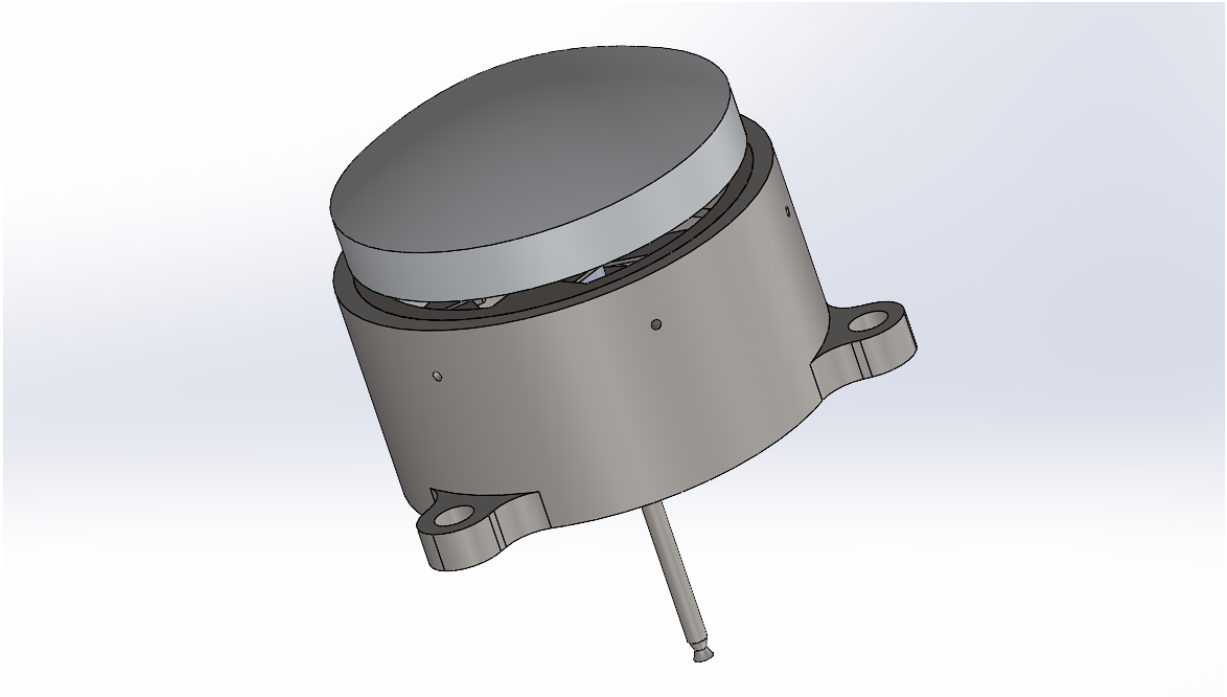


Figure 11.12: Isometric view of the final design.

Figure 11.13 shows the exploded view of the RFM. From left to right we have the M2 mirror, top membrane, bush, outer ring, bottom membrane, housing and the strut.

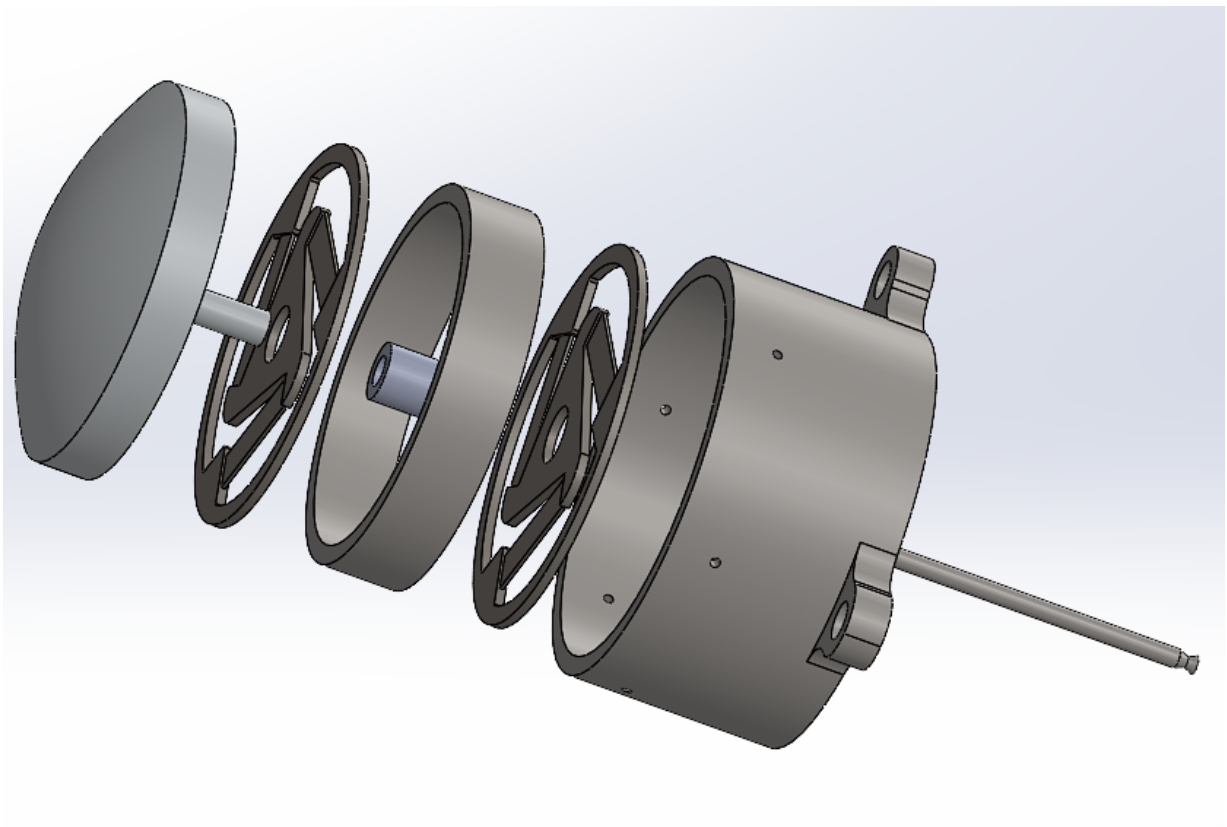


Figure 11.13: Exploded view of the final design.

11.8 Manufacturing

In this section the manufacturing process and interface joints of the mechanism are discussed.

First the manufacturing of membranes is considered. The membrane is shown in figure 11.14.

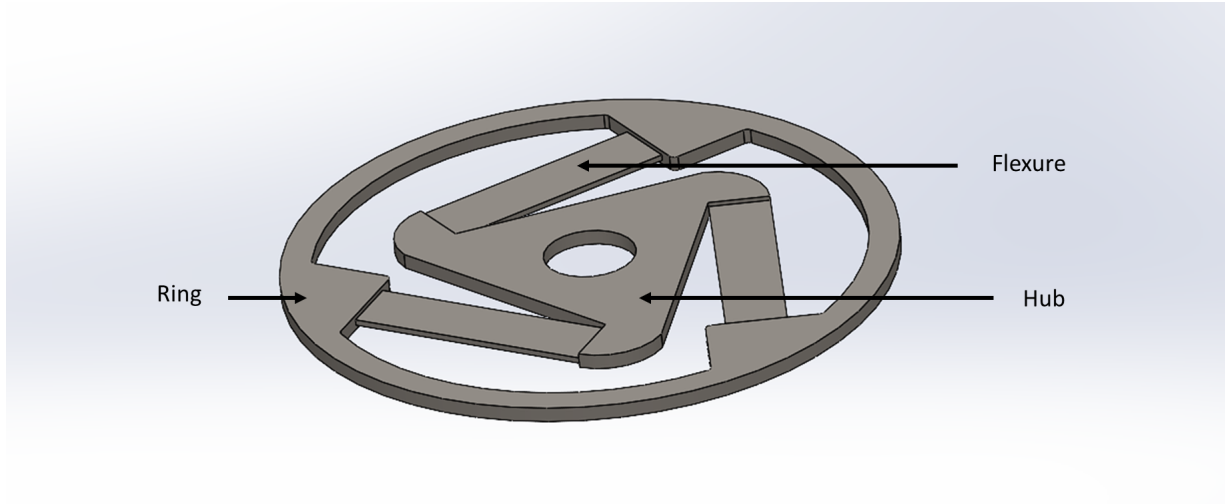


Figure 11.14: Isometric view of membrane.

The entire membrane can be cut from a steel strip with wire electric discharge machining (EDM). Note that the thickness of the flexures is lower than the thickness of the hub and the ring. This can be achieved by photochemical or chemical etching. In this way the membrane can be made monolithic.

Further, the mirror stem is press fitted in the bush and glue is inserted in the cavity between the mirror stem and the bush. The ring of the membranes is laser welded to a ring. This ring is glued to the housing. The strut is bonded on both sides; to the mirror stem on one side and the actuator mover on the other side.

11.9 Conclusion

The RFM design has four parts: mirror guidance, strut, housing. First, multiple guidance concepts are reviewed and the best one is selected. The guidance is then dimensioned based on radial and axial stiffness requirement.

Chapter 12

Thermal and mechanical analysis

In this chapter a numerical verification of the design is carried out in a FEM software. Before the verification step, some checks are carried out to gain confidence in the model. The analysis consists of two aspects namely structural and thermal. The following research questions are evaluated.

- Does the model accurately represent the designed mechanism?
- Can the mechanism survive launch?
- Does the M2 mirror surface remain within the allowable WFE spec when exposed to thermal loads?

The chapter starts with the description of the model geometry, material properties and loadcases. Further, the chapter is divided into three sections namely model check, mechanical analysis and thermal analysis. Every section has multiple load cases. Each load case follows the following structure. Description of the loadcase, boundary conditions, result and a sub-conclusion. At the end of the chapter all the loadcases and their corresponding results are summarized in a table. A conclusion is formed based on these results.

12.1 Material properties

The material properties used in this analysis are shown in table 12.1.

Material	Density	Youngs modulus	Poissons ratio	CTE	Yield strength	Fatigue strength	Thermal conductivity	Specific heat capacity	Part
	(kg/m ³)	(GPa)	(-)	(m/K)	(MPa)	(MPa)	(W/mK)	(J/kgK)	
Stainless steel 301	7900	185	0.33	15.5	1050	555	15	500	flexures
Stainless steel 304	8000	200	0.33	16.5	200	-	14	485	housing, strut
Aluminium RSA 6061	2700	70	0.33	23	295	-	160	900	mirror
EC2216	1366	2.6	0.34	102	-	-	0.42	1000	adhesive spots

Table 12.1: Material properties

12.2 Model verification

In this section the axial stiffness of the COMSOL model is checked with the designed value to gain confidence in the model. This is done by applying force in increments and capturing the corresponding displacement. This

data is used to plot the force-displacement behaviour of the mechanism. Axial stiffness is calculated from this plot and checked with the design.

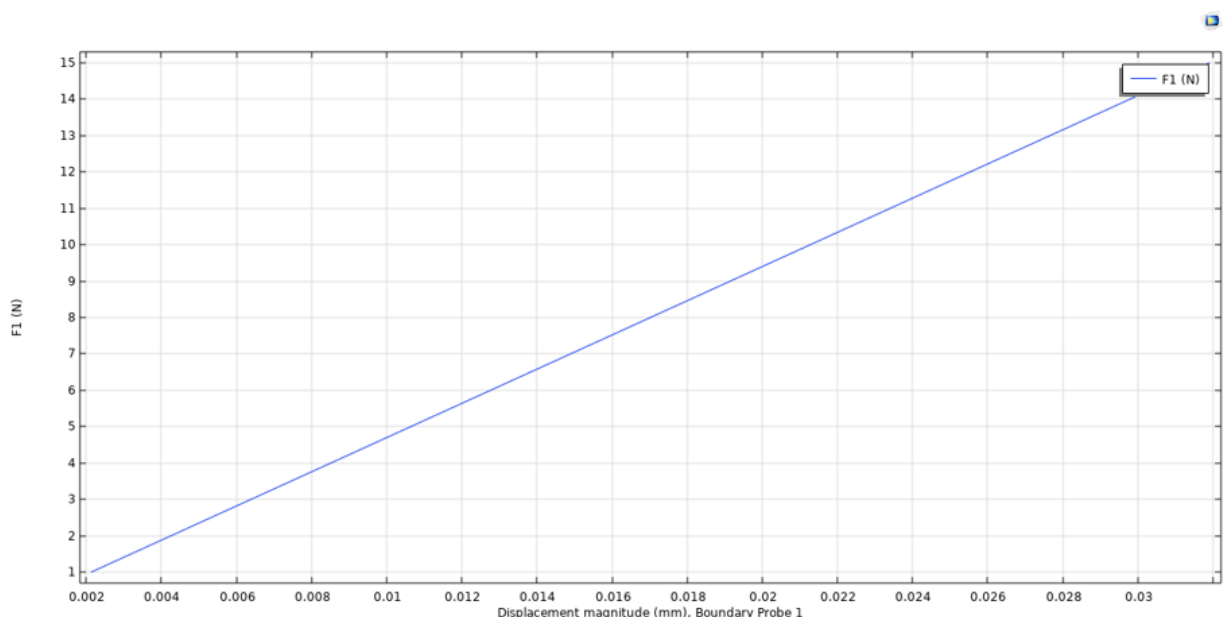


Figure 12.1: Mechanism force displacement plot.

The slope of plot in figure 12.1 gives an axial stiffness of 4.5×10^5 N/m. This is close to designed value of 4.5×10^5 N/m. This shows that the COMSOL model can be trusted for analysis.

12.3 Mechanical analysis

The following loadcases will be evaluated in the mechanical analysis.

- 100g acceleration in X direction
- 100g acceleration in Y direction
- 100g acceleration in Z direction
- +30 micron displacement in Z direction

The first three loadcases are the launch static accelerations typically used to make a preliminary check for a space component. The stresses developed due to these accelerations should be a factor 2 below the yield strength of the material for launch survival. The displacement in Z direction of the moving mass should be less than the stroke of the actuator to avoid a launch lock. The surface deformations are not checked for the first three cases as only survival of the components is important.

The last loadcase depicts the maximum stroke of the actuator. The stresses developed in the flexures should be a factor 2 below the fatigue strength of the flexure material for safe operation.

12.3.1 Boundary conditions

The boundary conditions are as follows. All the loadcases have a common mechanical boundary condition. The three housing mounting flanges are fixed in X, Y and Z directions. This is shown in figure 12.2.

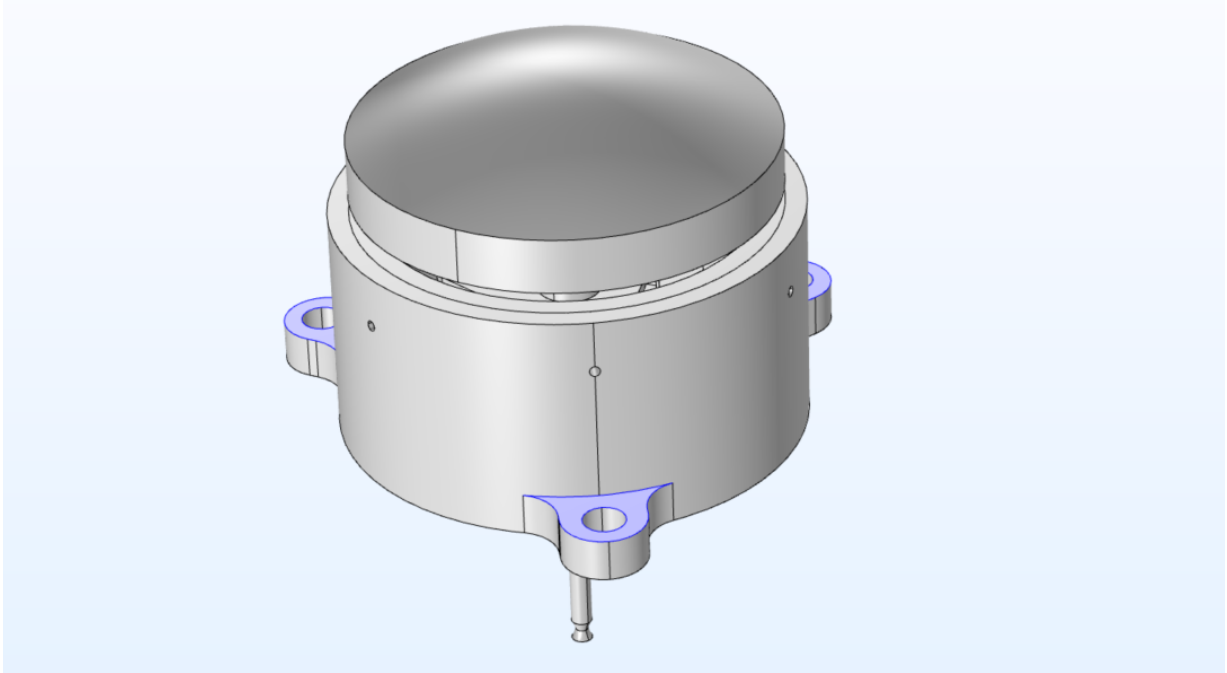


Figure 12.2: Fixed boundary condition is highlighted by the blue surfaces.

The strut has a spring foundation at its bottom flat surface which represents the stiffness of the actuator. This is shown in figure 12.3. The values for the spring are given in equation 12.1.

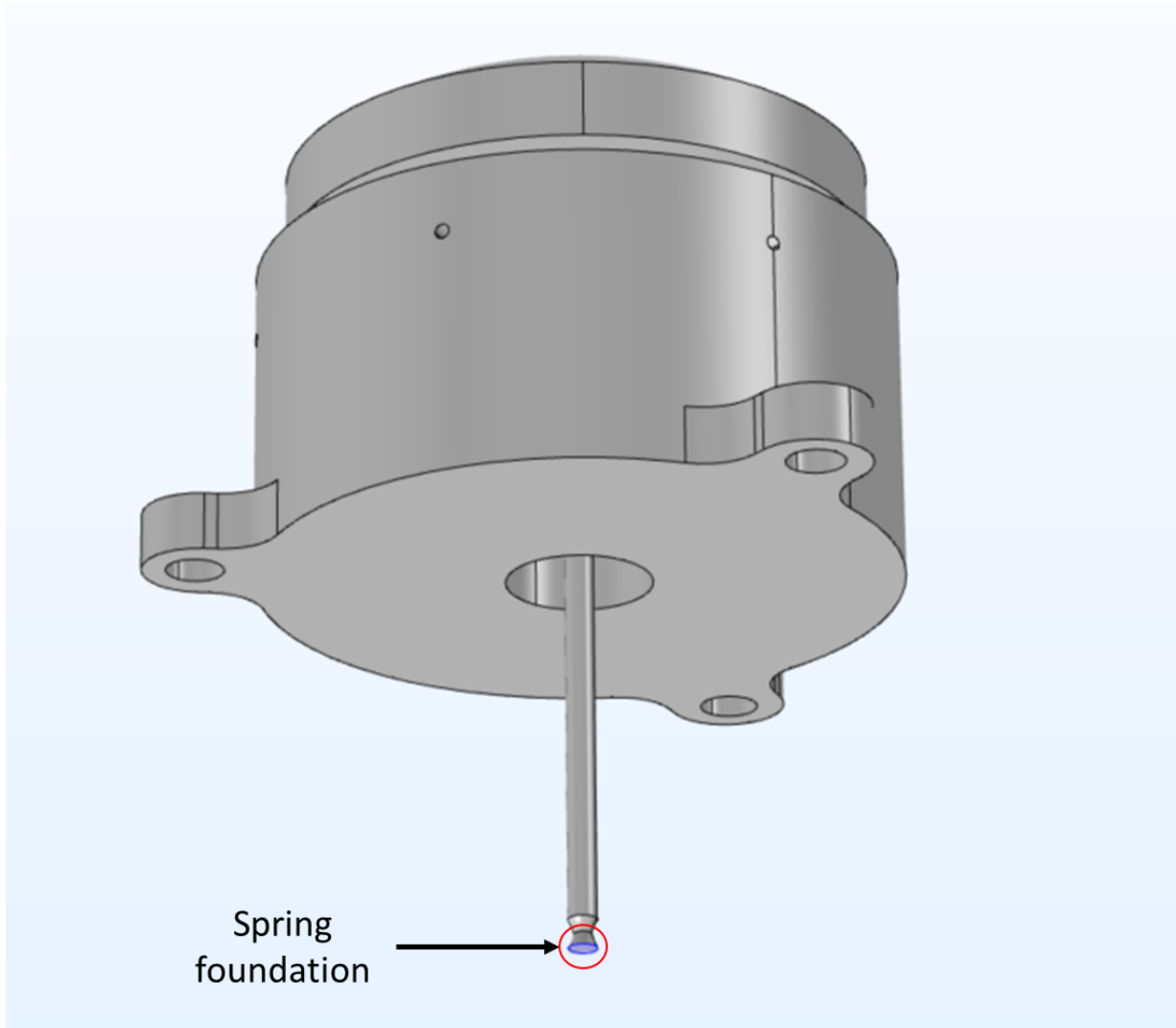


Figure 12.3: Spring foundation surface is highlighted by blue.

$$k = \begin{bmatrix} 1e8 & 0 & 0 \\ 0 & 1e8 & 0 \\ 0 & 0 & 4.5e5 \end{bmatrix} (N/m) \quad (12.1)$$

A mass is added at the bottom of the strut to represent the mass of the actuator mover.

The temperature of the entire assembly is 20 °C. All the other boundary conditions are described in their individual subsections.

12.3.2 100g acceleration in X direction

The boundary conditions for this loadcase is as follows. The assembly is subject to an acceleration of 100g in X direction. Figure 12.4a shows the stress distribution in it's deformed shape. The deformed shape is not to scale and is exaggerated to make the deformations visible. The maximum stress developed is 90 MPa. This is a stress concentration at the circular edge of the flat surface of the bottom notch. This maximum stress is well below the yield strength of the material which is 200 MPa. Majority of the housing has a stress of lower than 10 MPa which is 20 times lower than it's yield strength. Therefore, the housing and the strut are safe.

Further, figure 12.4b shows a max deformation of 5 μm . This is the tilt of the M2 mirror due to the bending of flexures. The amount of tilt is fine because this is a non-operational loadcase.

The stresses developed in the flexures is shown in figure 12.4c. A maximum stress of 45 MPa is developed at the edge of one of the flexures where it is attached to the hub. This is well below the yield strength of the material which is 1050 MPa. Therefore, the design is safe for this loadcase.

The stresses generated in the adhesive are shown in figure 12.4d. The maximum stress developed is 0.16 MPa. This is well below the ultimate strength of the adhesive and therefore it is safe.

The stresses in the mirror, outer ring and the bush are well below the yield strength and are not shown here. Overall, the design is safe for this loadcase.

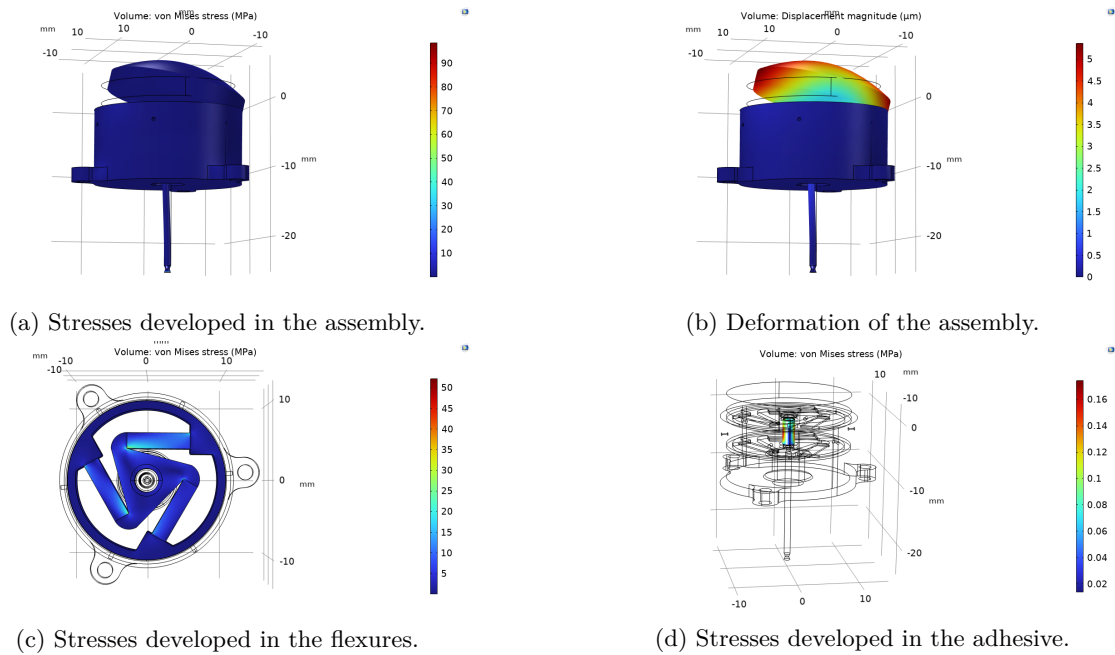


Figure 12.4: Results for launch acceleration in X direction.

12.3.3 100g acceleration in Y direction

The boundary conditions for this loadcase is as follows. The assembly is subject to an acceleration of 100g in Y direction. The results of this loadcase are expected to be similar to the previous loadcase as the mechanism is rationally symmetric. Figure 12.5a shows the stress distribution in it's deformed shape. The deformed shape is not to scale and is exaggerated to make the deformations visible. The maximum stress developed is 120 MPa. This is a stress concentration at the circular edge of the flat surface of the bottom notch. This maximum stress is well below the yield strength of the material which is 200 MPa. Majority of the housing has a stress of lower than 20 MPa which is 10 times lower than it's yield strength. Therefore, the housing and the strut are safe.

Further, figure 12.4b shows a max deformation of $5 \mu\text{m}$. This is the tilt of the M2 mirror due to the bending of flexures. The amount of tilt is fine because this is a non-operational loadcase.

The stresses developed in the flexures is shown in figure 12.5c. A maximum stress of 50 MPa is developed at the edge of one of the flexures where it is attached to the hub. This is well below the yield strength of the material which is 1050 MPa. Therefore, the design is safe for this loadcase.

The stresses generated in the adhesive are shown in figure 12.5d. The maximum stress developed is 0.16 MPa. This is well below the ultimate strength of the adhesive and therefore it is safe.

The stresses in the mirror, outer ring and the bush are well below the yield strength and are not shown here. Overall, the design is safe for this loadcase.

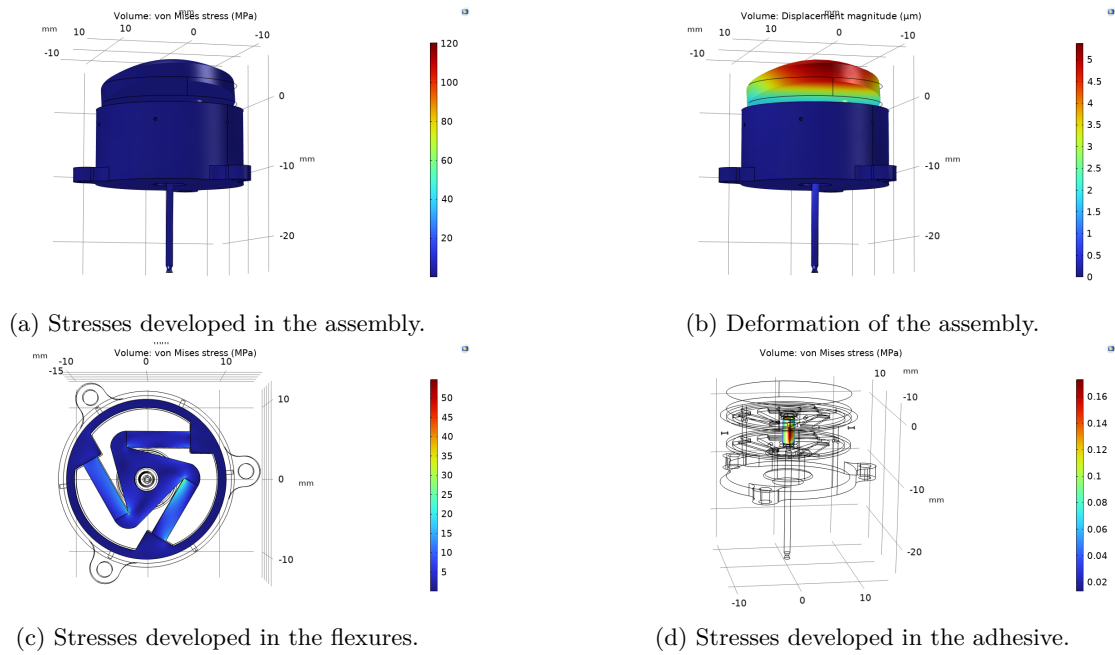


Figure 12.5: Results for launch acceleration in Y direction.

12.3.4 100g acceleration in Z direction

The boundary conditions for this loadcase are as follows. The assembly is subject to an acceleration of 100g in Z direction. Figure 12.6a shows the stress distribution in its deformed shape. The deformed shape is not to scale and is exaggerated to make the deformations visible. The maximum stress developed is 100 MPa. This is a stress concentration at the circular edge of the flat surface of the bottom notch. This maximum stress is half the yield strength of the material which is 200 MPa. Majority of the housing has a stress of lower than 20 MPa which is 10 times lower than its yield strength. Therefore, the housing and the strut are safe.

Further, figure 12.6b shows a max deformation of 20 μm . This is a Z translation of the M2 mirror due to the bending of flexures. The amount of translation is fine because this is a non-operational loadcase and the displacement is within the range of the RFM.

The stresses developed in the flexures are shown in figure 12.6c. A maximum stress of 35 MPa is developed at the outer edges of all the three flexures where it is attached to the outer ring. This is well below the yield strength of the material which is 1050 MPa. Therefore, the flexures are safe for this loadcase.

The stresses generated in the adhesive are shown in figure 12.6d. The maximum stress developed is 0.16 MPa. This is well below the ultimate strength of the adhesive and therefore it is safe.

The stresses in the mirror, outer ring and the bush are well below the yield strength and are not shown here. Overall, the design is safe for this loadcase.

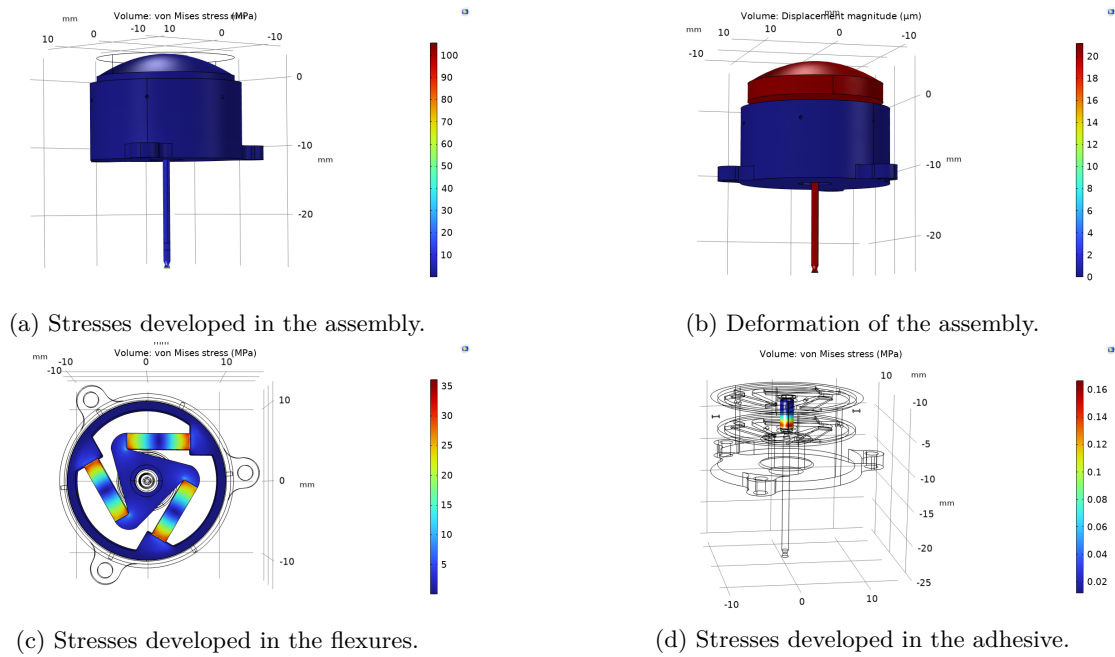


Figure 12.6: Results for launch acceleration in Z direction.

12.3.5 +30 micron displacement in Z direction

The boundary conditions for this loadcase is as follows. The bottom of the strut is prescribed to a displacement of 30 microns. Figure 12.7a shows the stress distribution in its deformed shape. The deformed shape is not to scale and is exaggerated to make the deformations visible. The maximum stress developed is 60 MPa. This appears at the ends of the flexures. This maximum stress is well below the fatigue strength of the material which is 1050 MPa. Majority of the housing has a stress of lower than 10 MPa which is 20 times lower than its yield strength. Therefore, the housing and the strut are safe.

Further, figure 12.7 shows a max deformation of 30 μm . This is a Z translation of the moving mass (M2 mirror and the strut). This is expected as it is the boundary condition.

The stresses developed in the flexures is shown in figure 12.7c. A maximum stress of 50 MPa is developed at the edges of all the three flexures. This is well below the yield strength of the material which is 1050 MPa. Therefore, the flexures are safe for this loadcase.

The stresses generated in the adhesive are shown in figure 12.7d. The maximum stress developed is 0.08 MPa. This is well below the ultimate strength of the adhesive and therefore it is safe.

The stresses in the mirror, outer ring and the bush are well below the yield strength and are not shown here. Overall, the design is safe for this loadcase.

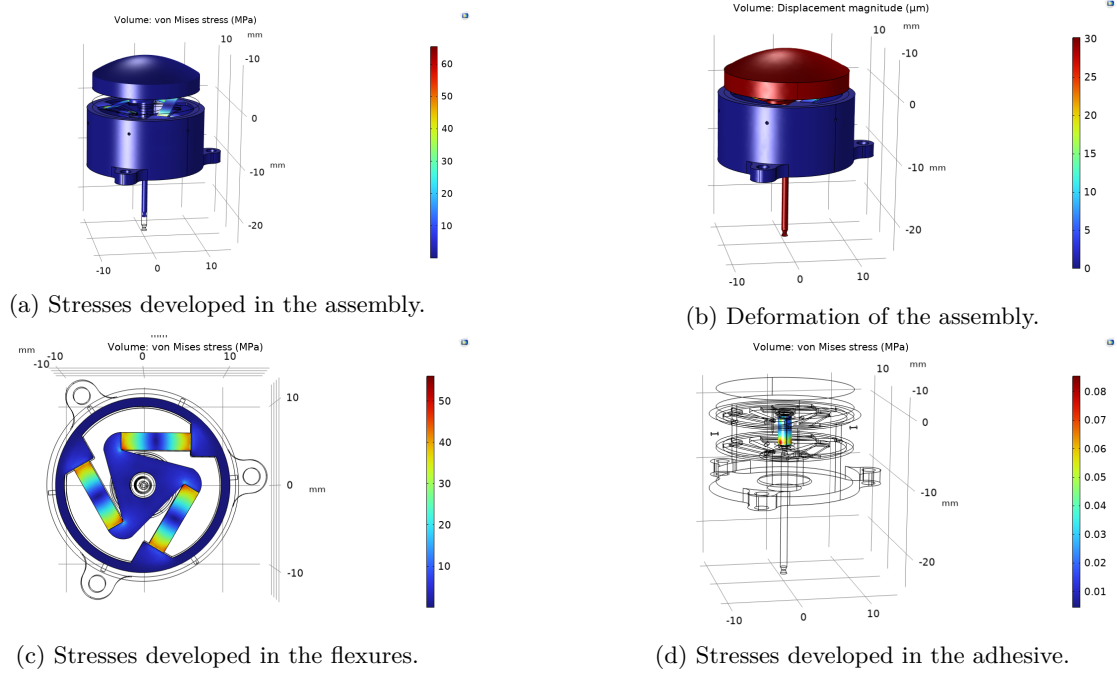


Figure 12.7: Results for a prescribed displacement of 30 microns.

12.3.6 Modal analysis

The modal analysis of the RFM assembly is carried out for the first 6 modes. Table 12.2 shows the mode frequency and mode shape.

The first mode is the actuated mode which is the axial translation of the mirror due to bending of flexures. The second and third modes are tip-tilt with similar mode frequency, The fourth mode is rotation of the mirror about it's axis. The fifth and sixth modes are the bending of the strut.

The non-actuated modes are above the random vibration spectrum of the launch which ranges from 10 Hz to 2000Hz[39]. This means that these modes will not be excited during launch.

Mode	Frequency	Type	Image
1	1116.5 Hz	Axial	

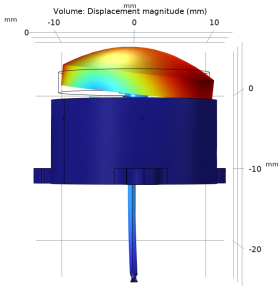
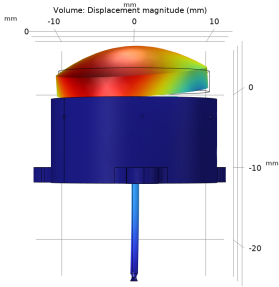
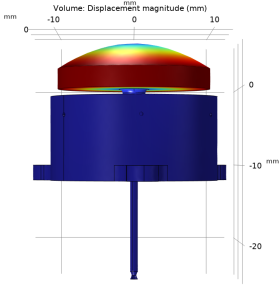
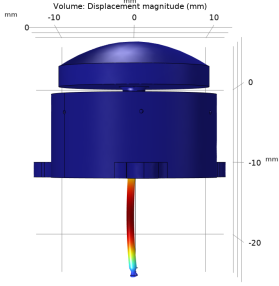
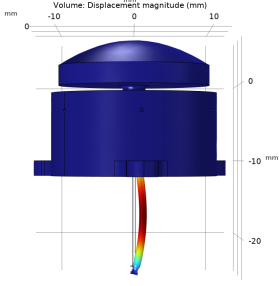
Mode	Frequency	Type	Image
2	2386.7 Hz	Tip-tilt	<p>Eigenfrequency=2386.7 Hz</p> 
3	2386.9 Hz	Tip-tilt	<p>Eigenfrequency=2386.9 Hz</p> 
4	3876.3 Hz	Mirror torsion	<p>Eigenfrequency=3876.3 Hz</p> 
5	5351.6 Hz	Strut bending	<p>Eigenfrequency=5351.6 Hz</p> 
6	5363.8 Hz	Strut bending	<p>Eigenfrequency=5363.8 Hz</p> 

Table 12.2: Modal analysis

12.4 Thermal analysis

The aim of the thermal simulation is to verify if the M2 mirror surface stays within specification of the WFE when exposed to different thermal load cases. The different load cases are listed below.

- Maximum operational temperature.
- Minimum operational temperature.
- Actuator + laser heat load.

12.4.1 Boundary conditions

The three mounting flanges of the housing are fixed in Z direction but are free to move in the X and Y direction. This is shown in figure 12.8. The spring foundation and added mass boundary conditions applied in subsection 12.3.1 are also applied here.

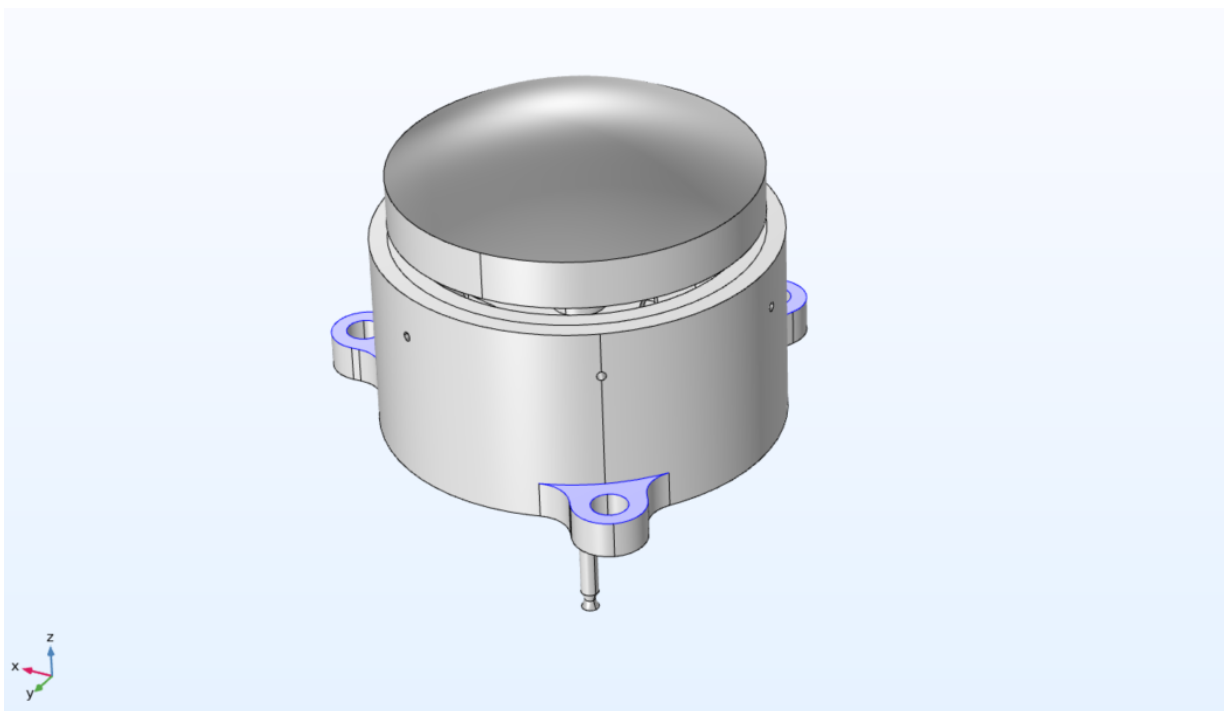


Figure 12.8: Roller boundary condition highlighted by the blue surfaces.

12.4.2 Mesh

The mesh of the entire assembly is free tetrahedral except the mirror surface which has a nearly axis symmetric mesh as shown in figure 12.9. This is important because the mirror surface displacement will be imported to a tool to calculate the WFE. An axis asymmetric mesh was initially used and it was found that the tool reported excessive tip-tilt.

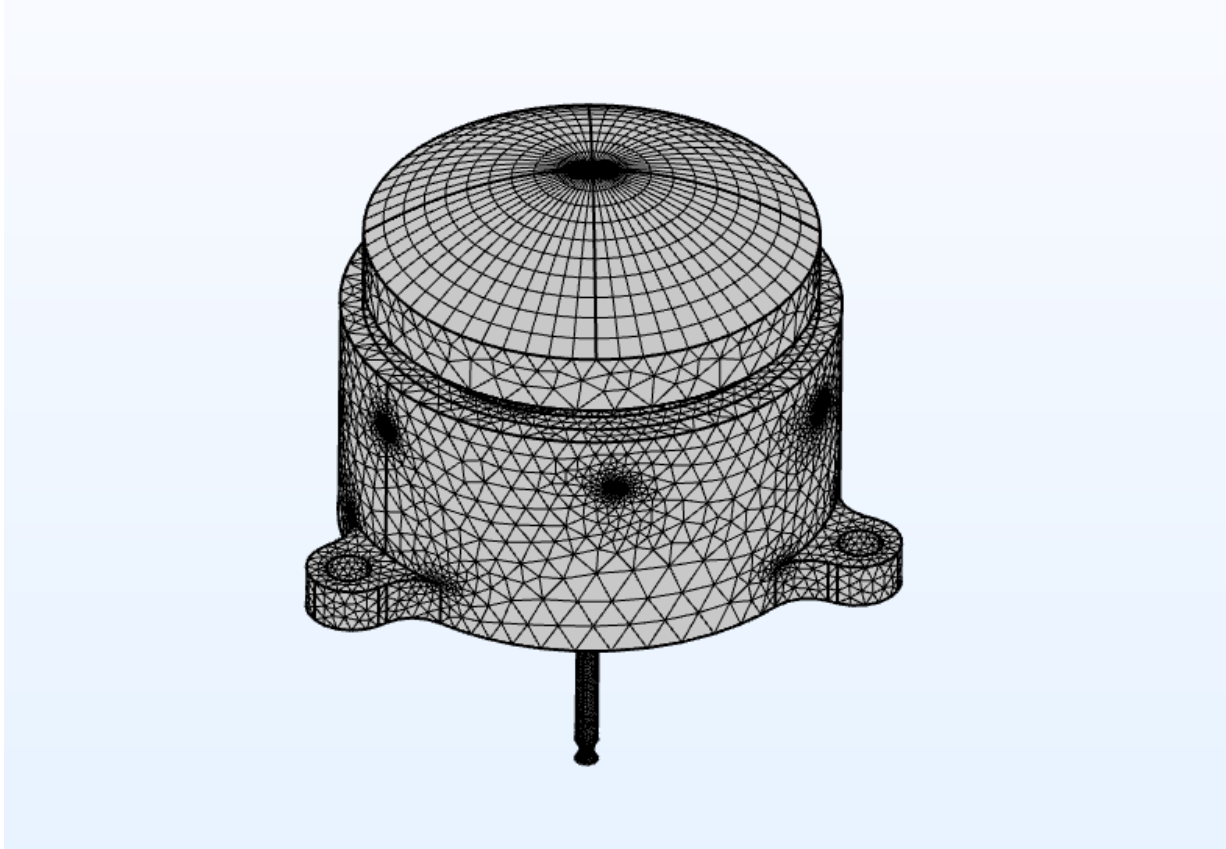


Figure 12.9: Mesh of the RFM assembly.

12.4.3 Maximum operational temperature

In this loadcase the entire RFM assembly is heated to a temperature of 35°C . The results for this loadcase are shown in figure 12.10. Figure 12.10a shows the temperature distribution of the RFM assembly. The stress distribution for this loadcase is shown in figure 12.10b. The maximum stress is 50 MPa in the bush. This is well below the yield strength of the material which is 200 MPa. Further, figure 12.10c shows the displacement of the RFM in z direction due to the thermal expansion. The maximum displacement is seen at the mirror with a magnitude of $8\ \mu\text{m}$. This is acceptable as the displacement is smaller than the range of the mechanism.

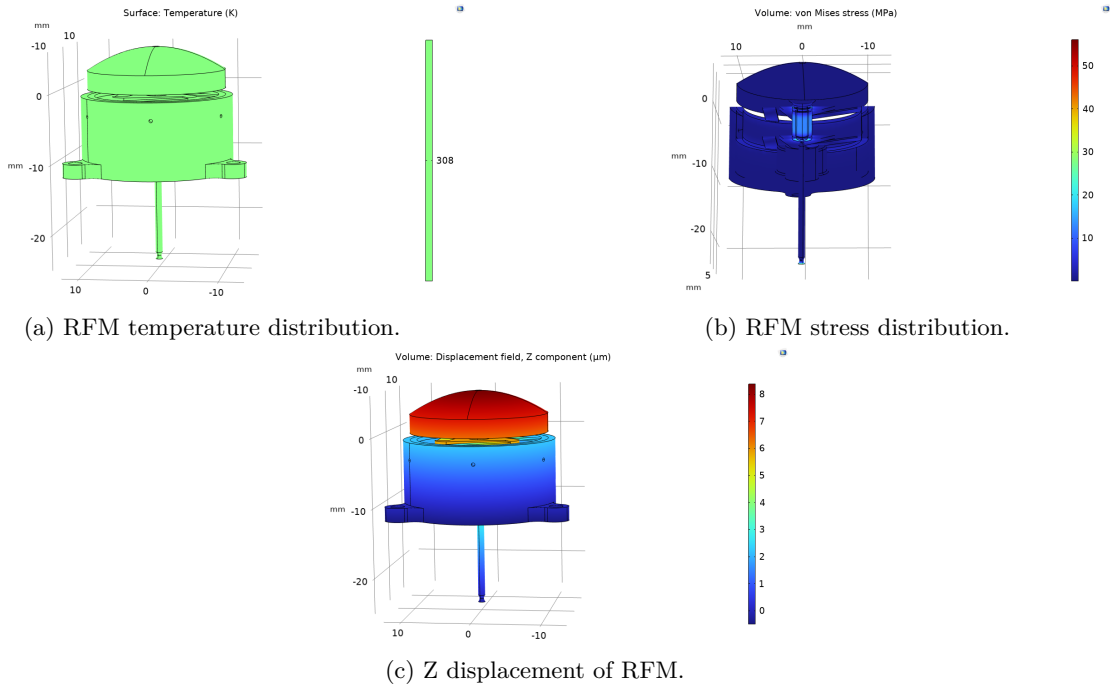


Figure 12.10: Maximum operational temperature loadcase.

Effect of mirror Z displacement

In case of uniform temperature change, the entire telescope will expand homogeneously. This will change the M1-M2 distance but still the telescope will operate nominally. Consider the original all aluminium telescope design without the RFM. In this case, it is important to check the z displacement of the M2 mirror with respect to the interface and compare it with the case which includes the RFM. For the first case the displacement of the M2 mirror is given by equation 12.2. This results in a displacement of $-11.2 \mu m$. The negative sign indicates that the direction of mirror displacement towards the interface.

$$\Delta l_{M2-I/F} = l_{M2-I/F} \alpha_{Al} \Delta T \quad (12.2)$$

The case in which the RFM is attached to the telescope is visualized in figure 12.11. In case of uniform temperature change the displacement of the mirror with respect to the interface is given by equation 12.3. This results in a displacement of $4.8 \mu m$. This proves that for the minimum operational temperature case, as the telescope contracts homogeneously, the net displacement that needs to be compensated is around $5.5 \mu m$. This is well within the range of the RFM.

$$\Delta l_{M2-I/F} = l_{M2} \alpha_{M2} \Delta T + l_S \alpha_S \Delta T - l_A \alpha_A \Delta T \quad (12.3)$$

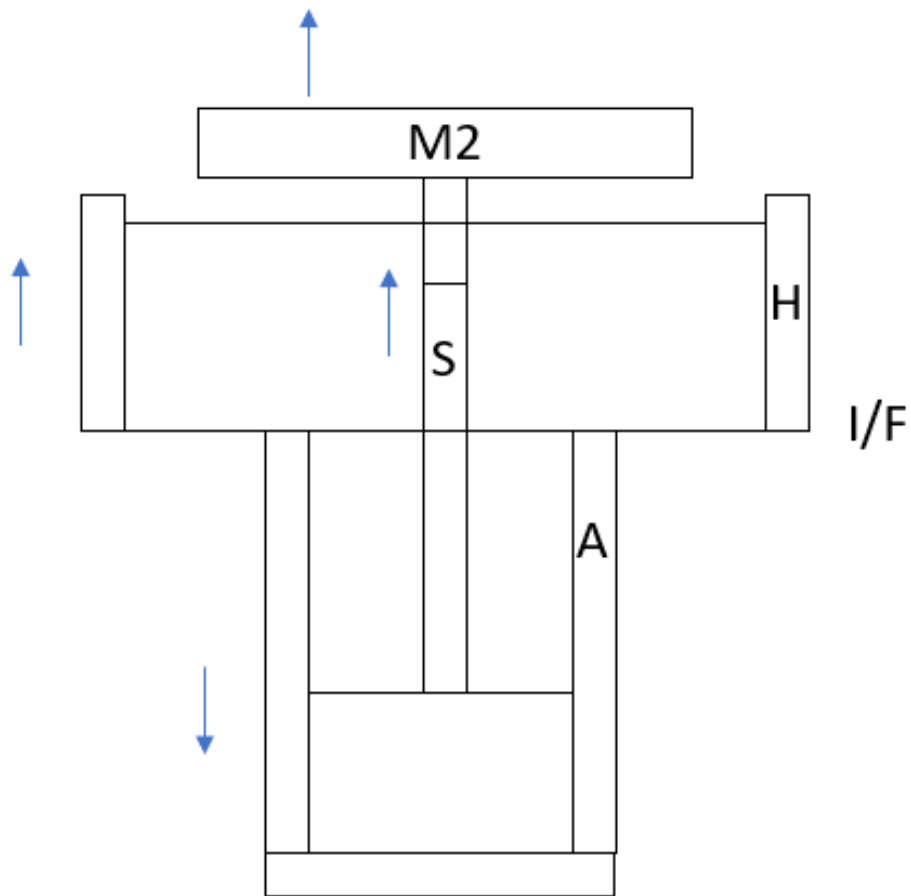


Figure 12.11: Schematic of thermal expansion. Here, M2: M2 mirror, S: strut, H: housing, A: actuator, I/F:RFM telescope interface.

In the COMSOL analysis this value is $8 \mu m$. This difference in magnitude of the analytical and COMSOL displacements can be explained by the fact that in the analytical calculation the flexures are considered fully compliant whereas in the COMSOL model they have a certain stiffness. This means that the thermal contraction of the housing adds to the displacement of the mirror resulting in a higher magnitude.

Effect of mirror deformation

The deformation of the mirror due to the temperature change introduces optical aberrations. To find the different types of aberrations, the deformed surface of the mirror was imported to a Zernike decomposition tool developed by TNO. The first 15 Zernike modes are shown in figure 12.12.

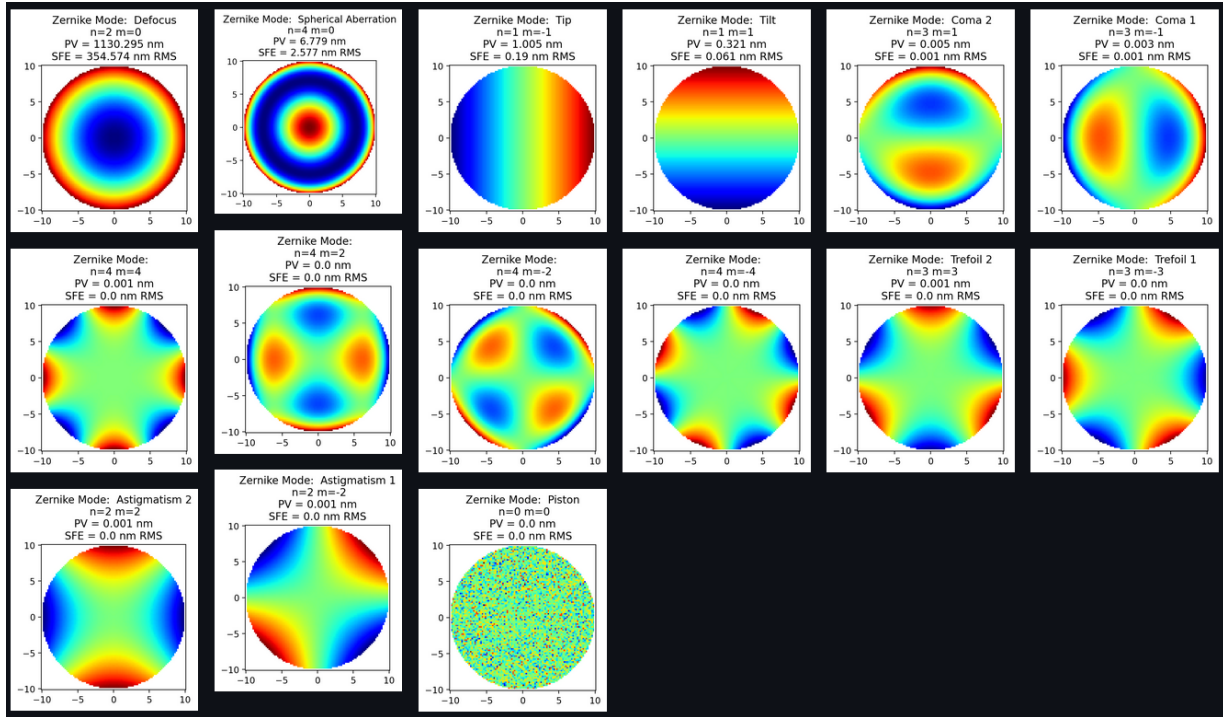


Figure 12.12: Zernike decomposition of the deformed mirror surface.

For a mirror the WFE is twice the surface form error (SFE). It is evident from the figure that defocus mode is the major contributor to the total WFE. But this could be compensated by the RFM. The other modes that are present are spherical aberration, tip, tilt. These are very small compared to the allowable WFE of 100 nm rms and therefore do not pose a problem. All the other aberrations are absent.

12.4.4 Minimum operational temperature

In this loadcase the entire RFM assembly is cooled to a temperature of -15°C . The results for this loadcase are shown in figure 12.13. Figure 12.13a shows the temperature distribution of the RFM assembly. The stress distribution for this loadcase is shown in figure 12.13b. The maximum stress is 120 MPa in the bush. This is below the yield strength of the material which is 200 MPa. Further, figure 12.13c shows the displacement of the RFM in z direction due to the thermal contraction. The maximum displacement is seen at the mirror with a magnitude of $-18 \mu\text{m}$. This is acceptable as the displacement is smaller than the range of the mechanism.

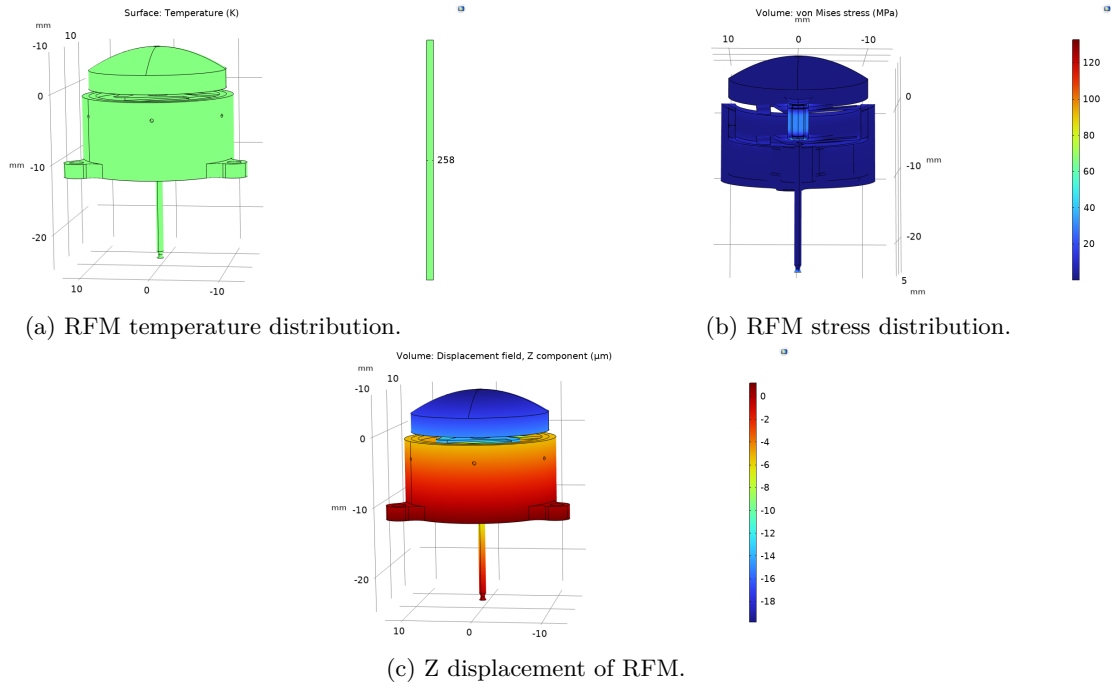


Figure 12.13: Minimum operational temperature loadcase.

Effect of mirror Z displacement

Consider the original all aluminium telescope design without the RFM. In case of uniform temperature change, the entire telescope will expand homogeneously. This will change the M1-M2 distance but still the telescope will operate nominally. In this case, it is important to check the z displacement of the M2 mirror with respect to the interface and compare it with the case which includes the RFM. For the first case the displacement of the M2 mirror is given by equation 12.2. This results in a displacement of $-11.2 \mu\text{m}$. The negative sign indicates that the direction of mirror displacement towards the interface.

The case in which the RFM is attached to the telescope is visualized in figure 12.14. In case of uniform temperature change the displacement of the mirror with respect to the interface is given by equation 12.3. This results in a displacement of $-12.9 \mu\text{m}$. This proves that for the minimum operational temperature case, as the telescope contracts homogeneously, the net displacement that needs to be compensated is around $5 \mu\text{m}$. This is well within the range of the RFM.

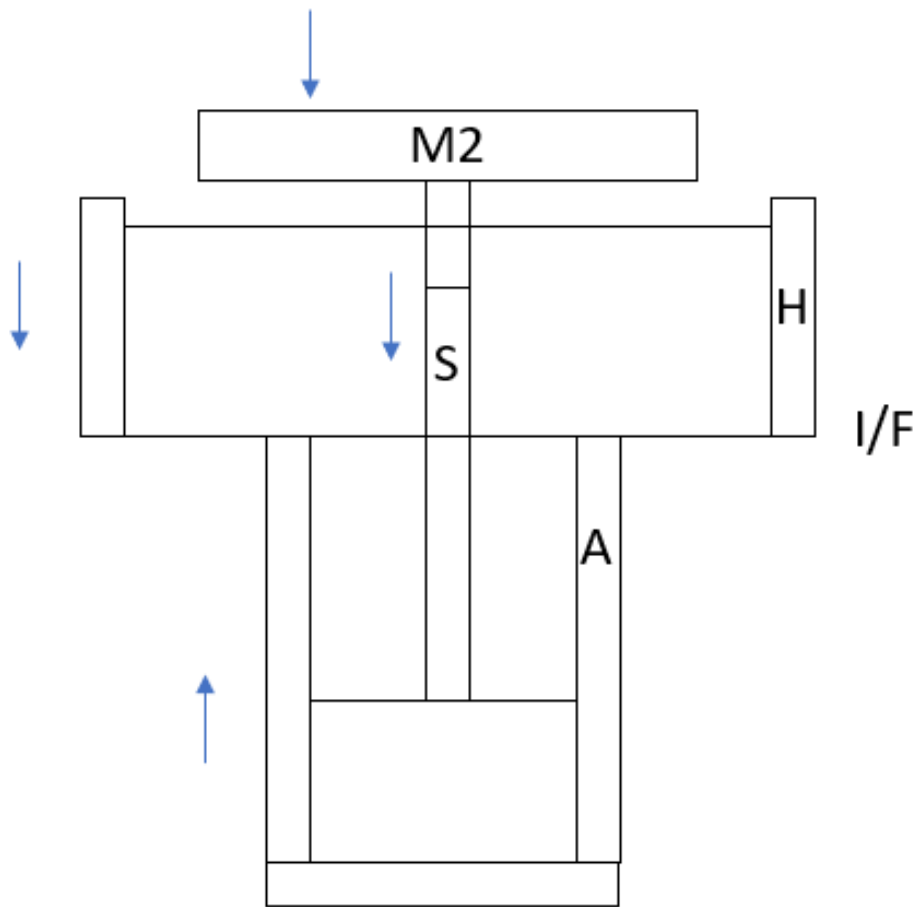


Figure 12.14: Schematic of thermal contraction. Here, M2: M2 mirror, S: strut, H: housing, A: actuator, I/F:RFM telescope interface.

In the COMSOL analysis this value is $-18 \mu m$. This difference in magnitude can be explained by the fact that in the analytical calculation the flexures are considered fully compliant whereas in the COMSOL model they have a certain stiffness. This means that the thermal contraction of the housing adds to the displacement of the mirror resulting in a higher magnitude.

Effect of mirror deformation

The Zernike modes for this loadcase are plotted by the same procedure followed in 12.4.3. The first 15 Zernike modes are shown in figure 12.15.

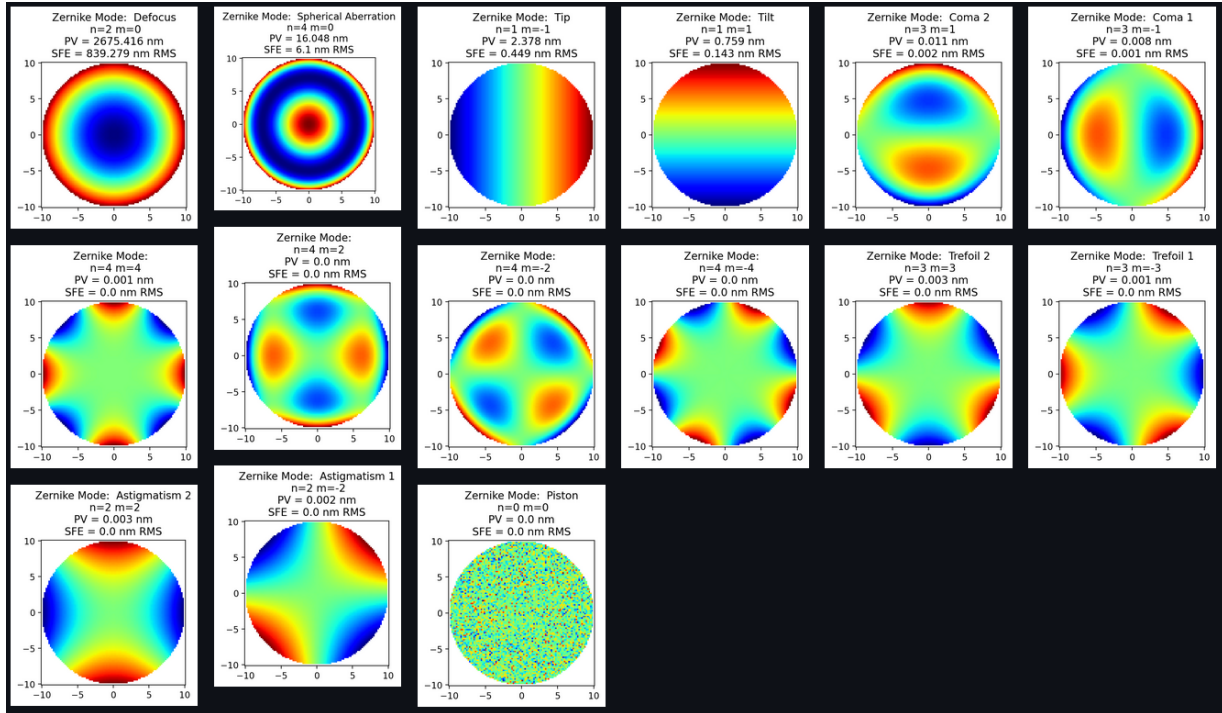


Figure 12.15: Zernike decomposition of the deformed mirror surface.

It is clear from the figure that again defocus mode is the major contributor to the total WFE. But this could be compensated by the RFM. The other modes that are present are spherical aberration, tip, tilt. These are very small compared to the allowable WFE of 100 nm rms and therefore do not pose a problem. All the other aberrations are absent.

12.4.5 Actuator + laser heat load

There are two sources of heat for this load case. One is the laser power absorbed by the mirror and the other is the heat generated by the actuator. The M2 mirror is made of aluminium. The reflectance of aluminium at a wavelength of 1550 nm is around 95% [40]. Therefore, the heat absorbed from the laser is assumed to be 5 percent of the laser source power. This is modelled as a heat rate over the entire reflecting surface of the mirror. The power consumed by the actuator was shown to be 0.05 W in subsection 11.5. It is assumed that all of actuator power is dissipated as heat which is seen as the worst case scenario. Although this is an unrealistic situation, it is a good way to ensure that the RFM can handle the heat load. If it turns out that the heat load is too much then a better estimate will have to be made.

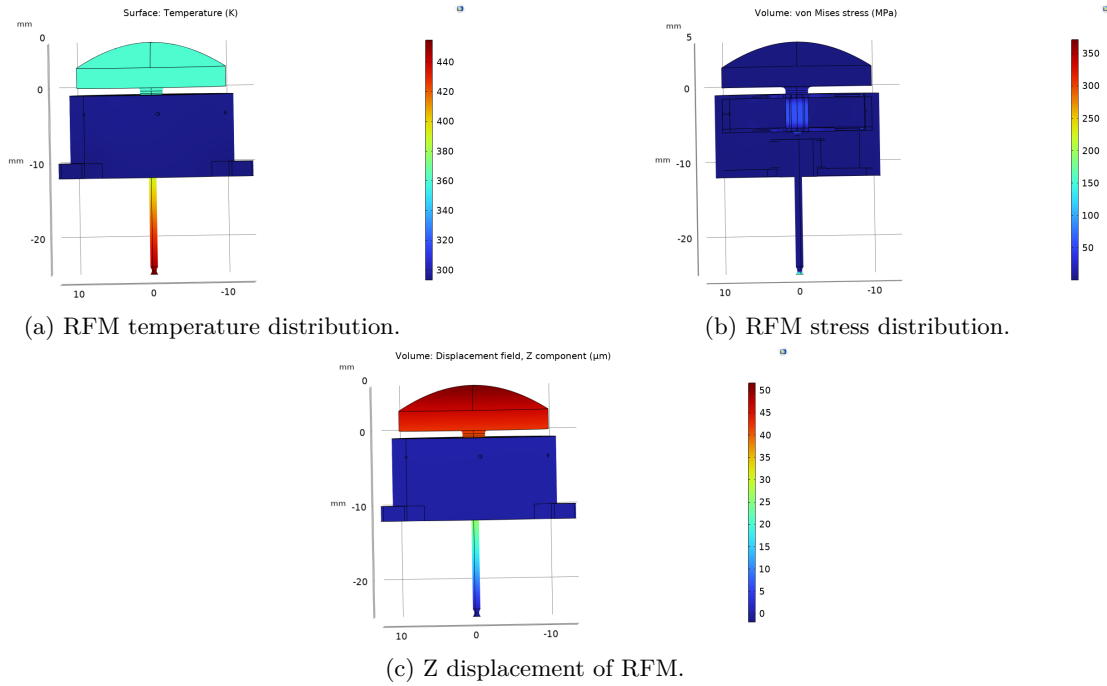


Figure 12.16: Laser+actuator loadcase.

Stress distribution RFM

In the previous section, the analysis showed a peak stress of 250 MPa in the RFM assembly. This stress level is well above the yields stress of some of the materials. Therefore, it is studied in more detail here.

The plot of stress value greater than 150 MPa is shown in figure 12.17. Sub-figure 12.17a shows that stress in most parts of the RFM assembly is below 150 MPa. This view is magnified and shown in figure 12.17b. This shows that the stress above 150 MPa is stress concentration at the bottom flat surface of the strut. This is a consequence of the spring foundation boundary condition and therefore unrealistic. As a result, the assembly is safe in this loadcase.

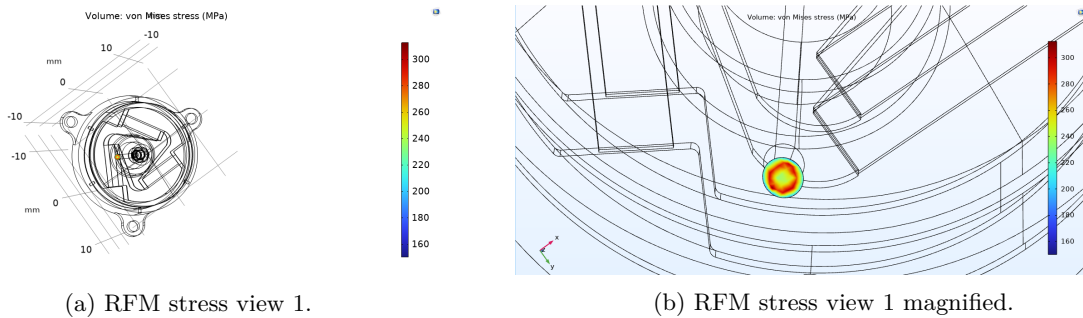


Figure 12.17: Stress detail for laser+actuator loadcase.

Effect of mirror deformation

The Zernike modes for this loadcase are plotted by the same procedure followed in 12.4.3. The first 15 Zernike modes are shown in figure 12.18.

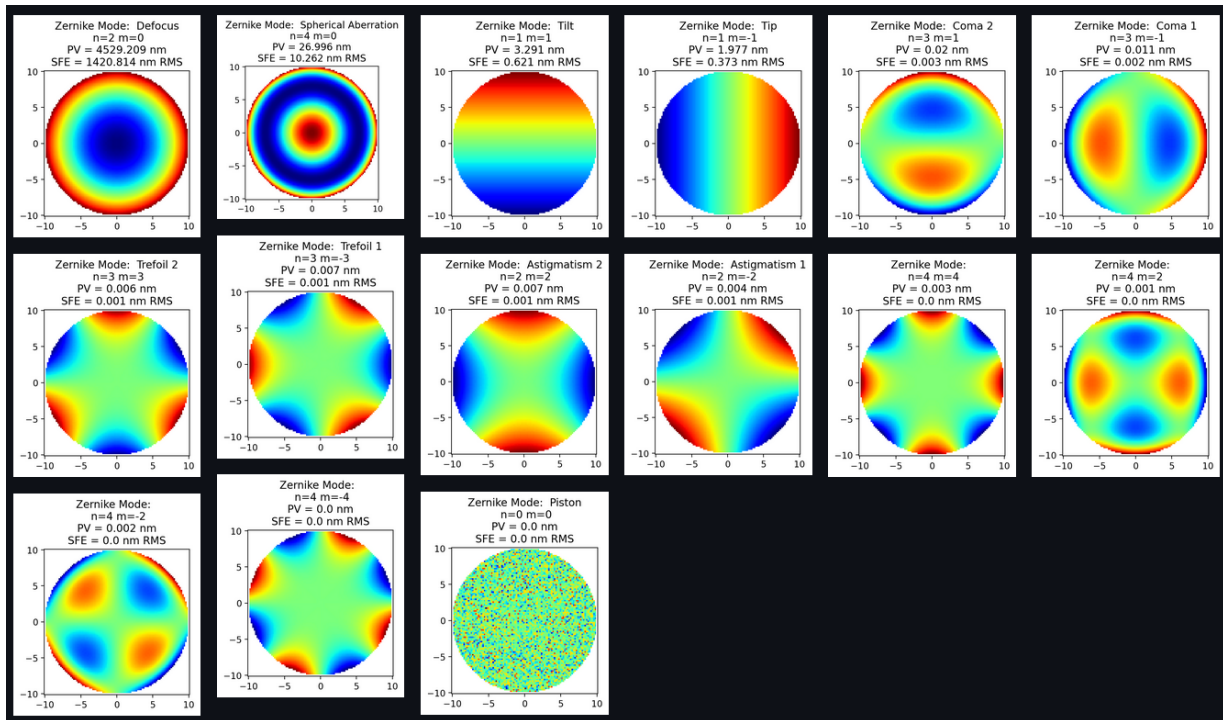


Figure 12.18: Zernike decomposition of the deformed mirror surface.

It is clear from the figure that again defocus mode is the major contributor to the total WFE. But this could be compensated by the RFM. The other modes that are present are spherical aberration, tip, tilt. These are very small compared to the allowable WFE of 100 nm rms and therefore do not pose a problem. All the other aberrations are absent.

12.5 Summary

The summary of mechanical load cases is presented in table 12.3. The stresses developed in all the mechanical loadcases are within the yield strength of the material and therefore, the design is safe during launch.

No.	Load case	σ_{max} (MPa)	Max. displacement (μm)	T ($^{\circ}C$)	Comment
1	100g X	30 @ top flexure inner ends	5 @ mirror (tilt)	20	Safe
2	100g Y	60 @ upper notch	5 @ mirror (tilt)	20	Safe
3	100g Z	30 @ flexure outer ends and notches	10 @ moving mass (Z)	20	Displacement < stroke. Low because actuator mass not included yet. After act. mass expected displacement is 18
4	+30 μm Z	80 @ flexure ends	30 (Z)	20	Safe

Table 12.3: Summary of mechanical load cases.

The summary of thermal load cases is presented in table 12.4.

No.	Load case	σ_{max} (MPa)	Max. displacement (μm)	T_{max} ($^{\circ}C$)	Comment
5	+35 deg C	40 @ bush	8 (Z)	35	Safe
6	-15 deg C	120 @ bush	-18 (Z)	-15	Safe
7	Laser 0.15W + Actuator 0.05 W	100 @ bush	51 (Z)	437 @ lower notch flat surface	$\sigma_{conc.}=350$, @ strut bottom due to boundary condition, displacement>stroke.

Table 12.4: Summary of thermal load cases.

12.6 Conclusion

Mechanical load cases

The designed RFM will survive launch as the stresses in all the metal parts are a factor 2 below the material yield strength. The stress developed in adhesive is well below the material strength. The maximum displacement of the moving parts is 20 micron which is below the stroke of 30 micron.

The flexures are safe at maximum displacement as the stresses generated are a factor 20 times lower than the material fatigue strength.

Modal analysis shows that the higher modes are above the random vibration spectrum of the launch. Therefore, no launch lock is required.

Thermal load cases

The stresses developed due to the thermal loadcases are well below the yield strength and therefore, the RFM is mechanically safe. The Zernike decomposition of the deformed mirror surface shows defocus to be the major contributor.

Chapter 13

Conclusion and recommendations

13.1 Conclusion

First, the working of the laser communication terminal was studied to understand the working of a laser communication terminal. This led to the understanding of the on-board detectors and the PAT strategy. A literature survey showed that a refocusing mechanism has never been used for a laser satellite communication telescope.

An optical simulation was carried out for the Rx laser beam. This showed that the optical fiber can be used to detect small defocus error and the ACQ camera can be used to detect large focus error. Further, the Tx beam was simulated and it was shown that the telescope is more sensitive to the Tx beam than the Rx beam.

A refocusing system was designed with two use case scenarios based on the existing PAT strategy. A trade-off was performed to choose an optical component to actuate. This resulted in the decision to actuate the telescope M2 mirror it is the most sensitive and it brings the telescope to nominal operation. Extremum seeking control was simulated in simulink to show that it can be used to close the loop and refocus in the presence of jitter. Based on the above analysis and trade-offs, mechanism requirements were derived on a system level.

A functional design of the mechanism was created which consists of the M2 mirror, a guidance, an actuator, a coupling and a housing. The actuator selection was done by considering different actuation principles and picking the most suitable for the requirements. As a result, hybrid reluctance actuator was selected because of its power efficiency, suitable range and resolution.

A trade-off was performed to choose the tangential flexure concept for the guidance of the M2 mirror. A compliant strut was designed to connect the actuator to the mirror and compensate for misalignment. Mirror mount, housing and interfaces were designed and dimensioned.

FEM simulation was carried out to check the stresses induced in the RFM due to launch loads and thermal loads. The stresses in the RFM were found to be well below failure limit for the launch load case. Thermal simulation showed that the RFM is mechanically safe. However, the displacement of the mirror is large in the laser+actuator heat load case. This problem can be solved in two ways. a)By carrying the heat away from the mirror or b)increasing the range of the mechanism.

Overall, it was shown that the designed active refocusing mechanism can be used for a laser satellite communication telescope.

13.2 Recommendations

Although the design meets most of the requirements some recommendations are made to further improve the design.

13.2.1 Mechanism design

The design of the guidance can be further improved to be more stable. The distance between the two membranes needs to be increased the stiffness against tip-tilt motion. A solution could be to sandwich the actuator between the membranes.

13.2.2 Actuator design

The actuator in the current design is not tailor made for the application. The actuator could be scaled to reduce the length and therefore, reduce the total length of the telescope.

13.2.3 Actuator and laser heat load case

The loadcase simulated here is only an estimate. The resulting thermo-mechanical deformation is larger than the stroke of the actuator. Firstly, the actuator heat load is an assumption and the thermal heat path needs to be accurately modelled. If the large displacements persist then there could be two possible solutions. First: To carry the heat away from the mirror. This can be done in one of the two ways. a) To coat the mirror surface to reduce the laser absorption. b) To provide a flexible conductive heat path. Second: To increase the range of the actuator.

13.2.4 Manufacturing and assembly

The manufacturing aspect needs to be detailed. Here, only a possible solution is suggested. An alignment plan has to be made to integrate the RFM with the telescope and make sure the two telescope mirrors are properly aligned.

13.2.5 RFM stability

The stability of the mechanism during the ACQ phase is important as it will operate in open loop. This needs to be tested to ensure the ACQ phase is successful.

Appendix A

Mechanisms

The FACT(Freedom and constraint topology) sheet is a library of parallel compliant mechanisms. For a one degree of freedom translation, the flexures must lie in two parallel planes perpendicular to the direction of motion. This is shown in figure A.1[41] in number 3 under the column named 1 DOF.

Complete Library for Parallel Systems

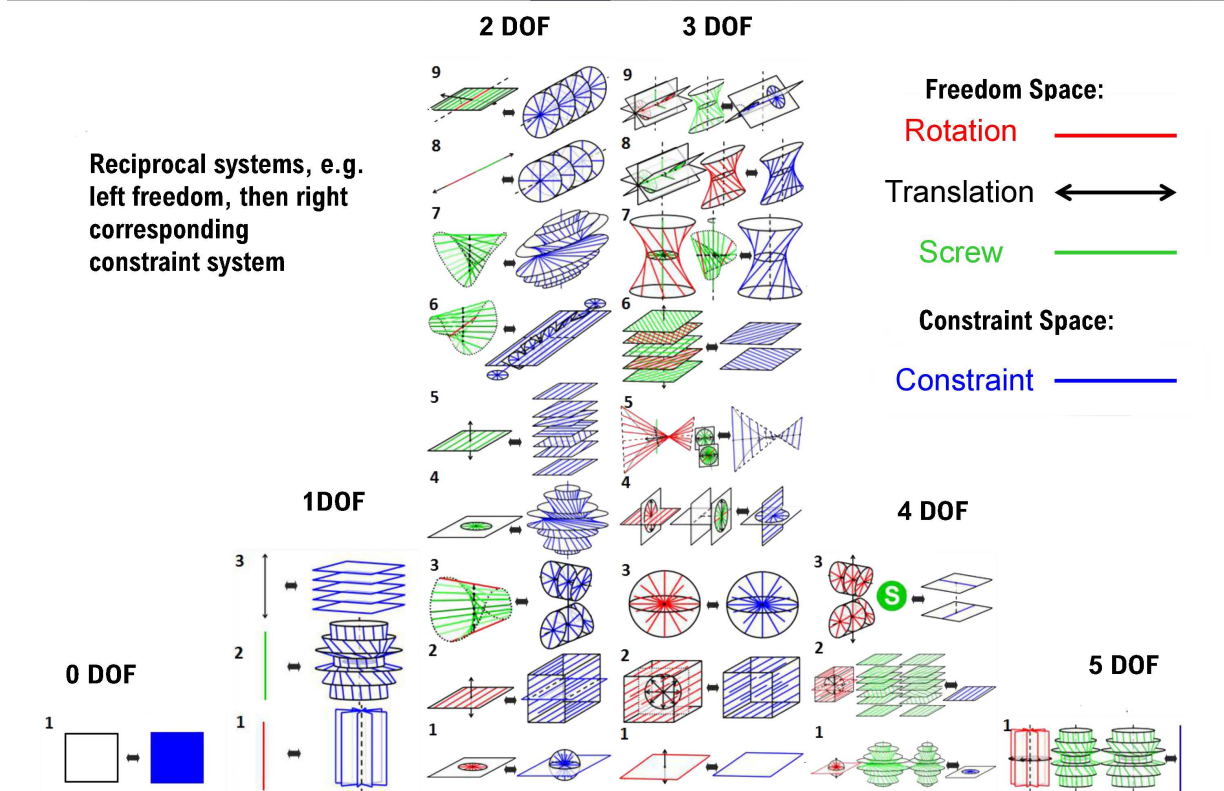
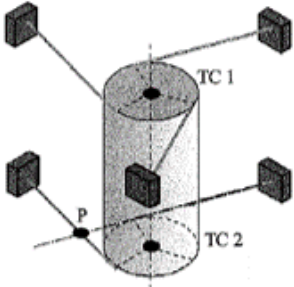
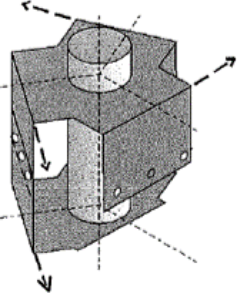
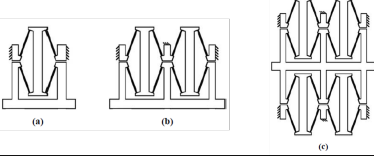
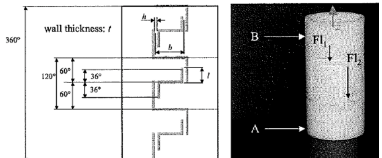
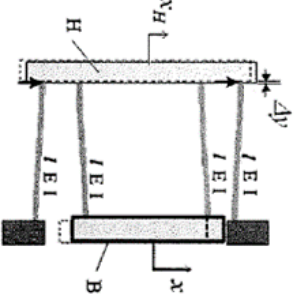
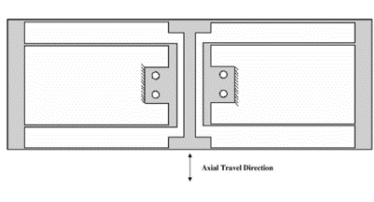
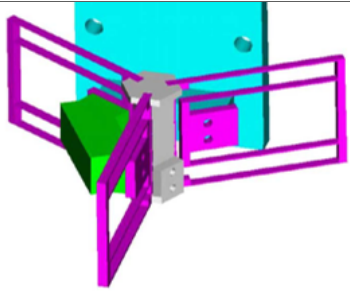


Figure A.1: FACT sheet.

Further, all the flexure mechanisms considered during the project are summarized.

	Mechanism	Name	DoF	Comments
1		Tangential flexure	1	<ul style="list-style-type: none"> Exactly constrained Low radial stiffness
2		Folded leaf flexure	1	Exactly constrained
3		X-Bob	(a)2 (b)1 (c)-1	Planar mechanism
4		Compliant tube	1	Suitable for lens group
5		Compound leaf flexure	2	<ul style="list-style-type: none"> Under constrained Susceptible to vibrations
6		Planar folded beam	1	<ul style="list-style-type: none"> Exactly constrained Motion range twice of 5 for same size of flexures
7		Spatial folded beam	-	Uniform radial stiffness

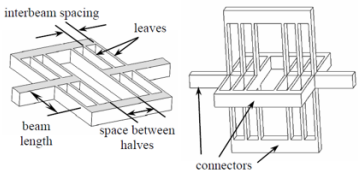
8		Compliant translational joint	-2	<ul style="list-style-type: none"> • Overconstrained • High and uniform radial stiffness
---	---	-------------------------------	----	--

Table A.1: 1 DoF linear motion mechanisms.

The mechanisms can be divided into two classes. 1) Planar flexure mechanisms 2) Rotationally symmetric flexure mechanisms. The second class of mechanism is preferred because it gives uniform radial stiffness. This eliminates mechanism 3, 5 and 6. In the remaining. Mechanism 4 is a form of tube and is susceptible to bending. Mechanism 7 has a complex design and mechanism 8 is overconstrained to increase the radial stiffness. Overall, mechanisms 1 and 2 have good potential.

Appendix B

Optical simulation

In section 5.1 it was assumed that the Rx beam is Gaussian. This was done to simplify the analysis. However, in reality the Rx beam that enters the telescope will have a top hat profile. This will result in an Airy disk at the detector plane. An Airy disk can have zero intensity at the center as the image plane is translated through focus. This can be a problem for extremum seeking control as a loss of signal may result in failure to refocus. A simulation of the Airy disk through focus is carried out in LightPipes[42] optical toolbox. The Airy disk profiles for different defocus distances is shown in figure B.1. It is clear that there is no zero intensity at the center for different defocus distances.

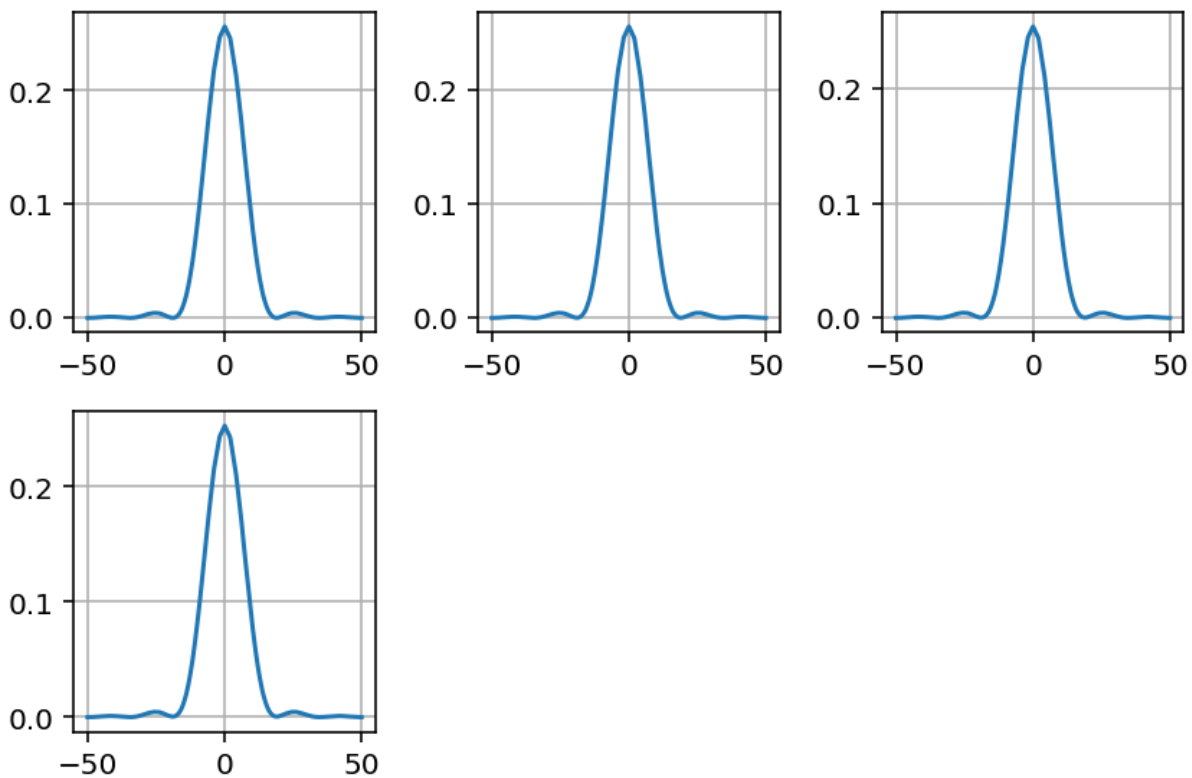


Figure B.1: Airy disk through focus. The defocus from left to right is 0, 20, 40, 60 μm .

Bibliography

- [1] H. Hemmati, *Near-earth laser communications*. CRC press, 2020.
- [2] H. Zech, F. Heine, and M. Motzigemba, “Laser communication terminals for data relay applications: Today’s status and future developments,” in *2017 IEEE International Conference on Space Optical Systems and Applications (ICSOS)*. IEEE, 2017, pp. 193–198.
- [3] R. Saathof, R. den Breeje, W. Klop, S. Kuiper, N. Doelman, F. Pettazzi, A. Vosteen, N. Truyens, W. Crowcombe, J. Human *et al.*, “Optical technologies for terabit/s-throughput feeder link,” in *2017 IEEE International Conference on Space Optical Systems and Applications (ICSOS)*. IEEE, 2017, pp. 123–129.
- [4] “Superfast internet using laser-satellite communications,” <https://www.tno.nl/en/tno-insights/articles/superfast-internet-using-laser-satellite-communications/>.
- [5] M. A. Khalighi and M. Uysal, “Survey on free space optical communication: A communication theory perspective,” *IEEE communications surveys & tutorials*, vol. 16, no. 4, pp. 2231–2258, 2014.
- [6] H. Henniger and O. Wilfert, “An introduction to free-space optical communications.” *Radioengineering*, vol. 19, no. 2, 2010.
- [7] “Satellite frequency bands,” https://www.esa.int/Applications/Telecommunications_Integrated_Applications/Satellite_frequency_bands.
- [8] A. G. Alkholidi, K. S. Altowij *et al.*, “Free space optical communication theory and practices,” *Contemporary Issues in Wireless Communications*, pp. 159–212, 2014.
- [9] H. Kaushal and G. Kaddoum, “Optical communication in space: Challenges and mitigation techniques,” *IEEE communications surveys & tutorials*, vol. 19, no. 1, pp. 57–96, 2016.
- [10] “Ucs satellite database,” <https://www.ucsus.org/resources/satellite-database>.
- [11] Z. Ghassemlooy and W. O. Popoola, *Terrestrial free-space optical communications*. InTech, 2010.
- [12] M. Arumugam, “Optical fiber communication an overview,” *Pramana*, vol. 57, no. 5, pp. 849–869, 2001.
- [13] R. C. Olsen, *Remote sensing from air and space*. SPIE Press, 2007, vol. 162.
- [14] L. D. Feinberg, B. H. Dean, W. L. Hayden, J. M. Howard, R. A. Keski-Kuha, and L. M. Cohen, “Space telescope design considerations,” *Optical Engineering*, vol. 51, no. 1, p. 011006, 2012.
- [15] W. J. Smith, *Modern optical engineering: the design of optical systems*. McGraw-Hill Education, 2008.
- [16] W. Wetherell and M. Rimmer, “General analysis of aplanatic cassegrain, gregorian, and schwarzschild telescopes,” *Applied Optics*, vol. 11, no. 12, pp. 2817–2832, 1972.
- [17] L. Kramer, J. Peters, R. Voorhoeve, G. Witvoet, and S. Kuiper, “Novel motorization axis for a coarse pointing assembly in optical communication systems,” *IFAC-PapersOnLine*, vol. 53, no. 2, pp. 8426–8431, 2020.
- [18] S. Kuiper, W. Crowcombe, J. Human, B. Dekker, E. Nieuwkoop, A. Meskers, G. Witvoet, L. Kramer, M. Lemmen, H. Lagemaat *et al.*, “High-bandwidth and compact fine steering mirror development for laser communications,” in *17th European space mechanisms and tribology symposium*, 2017.
- [19] “Optical fiber image,” <https://www.thorlabs.com/images/xlarge/22502-xl.jpg>.

- [20] “Quadcell image,” <https://www.hamamatsu.com/eu/en/product/type/G6849/index.html>.
- [21] “Camera image,” <https://www.hamamatsu.com/eu/en/product/type/G14674-0808W/index.html>.
- [22] M. Silva-López, D. Garranzo-García, A. Sánchez, J. A. Bonet-Navarro, A. Nuñez, and A. Álvarez-Herrero, “Analysis and evaluation of the full disk telescope refocusing mechanism for the solar orbiter mission,” *Optical Engineering*, vol. 54, no. 8, p. 084104, 2015.
- [23] M. Lee, J. Kim, J.-S. Chang, and M.-S. Kang, “Development of in-orbit refocusing mechanism for spaceeye-1 electro-optical payload,” in *Earth Observing Systems XXI*, vol. 9972. International Society for Optics and Photonics, 2016, p. 99721O.
- [24] Y. Michel, E. Condé, D. Kouach, M. Simpfendorfer, Y. Parot, G. Orttner, M. Saccoccio, and S. Maurice, “Chemcam screw/nut autofocus mechanism: qualification data and guidelines for space-use of ground equipments,” in *Proc. 13th European Space Mechanisms and Tribology Symposium-(ESMATS 2009)*, 2009.
- [25] A. Franzoso and R. D’Imporzano, “A sub-micrometric thermal refocussing mechanism for high resolution eo telescopes.” 45th International Conference on Environmental Systems, 2015.
- [26] O. Selmoglu, M. Ekinici, and O. Karci, “Thermal refocusing method for spaceborne high-resolution optical imagers,” *Applied optics*, vol. 55, no. 15, pp. 4109–4112, 2016.
- [27] “Piezo actuators and electronics,” <https://www.cedrat-technologies.com/en/technologies/actuators/piezo-actuators-and-electronics.html>.
- [28] G. R. Fowles, *Introduction to modern optics*. Courier Corporation, 1989.
- [29] R. E. Wagner and W. J. Tomlinson, “Coupling efficiency of optics in single-mode fiber components,” *Applied optics*, vol. 21, no. 15, pp. 2671–2688, 1982.
- [30] P. F. Goldsmith, “Gaussian beam propagation,” 1998.
- [31] K. B. Ariyur and M. Krstic, *Real-time optimization by extremum-seeking control*. John Wiley & Sons, 2003.
- [32] S. L. Brunton, X. Fu, and J. N. Kutz, “Extremum-seeking control of a mode-locked laser,” *IEEE Journal of Quantum Electronics*, vol. 49, no. 10, pp. 852–861, 2013.
- [33] “Cylindrical housed linear voice coil actuator,” <https://www.sensata.com/products/motors-actuators/voice-coil-actuators/cylindrical-housed-linear-voice-coil-actuator>.
- [34] S. Kuiper, N. Doelman, T. Overtoom, E. Nieuwkoop, T. Russchenberg, M. van Riel, J. Wildschut, M. Baeten, H. Spruit, S. Brinkers *et al.*, “Electromagnetic deformable mirror for space applications,” in *International Conference on Space Optics/ICSO 2016*, vol. 10562. International Society for Optics and Photonics, 2017, p. 1056230.
- [35] H. Soemers, “Design principles for precision mechanisms,” 2010.
- [36] “Vibroacoustic qualification testing of payloads, subsystems, and components,” https://extapps.ksc.nasa.gov/Reliability/Documents/Preferred_Practices/1419.pdf.
- [37] “Sandvik 12r11 strip steel,” <https://www.materials.sandvik/en/materials-center/material-datasheets/strip-steel/sandvik-12r11/>.
- [38] D. Farhadi Machekposhti, N. Tolou, and J. Herder, “A review on compliant joints and rigid-body constant velocity universal joints toward the design of compliant homokinetic couplings,” *Journal of Mechanical Design*, vol. 137, no. 3, p. 032301, 2015.
- [39] “Vibroacoustic qualification testing of payloads, subsystems, and components,” https://extapps.ksc.nasa.gov/Reliability/Documents/Preferred_Practices/1419.pdf.
- [40] M. Bass, *Handbook of Optics*. McGraw-Hill, 1994, vol. 2.
- [41] J. B. Hopkins and M. L. Culpepper, “Synthesis of multi-degree of freedom, parallel flexure system concepts via freedom and constraint topology (fact)–part i: Principles,” *Precision Engineering*, vol. 34, no. 2, pp. 259–270, 2010.
- [42] “Lightpipes optical toolbox,” <https://pypi.org/project/LightPipes/>.